Influence of exhaust gas recirculation on performance of a turbocharged diesel engine running on biofuel blends

by
Louis André Albertyn

Thesis presented in partial fulfilment of the requirements for the degree of Master of Engineering (Mechatronic) in the Faculty of Engineering at Stellenbosch University

UNIVERSITEIT
iYUNIVESITHI
STELLENBOSCH
UNIVERSITY

Supervisor: Mr Richard Walter Haines

March 2018

DECLARATION

By submitting this thesis electronically, I declare that the entirety of the work contained therein is my own, original work, that I am the sole author thereof (save to the extent explicitly otherwise stated), that reproduction and publication thereof by Stellenbosch University will not infringe any third-party rights and that I have not previously in its entirety or in part submitted it for obtaining any qualification.

March 2018

UNIVERSITEIT·STELLENBOSCH·UNIVERSITY
jou kennisvennoot • your knowledge partner

Plagiaat verklaring / Plagiarism Declaration

Plagiaat is die oorneem en gebruik van idees, materiaal en ander intellektuele eiendom van ander persone asof dit jou eie werk is.
Plagiarism is the use of ideas, material and other intellectual property of another's work and to present is as my own.

Ek erken dat die pleeg van plagiaat 'n strafbare oortreding is aangesien dit 'n vorm van diefstal is.
I agree that plagiarism is a punishable offence because it constitutes theft.

Ek verstaan ook dat direkte vertalings plagiaat is.
I also understand that direct translations are plagiarism.

Dienooreenkomstig is alle aanhalings en bydraes vanuit enige bron (ingesluit die internet) volledig verwys (erken). Ek erken dat die woordelikse aanhaal van teks sonder aanhalingstekens (selfs al word die bron volledig erken) plagiaat is.
Accordingly, all quotations and contributions from any source whatsoever (including the internet) have been cited fully. I understand that the reproduction of text without quotation marks (even when the source is cited) is plagiarism.

Ek verklaar dat die werk in hierdie skryf stuk vervat, behalwe waar anders aangedui, my eie oorspronklike werk is en dat ek dit nie vantevore in die geheel of gedeeltelik ingehandig het vir bepunting in hierdie module/werkstuk of 'n ander module/werkstuk nie.
I declare that the work contained in this assignment, except where otherwise stated, is my original work and that I have not previously (in its entirety or in part) submitted it for grading in this module/assignment or another module/assignment.

15649768 Studentenommer/ *Student number*	 Handtekening/ *Signature*
L.A. Albertyn Voorletters en van/ *Initials and surname*	2017-11-30 Datum/ *Date*

ABSTRACT

Exhaust gas recirculation technology has been implemented with success in the automotive industry in reducing nitrogen oxides in diesel exhaust gas. Given that South Africa's Clean Fuels programme currently adheres to Euro II fuel and emissions standards, research into the influence of exhaust gas recirculation on a more modern TDI engine running on locally sourced biofuel blends is done for this project.

In this research project the existing engine test bench is upgraded by equipping the exhaust gas recirculation system as well as the compressor of the variable geometry turbocharger with various sensors and instrumentation. All the data acquired from the sensors is logged by a graphical user interface program developed in LabVIEW. National Instruments data acquisition devices USB 6351 and USB 4350 are interfaced with LabVIEW to obtain the recorded data. Further improvements include the addition of a water-to-air intercooler developed in-house to control the charge air temperature. An eddy current dynamometer replaces the previous hydraulic dynamometer to improve steady state speed and torque control of the engine.

Experiments were performed on two biofuel blends, B20 and E10, using crude derived pump fuel as the base fuel. Both biofuel blends were splash blended and mixed by volume. The B20 blend consists of twenty percent biodiesel, obtained from waste cooking oil, and eighty percent base fuel. The E10 blend consists of ten percent ethanol mixed with the ninety percent base fuel. All fuels are refined locally. The control of the exhaust gas recirculation is maintained as per the original equipment manufacturer. The focus of this study is therefore to determine how exhaust gas recirculation affects a diesel engine optimised to run on ultra-low sulphur diesel and how it responds to running on different biofuel blends in terms of fuel consumption, temperatures and emissions of specifically nitrogen oxides.

Results suggest that there is little to no variation in brake specific fuel consumption at the partial loads tested. The emission of nitrogen oxides does not deviate significantly between the fuels, however a marked reduction in soot is noticed for the E10 blend. Carbon monoxide concentrations are also higher for the E10 blend at high speed, low load operating points. As expected, nitrogen oxides are increased with the reduction in exhaust gas recirculation rate.

OPSOMMING

Uitlaatgas hersirkulasie word suksesvol deur die motor industrie gebruik om stikstof oksiede in diesel uitlaatgasse te verminder. Suid-Afrika se Skoon Brandstof program voldoen tans aan Euro II brandstof en uitlaatgas standaarde. Hierdie projek fokus dus op navorsing van die invloed van uitlaatgas hersirkulasie op 'n meer moderne TDI enjin, wat loop op plaaslik vervaardigde biobrandstof mengsels.

Die navorsings projek behels die opgradering van die enjin toetsbank deur die uitlaatgas hersirkulasie sisteem sowel as die kompressor van die turboaanjaer, volledig uit te rus met sensors en instrumentasie. Alle data verkry vanaf die sensors word opgeneem deur 'n grafiese verbruikers koppelvlak program wat ontwikkel is in LabVIEW. Die sensor informasie word deur ´'n National Instruments USB 6351 en USB 4350 toestel na die rekenaar herlei deur LabVIEW. Verbeterings aan die toetsbank sluit in die vervanging van die oorpronklike tussen-verkoeler met 'n water-na-lug tussen-verkoeler om die saamgedrukte lug se temperatuur te beheer. 'n Nuwe werwelstroom dinamometer, wat die vorige hidrouliese dinamometer vervang, verseker dat die bestendigde toestand van spoed en wringkrag beheer op die toetsbank ook verbeter is.

Eksperimente word uitgevoer op twee biobrandstof mengsels, B20 en E10, met ru-olie afkomstige pomp diesel as 'n basis brandstof. Beide mengsels was afgetap en per volume gemeng. Die B20 mengsel beslaan twintig persent biodiesel, afkomstig vanaf ou kookolie, en tagtig persent van die basis brandstof. Die E10 mengsel beslaan tien persent etanol en negentig persent van die basis brandstof. Alle brandstowwe word plaaslik vervaardig. Die beheer van die uitlaatgas hersirkulasie sisteem word bepaal deur die oorspronklike enjin beheereenheid. Die navorsing fokus op die veranderinge wat te weeg gebring word deur die uitlaatgas hersirkulasie sisteem op die enjin karakteristieke insluitend brandstofverbruik, temperature en uitlaatgasse soos stikstof oksiede. Die aanpassing van die enjin beheereenheid met die gebruik van verskillende brandstowwe is ook van belang.

Die resultate dui daarop aan dat die spesifieke brandstof verbruik, by laer wringkragte, nie baie varieer tussen die verskillende brandstowwe nie. Die uitlaat van stikstof oksiede varieer nie merkwaardig tussen die verskillende brandstowwe nie, maar die uitlaat van swart roet verminder vir die E10 mengsel. Koolstofmonoksied konsentrasies is hoër vir die E10 mengsel, teen hoë enjin spoed met lae wringkrag. Stikstof oksiede vermeerder hoe minder uitlaat gasse teruggevoer word na die inlaat van die enjin, soos verwag deur die gebruik van uitlaatgas hersirkulasie.

ACKNOWLEDGEMENTS

The author would like to thank the following:

- Mr Richard Haines for his support and advice during the project.
- Mr Gerhard Lourens, from the Sasol fuels application centre, for consulting on the upgrade of the engine test bench.
- Mr Reynaldo Rodriguez for the technical assistance provided during the project.
- Also, all the workshop personnel, without whom this project could not have been done.

TABLE OF CONTENTS

LIST OF FIGURES

LIST OF TABLES

NOMENCLATURE

Symbols

A	Area
c	Velocity
C_d	Discharge coefficient
c_p	Specific heat
d	Diameter
g	Gravitational constant
K	Dynamic temperature correction factor
m	Mass
Ma	Mach number
p	Pressure
q	Flow rate
R	Gas constant
T	Temperature
t	Time
V	Volumetric
z	Elevation
β	Diameter ratio
ε	Expansibility factor
η	Efficiency
θ	Crank angle
κ	Isentropic exponent
ρ	Density

Superscripts

´	Corrected

Subscripts

B	Brake
d	Dynamic
m	Mass
s	Static
t	Total
V	Volume
1	Inlet
2	Outlet

Abbreviations

ASTM	American society for testing and materials
B20	Twenty percent volume biodiesel-diesel blend
BDC	Bottom-dead-centre

BSFC	Brake specific fuel consumption
CAD	Computer aided design
CFPP	Cold filter plugging point
CFR	Cooperative fuel research
CNC	Computer numeric control
CO	Carbon monoxide
CO_2	Carbon dioxide
DOC	Diesel oxidation catalyst
DPF	Diesel particulate filter
E10	Ten percent volume ethanol-diesel blend
ECU	Engine control unit
EGR	Exhaust gas recirculation
EM	Emissions
EN	European standards
EPA	Environmental protection agency
ETA	Engine test automation
EU	European union
FAME	Fatty acid methyl esters
FBS	Fixed bearing side
FS	Full scale
FSN	Filter smoke number
GUI	Graphic user interface
HC	Hydrocarbons
HHV	Higher heating value
ISO	International Organization for Standardization
LBS	Loose bearing side
LHV	Lower heating value
LPG	Liquefied petroleum gas
LR	Long route
MAF	Mass air flow
MAP	Manifold absolute pressure
N_2	Nitrogen
NASA	National aeronautics and space administration
NO	Nitrogen monoxide
NO_2	Nitrogen dioxide
NO_X	Nitrogen oxides
O	Monoxide
O_2	Oxygen
OEM	Original equipment manufacturer
PC	Programmable computer
PLC	Programmable logic controller
PM	Particulate matter
RSE	Referenced single-ended
SAE	Society of Automotive Engineers
SANS	South African national standards
SAPIA	South African petroleum industry association

SR	Short route
SVO	Straight vegetable oil
TDC	Top-dead-centre
TDI	Turbocharged direct injection
ULSD	Ultra-low sulphur diesel
VAG	Volkswagen of America group
VCDS	Vag-com diagnostic software
VGT	Variable geometry turbocharger

1. INTRODUCTION

Demand for on-road vehicles are growing as the world's population increases each year. This puts a strain on the dwindling fossil fuel resources. Recent trends in the automobile industry indicate a shift towards electric vehicles. These alternatives, however efficient they are, are unfortunately still limited by their fuel source. For this reason, the internal combustion engine will remain a large part in the production of vehicles until a suitable alternative is presented.

The focus has shifted however, from producing large, naturally aspirated, internal combustion engines to smaller turbocharged engines which run more efficiently on either crude derived fuels or biofuel blends. With the drive from legislators to reduce the automobile's harmful emissions footprint, technologies such as exhaust gas recirculation has been implemented with success in reducing nitrogen oxides emissions, specifically. The potential in combining these technologies have great benefit towards reducing the emissions footprint of the internal combustion engine.

Biofuel blends are of great interest as they offer reduced green-house gas emissions, although there are some disadvantages to using biofuel blends.

This thesis aims to investigate the influence of biofuels on a small four-cylinder turbodiesel engine fitted with an uncooled, custom designed short route exhaust gas recirculation (EGR) system. The investigation aims to establish how the engine control unit's control strategy responds to biofuel blends on an engine optimised to run on crude derived pump diesel, with respect to the turbocharger and exhaust gas recirculation system.

1.1. Background

Fossil fuel deposits are becoming ever scarcer. These fuel deposits are becoming ever harder to extract. Alternatives to fossil fuels must therefore be developed. There exists such an alternative in the form of biofuels. These fuels can be derived from a variety vegetable or animal fats. The disadvantage to these fuels however, are that they are significantly more expensive versus the current major fuel source, crude oil, even considering the increase in fuel prices the world is currently experiencing. Environmentalist and scientist warn that the current concentration of the Earth's crude oil reserves is dwindling which make the world's reliance on the use of fossil-based fuels unsustainable.

A change in global mind set is therefore needed. To bring about this change concrete scientific data is required to motivate the claims of many engineers and scientists about the potential for biofuels to reduce the global community's dependency on fossil fuel. The chief method for acquiring such data is by use of a laboratory engine test bench. A variety of tests such as emissions testing, engine performance and fuel efficiency tests can be performed with these setups. Such installations are expensive not only because of the equipment costs but also due the

costs associated with training experienced personnel to run engine testing laboratories, especially when one considers South Africa.

In 2006, the Department of Mechanical and Mechatronic Engineering of Stellenbosch began commissioning the development of an engine test cell facility with the purpose of researching biofuels. The first test bench commissioned comprised an old technology 2.0 litre turbodiesel engine with a Schenck D360 hydro dynamometer (Palmer, 2008). This was a very simple and rudimentary system without an engine control unit (ECU), therefore the existing engine was replaced by a modern 1.9 litre TDI engine fitted with exhaust gas recirculation and an engine control unit. In-cylinder pressure measurement capabilities where added to the test bench to facilitate the capability to perform heat release analyses on the engine (Kotze, 2010).

Most recently the test bench has been upgraded to include emissions measurement capabilities as well as improvements that were made to the overall safety of the test bench (Blom, 2015). Blom (2015) also recommended some improvements to be made to the test setup at the time, therefore as part of this thesis these improvements are addressed.

1.2. Motivation

The primary motivation for this project is to inject new research capabilities into the South African market and specifically allow the Department of Mechanical and Mechatronic Engineering access to a modern diesel engine test bench. The effects different biofuel blends have on the performance characteristics and emissions profile of the engine, fitted with exhaust gas recirculation, was investigated.

In addition to this, the test bench can also then be utilised to present practical sessions for undergraduate engineering modules, to allow students some exposure to automotive systems and their operation. This will be invaluable to recruit more students' interest into the field of internal combustion engines and help develop the laboratory capabilities even further.

1.3. Objectives

The primary objectives of the project are as follows:

- Further develop the existing diesel engine test bench, to include measurement capabilities on the peripheral systems of the engine including the exhaust gas recirculation system and variable vane turbocharger.

- Acquire diesel engine performance, turbocharger, exhaust gas recirculation and emissions data for biofuel blends.

1.4. Document outline

This thesis consists of a chapter containing a literature review into research already conducted in the field of engine emissions and performance of biofuel blends. The literature review also covers the individual engine components that are to be utilised on the engine test bench.

Chapter three focuses on the instrumentation design and layout of both the exhaust gas recirculation and variable vane turbocharger systems as well as the development of the LabVIEW graphical user interface (GUI) used to measure different parameters on the test bench. Signal conditioning and processing of data is briefly reviewed to inform the reader on the methods utilised to obtain the necessary information to display it in the LabVIEW graphical interface.

The experimental chapter consists of defining the setup of each batch of experiments to detail the process to replicate the experiments. The discussion chapter focuses on analysing and discussing the data obtained from the experiments and to compare the results to similar experiments found in literature.

The conclusion on the results obtained is given along with suggestions for further research and development on the 1.9 litre TDI engine test bench.

2. LITERATURE REVIEW

The following chapter comprises of a literature study on diesel and biofuel blends. Both local and international legislation are considered. The principle of operation of the diesel engine is explored, along with the various mechanisms by which nitrogen oxides form.

The basic exhaust gas recirculation method as well as options to improve its capability of reducing regulated exhaust emissions, is discussed. The principle of operation for a turbocharger is reviewed. The variable geometry turbocharger technology employed by the current test engine's original equipment manufacturer (OEM) is detailed.

2.1. Fuel properties

The *cetane number* is a measure of the ignition quality of the diesel fuel. Ignition quality is defined as the time interval between the start of injection and the start of combustion, i.e. the *ignition delay*. Various advantages are attributed to a higher cetane number, such as better cold starting performance, reduced white smoke, reduced acoustics due to combustion and an overall reduction in nitrogen oxides (NOx) and particulate matter (PM) emissions (Majewski & Jääskeläinen, 2013) (Rashedul, et al., 2014). The cetane number of a diesel fuel is determined experimentally with a cooperative fuel research (CFR) engine, which is a single-cylinder engine with a mechanism to adjust the compression ratio (Richards, 2014).

Cetane numbers are related to that of octane numbers in that they both test the auto-ignition tendency of the fuel. However, whereas cetane numbers are a measure of the readiness of diesel to ignite in a diesel engine, octane numbers represent fuels that resist auto-ignition and knock in a petrol engine. This means that high cetane numbers correspond to low octane numbers and vice versa (Chevron, 2007).

The *density* of a fuel has a large impact on the fuel economy and the maximum power the engine can deliver, since an increased density usually leads to an increase in the energy content of the fuel (DieselNet, 2002) (Richards, 2014). According to the Euro VI fuel specifications, the density of reference diesel fuel being used by on-road diesel driven vehicles should be in the range of 833 to 837 kg/m^3 at a temperature of 15 $°C$ compared to that of petrol which has a much lower density at roughly the same temperature of 20 $°C$ (Martinez, 2017), as shown in Table 1. Reducing the density of the fuel has an impact on emissions. A reduction in density leads to a decrease in particulate matter as well as nitrogen oxides. This has an inverse effect on hydrocarbons (HC) and carbon-monoxide (CO), which increases. The performance of fuel injectors is also adversely affected (DieselNet, 2002).

Heating value is defined as the amount of heat/energy released during combustion. Two measures of heating value exist, namely the higher heating value (HHV) and the lower heating value (LHV). The higher heating value is determined by

measuring the amount of heat released when the fuel is combusted, and all the products have returned to a temperature of 25 °C, i.e. the water that took part in the combustion process has condensed back to a liquid. The higher heating value therefore includes the heat of condensation of the water which is why it is also known as the gross calorific value (Heywood, 1988) (Challen & Baranescu, 1999). The lower heating value is determined by subtracting the heat of vaporization from the higher heating value and is therefore also known as the net caloric value. As expected the lower heating value is used when water is in its vapour form and is therefore usually the metric used when comparing fuels (Majewski & Jääskeläinen, 2013) (Richards, 2014).

Volatility, also known as the distillation temperature of a fuel, refers to the point at which the fuel starts to evaporate. This characteristic is especially important, since a low volatility directly correlates to reduced emissions of hydrocarbons and carbon monoxide (Richards, 2014). A reduced volatility of the diesel has a negative effect on the cold starting capability of an engine due to the increased amount of energy needed to bring the fuel up to evaporation temperature (Heywood, 1988) (Stone, 1992).

Viscosity of a fluid relates to the fluid's resistance to flow, with a higher viscosity indicating a greater resistance to flow. The viscosity of diesel is critical in ensuring optimal operating conditions for the engine. A low viscosity can have adverse effects such as leakage and reduced lubricity between the cylinder and piston surfaces causing more friction which leads to increased wear (Essay UK, 2016). Conversely, too high a viscosity and the fuel will resist flow in the fuel lines leading to damage of the fuel pump and injectors. (Majewski & Jääskeläinen, 2013).

Low temperature operability refers to any fuel's capability to be used in extremely cold conditions. Per Majewski & Jääskeläinen (2013), diesel has a high ratio of alkanes to cycloalkanes and aromatics. This gives diesel the tendency to form wax as the fuel cools down, obstructing the fuel lines and blocking fuel filters as the wax crystal propagation intensifies. The *Pour point* of a liquid fuel is defined as the lowest temperature at which the fuel can flow properly and as such it at a temperature only slightly above that of the cloud point of a fuel. The *Cloud point* of a fuel is the temperature at which wax crystals start to form in the fuel (Richards, 2014). Similarly, the *Cold Filter Plugging Point* (CFPP) is the lowest temperature at which diesel can pass through a standardized filter as set out by the ASTM 6371 standard (ASTM D6371, 2017). Refineries counteract this tendency to form wax by introducing certain additives such as kerosene and petrol. The role of ethanol as an oxygenating additive in diesel is covered in section 2.1.3.

Flash point is the temperature at which a fluid evaporates a sufficiently high enough concentration to form a combustible gas, i.e. the ease of a fuel to burn. Lower flashpoints indicate a greater flammability (DieselNet, 2002). The flashpoint of diesel is very high and as a result it is safer to store diesel as it does not combust

easily, in contrast to petrol's high flammability (Richards, 2014) (Majewski & Jääskeläinen, 2013).

The *lubricity* of a fuel directly impacts the engine components' wear and fatigue. Viscosity and cleanliness, which refers to the quantity of contaminants in the fuel, are characteristics which directly influence the lubricity of a fuel (Richards, 2014). The ability of the fuel to form a stable hydrodynamic film on the surfaces it encounters describes the lubrication quality of the fuel. In general, a higher concentration of polyaromatics and polar impurities in a fuel increases its lubrication quality. It should be of note that modern diesel contains a range of additives to improve the lubrication qualities of the fuel, since extraction of sulphur from the fuel also leads to the removal of compounds that are beneficial to lubrication (Majewski & Jääskeläinen, 2013).

Sulphur has a host of disadvantages that affects not only the engine performance, but also has implications to the health of the environment and humans. The sulphur content in diesel forms sulphur dioxide (SO_2), a primary precursor to acid rain. It has been reported that high sulphur content, 2000 *ppm*, can lead to an increase in particulate matter (Merkisz, et al., 2002). Legislation pioneered by the environmental protection agency (EPA) of the United-States of America and the European Union (EU) led to the reduction of sulphur in diesel in 1993 and 1996 respectively (Chevron, 2007). Many developing countries such as South Africa adopted the EU standards, however due to their vehicle parc, the continued development of those standards lag international trends set by developed countries (SAPIA, 2008).

2.1.1. Diesel

Traditional diesel fuel is derived from crude oil and is refined into several products. These products comprise three categories, namely light, middle and heavy distillates. Diesel fuel falls into the middle distillates category along with kerosene and other residential heating fuels such as LPG (Chevron, 2007).

As the above categorization suggests, the refining process begins with a raw batch of crude oil. With each successive process, the raw material is broken down into different substances depending on the refinement process being used, but the longer the refinement chain the lighter the eventual product becomes. Therefore, diesel has a higher energy content per litre than that of petrol, a light distillate, as Table 1 shows (Alternative Fuels Data Center, 2014).

Table 1: Diesel versus petrol characteristics (Alternative Fuels Data Center, 2014)

	Energy Content [MJ/litre]	Density [kg/m^3]	Viscosity [mm^2/s]
Diesel	35.8 to 38.6	833 to 837	3.0
Petrol	31.3 to 34.7	720 to 760	0.5

Diesel is comprised mainly of different compositions of hydrocarbons. These hydrocarbons are classified into either the alkane, cycloalkane or aromatic classes. Depending on the quality of the raw crude oil, smaller concentrations of sulphur, oxygen and nitrogen may also be present. Different compositions of the three classes of hydrocarbons, mentioned above, produce varying characteristics and properties in the diesel. (Chevron, 2007). The most widely used crude diesel generally contains twelve or more carbon atoms and has a flash point of 55 *°C*. Cetane numbers for diesel range from 40 to 50 (Ferguson & Kirkpatrick, 2001). The South African standard for diesel is represented in SANS342 (2016) with required cetane numbers of 45 and sulphur content of 50 *ppm* for the current clean fuels program. Diesel generally has good lubricity, however when additives are mixed in to prevent wax formation in cold conditions, the lubricity of diesel is reduced (Richards, 2014).

2.1.2. Biodiesel-diesel blends

Pure biodiesel (B100) is a refined fuel obtained from transesterification and esterification of short chain organic oils and fats from both fauna and flora (Rashedul, et al., 2014). The term biodiesel encompasses a broad spectrum of fuels with differing molecular structures. The focus of this review however will be solely on *alkyl esters*. Although Straight Vegetable Oil (SVO) can be used as a diesel fuel, the potential ramifications it has for smooth engine operation is great. The properties of straight vegetable oil such as its high viscosity can lead to poor atomization of fuel, incomplete combustion, choking of the fuel injectors, ring carbonization and accumulation of the fuel in the lubricating oil (Knothe, et al., 2005).

Transesterification is a process by which the abovementioned sources are converted into biodiesel by allowing the fatty acid/triglyceride oils to react with an alcohol to form fatty acid mono alkyl esters and glycerol. A strong catalyst is needed for the transesterification to take place (Knothe, et al., 2005). By esterification of the straight vegetable oil, the fuel properties are improved, most importantly for engine operation, a lower viscosity and lower pour point (Richards, 2014).

The most prevalent feedstock of biodiesel include soybean, rapeseed, palm, sunflower, coconut and camelina. These are all edible sources which impact on the human food supply, therefore recent research has shifted its focus more towards inedible sources such as jatropha and kanuga (Majewski & Jääskeläinen, 2009). Jatropha specifically is a promising source for biodiesel production as it is very adaptable to harsh environments with degraded soil and its resistance to disease and pests is high (Openshaw, 2000) (Maina, 2014). South African biodiesel is obtained primarily from waste cooking oil or pure plant oil (IBSA dialogue forum, 2010).

Biodiesel has many advantages over crude derived diesel. These include its cleaner tailpipe emissions profile in terms of hydrocarbon, carbon monoxide and particulate matter with virtually no sulphur oxides (SO_x). The trade-off in emissions come in

the form of increased nitrogen oxide emissions, although there exists no consensus on this in literature since many reports on biodiesel emissions are contradictory (Majewski & Jääskeläinen, 2009).

The reason for this may be due to the biodegradability of biodiesel and the fact that the quality of biodiesel can vary greatly from country to country due to the different standards set for biodiesel as well as the differing sources of biodiesel. Many manufacturers now support the addition of biodiesel to crude derived diesel up to ten percent. Table 2 illustrates the differences between international biodiesel standards (Jääskeläinen, 2009).

Table 2: Difference in international standards for pure biodiesel (Martinez, 2017)

Properties	**ASTM D6751**	**EN 14214**
Density	Unspecified	860 – 900 kg/m^3
Cetane Number	47	51
Viscosity	1.9 -6.0 mm^2/s	3.5 - 5.5 mm^2/s
Sulphur Content	15 ppm	10 ppm
Mono glycerides	0.4% wt.	0.7% wt.
Diglycerides	-	0.2 % wt.
Triglycerides	-	0.2 % wt.
Total glycerine	0.24 % wt.	0.25 % wt.

It should be noted that the ASTM D6751 does not specify which alcohol should be used to refine the biodiesel, whereas the EN 14214, which the South African standard SANS 1935:2011 is based on, restricts the use of alcohol as catalyst to methanol, resulting in the product being fatty acid methyl esters (FAME) (SANS1935, 2011) (Jääskeläinen, 2009). When comparing biodiesel to crude derived diesel, the low temperature operation capabilities of biodiesel is severely impaired compared to that of crude derived diesel. This is due to the presence of saturated long chain fatty acids in most biodiesel blends and therefore biodiesel must often be augmented with additives to enhance its low temperature operation capabilities (Jääskeläinen, 2009).

In contrast to its poor low temperature operation, biodiesel has excellent lubrication characteristics and it is often added to crude derived diesel to enhance its lubricity. International standards ASTM D975, D7467 govern blends B5 and B6 to B20 respectively, whereas EN 590 covers blends up to B7. The standards all evolve over time to include higher blends of biodiesel in petroleum diesel, as is evident by the new EN 16734 allowing biofuel blends of up to ten percent (Jääskeläinen, 2009). Twenty percent biodiesel blends, B20, is a popular biodiesel-diesel blend. It has been established that with an increasing the percentage of biodiesel in a blend leads to an increase in brake specific fuel consumption, carbon monoxide and nitrogen oxides whilst reducing smoke emissions (Kivevele, et al., 2011) (Wu, et al., 2012).

2.1.3. Ethanol-diesel blends

Diesel fuel can be augmented by adding oxygenating additives. Various techniques such as alcohol fumigation, dual injection, emulsion and blending, exist by which additives can be introduced to the combustion process alongside diesel (Jääskeläinen, 2016). The emissions profile of the exhaust produced when diesel is burned are among the primary reasons additives are added to diesel. The following discusses the use of ethanol addition to crude oil diesel.

Ethanol (C_2H_6O) is one of the most commonly used oxygenates when blending biofuels, with an oxygen mass fraction of thirty-five percent. It is often blended up to fifteen percent with crude derived diesel. The renewable nature of ethanol makes it an attractive option for biofuel blending. Ethanol feedstocks in South Africa are produced from primarily two biomass sources containing sugar and starch (IBSA dialogue forum, 2010). The blend stability of ethanol-diesel blends is difficult to maintain without any additives. This is because the stability is readily influenced by environmental factors such as temperature and humidity. Water in any form can cause the blend to separate or become unclear (Lei, et al., 2011). (Jääskeläinen, 2016).

Ethanol when added to either diesel or biodiesel, allows the fuel to ignite more completely, leading to reduced particulate matter and soot (Rashedul, et al., 2014). According to Jääskeläinen (2016), the effect oxygenated additives has on the emissions profile of nitrogen oxides, carbon monoxide and hydrocarbons are still disputed by many researchers in literature, however Lei, et al. (2011) reported increased carbon monoxide levels for low engine loads due to the reduction of gas temperature with the trend switching at higher loads because of increased oxidation of carbon monoxide resulting from higher gas temperatures at the higher operating points for E10 ethanol-diesel blends.

Adding between ten and twenty percent ethanol to crude derived diesel will extend the ignition delays during combustion by lowering the cetane number of the fuel. It also lowers the flashpoint of the blend to 17 $°C$ making it dangerous to store the fuel for extended periods of time (Jääskeläinen, 2016). The tendency of ethanol-diesel blends to form vapour in the fuel lines can also lead to cavitation, damaging fuel injectors and pumps (Waterland, et al., 2003).

2.2. Internal combustion engine technology

The internal combustion engine has evolved significantly since its invention in 1876 by German engineer, Nikolaus Otto the inventor of the spark ignition engine. The advent of the spark-ignition engine was closely followed by the invention of the compression-ignition engine in 1892, now more commonly referred to as the diesel engine named after its inventor Rudolf Diesel. These early engines however were very primitive and lacked many of the peripheral components that are considered commonplace on modern engines. The following section details the principle of

operation behind the modern compression-ignition engine and the supporting systems and devices that contribute to its overall performance and efficiency.

2.2.1. Compression ignition engines

The first internal combustion engine operated on a four-stroke cycle to deliver mechanical power converted from the chemical energy contained in the fuel. With regards to the topic of this thesis only the four-stroke internal combustion diesel engine is reviewed in this section.

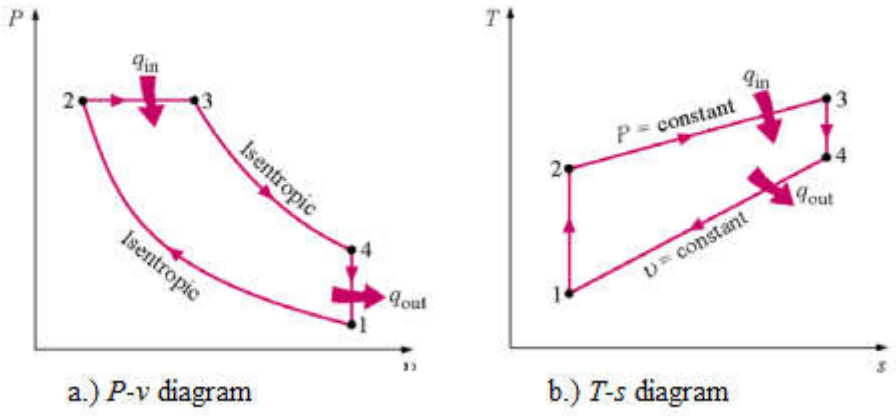

Figure 1: The ideal Diesel cycle (Cengel & Boles, 2007)

The four strokes, referred to above, are the *Intake*, *Compression*, *Power* and *Exhaust* strokes each lasting approximately 180° rotation of the crank shaft. Figure 1 shows the changes in pressure and temperature between each stroke, with (1) representing the start of the intake stroke and (4) representing the start of the exhaust stroke (Cengel & Boles, 2007) (van Basshuysen & Schäfer, 2004).

The *Intake stroke* initiates with the piston near the top dead centre (TDC, 0° crank angle) of the cylinder where the exhaust and air intake valves are positioned. Once the exhaust valve closes at the end of the exhaust stage, the air intake valve opens. The air is then induced through the inlet valve. Depending on whether the engine is turbocharged or naturally aspirated, the air flow rate entering the cylinder varies. Boosted air induced into the cylinder chamber, forces the piston down, facilitating the downwards stroke of the piston and connecting rod to bottom-dead-centre (BDC, 180° crank angle), rotating the crankshaft as seen in Figure 2 (Brian, 2000) (van Basshuysen & Schäfer, 2004) (Mollenhauser & Tschoeke, 2010).

Various factors during this stage influence the overall performance, efficiency and emissions profile of the engine. Diesel engines by design operate on excess air, with air-to-fuel (A/F) ratios of the inducted charge air ranging from 25:1, for naturally

aspirated engines, to 160:1, for turbocharged engines (Jääskeläinen & Khair, 2016). The size of the intake valve determines the mass of air that can be induced into the cylinder which directly influences the air-to-fuel ratio. The significance of the air-to-fuel ratio during combustion is discussed in the *power stroke* (Jääskeläinen & Khair, 2014) (Heywood, 1988) (Mollenhauser & Tschoeke, 2010).

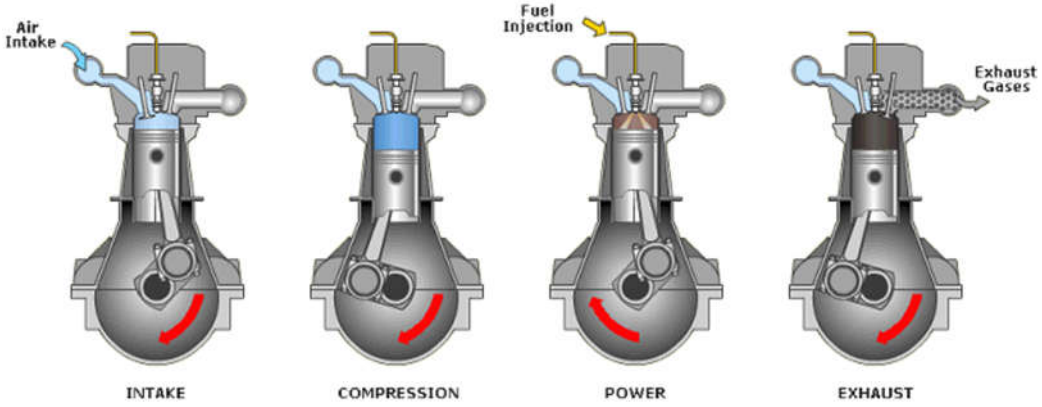

Figure 2: Four stroke Diesel cycle (Brian, 2000)

The next stroke is the *Compression* stroke. During the compression stroke all valves are closed/sealed to prevent any air escaping from the cylinder. The piston can therefore compress the contained air which characterises the compression stroke by noting a significant increase in both pressure and temperature. The energy required to drive the compression stroke is driven by the momentum of the flywheel, in manual transmission vehicles, or the flex plate, in vehicles with automatic transmissions (Stone, 1992).

Ideally this stroke is performed adiabatically since the increase in temperature is due to the air being compressed. The compression ratio achieved during this stage affects factors such as the fuel vaporization, mixing rate and combustion quality during the power stroke. The volume of air between the top piston ring and the piston crown is also compressed but never participates in the combustion during the power stroke. This volume remains constant during the compression stroke and effectively reduces the efficiency of the engine and should be kept to a minimum. The upwards stroke completes the first full revolution of the crankshaft. Just before the piston reaches top dead centre, fuel is injected facilitating the auto-ignition/compression ignition event (Heywood, 1988).

Widespread discussion still rages to this day as to where the compression stroke ends and where the power stroke begins, owing to the extreme complexities of the compression-ignition process. To simplify the explanation, the following stages of *ignition delay*, *premixed combustion* and *rate-controlled combustion* is considered a part of the *Power* stroke, which starts just before a full 360° rotation of the crankshaft (Jääskeläinen & Khair, 2016).

The *ignition delay* period is the first stage of the power stroke between the start of injection and the first instance of detectable combustion. Combustion occurs when sudden changes in pressure and temperature are observed right after the fuel injection (Heywood, 1988) (Mollenhauser & Tschoeke, 2010). A heat release analysis is a good tool in identifying the start of combustion, when the net rate of heat release reaches zero. This is considered the start of auto-ignition and is often characterised by a sudden change in pressure and temperature (Jääskeläinen & Khair, 2016).

The importance of the duration of the ignition delay is apparent when considering the emissions profile of the engine. Mixture preparation takes place during the ignition delay and is responsible for pre-ignitions and localized ignitions, which result from the rich mixture of the inducted charge air and the injected atomized fuel spray (Heywood, 1988). These small events are driven primarily by the physical kinetics of swirl inside the cylinder and does not contribute significantly to the start of combustion but rather assists in breaking hydrocarbon chains which generate free radicals (Jääskeläinen & Khair, 2016).

The ideal chemical reaction referred to as combustion, occurs in the absence of any contaminants which is a reaction purely between oxygen and hydrocarbons. The energy produced during combustion is a result of the net release of energy as molecular bonds break and form. This excess energy is released in the form of heat along with water and carbon dioxide in the following exothermic reaction (Petroleum.co.uk, 2015):

$$C_{12}H_{23} + 71O_2 \rightarrow 48H_2O + 46CO_2 + Energy \quad (1)$$

Premixed combustion is the first detectable instance of combustion inside the cylinder. It is marked by an extreme rise in both pressure and temperature due to the auto-ignition that occurs. During this period of the power stroke the combustion is driven purely by chemical kinetics. The sudden increase of both pressure and temperature results in the characteristic noise of a diesel engine, as the localised air fuel mixture pockets are burnt off (Mollenhauser & Tschoeke, 2010) (Jääskeläinen & Khair, 2016). Particulate matter, or soot, results from the combustion of these rich pockets of fuel. The amount of fuel burnt during the premixed combustion period is dependent upon the engine speed, load, injection quantity and injection timing (Jääskeläinen & Khair, 2016). It is the premixed combustion that initiates the downward stroke of the piston.

Rate-controlled combustion is responsible for most of the conversion of chemical energy, contained in the fuel, to mechanical energy. It is characterised by a gradual rate of heat release over a longer period than that of the premixed combustion. Figure 3 illustrates the different combustion phenomena that occurs during rate-controlled combustion (Jääskeläinen & Khair, 2016). It is during this period that the emissions profile of the exhaust gas is determined.

Due to the premixed combustion period, very few rich fuel pockets still exist inside the cylinder. This means that the remaining fuel inside the cylinder forms a lean fuel mixture, which produces most of the unburnt hydrocarbons that are exhausted into the atmosphere when burnt.

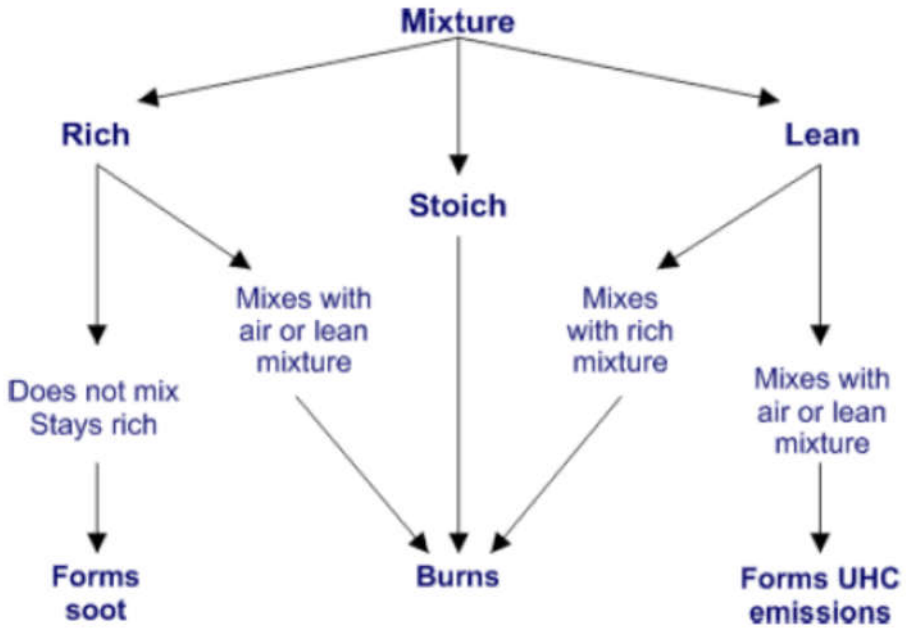

Figure 3: Mixture to combustion routes (Jääskeläinen & Khair, 2016)

The *exhaust stroke* takes place at the last 180° of the four-stroke cycle. The piston is driven upwards as the exhaust valves open to drive out the exhaust gas into the exhaust manifold. In a naturally aspirated engine the entirety of the exhaust gas is expelled out of the exhaust pipe, wasting useful mechanical energy. A forced induction engine however uses this mechanical energy to raise the efficiency of the engine before the exhaust gas is expelled by passing it through a turbocharger, as explained in section 2.2.3 (van Basshuysen & Schäfer, 2004) (Hiereth & Prenninger, 2007).

2.2.2. Exhaust gas recirculation

Exhaust Gas Recirculation (EGR) is an emissions regulation pre-treatment technique designed to utilise the exhaust gas, generated by the combustion process, to specifically reduce the emission of nitrogen oxides (Agarwal, et al., 2011). (Reif, 2014)

The development of exhaust gas recirculation is primarily driven by increasingly stringent emissions requirements, set forth by the international legislative bodies. The South African standard for fuels, Clean Fuels 1 (CF1) is currently based on the Euro II vehicle standard. The phase-in of the Clean Fuels 2, based on Euro V standards is currently delayed (SAPIA, 2017). Light-duty vehicles being imported

to South Africa are however being fitted with emissions reduction technologies driven by standards set forth by the EU and EPA. The exhaust gas recirculation technology discussed below focus on the technology utilised by the 1.9 litre TDI engine on the test bench, which is Euro III compliant (VAG, 2003) (Kotze, 2010). This engine is no longer in production, however according to SAPIA (2008), the South African vehicle parc is relatively old therefore the engine and its systems are likely still in use by the light passenger vehicle owners.

The fundamental principle behind the concept of exhaust gas recirculation is the substitution of a fraction of the total atmospheric intake air with recycled exhaust gas. Diesel exhaust consists of 99% carbon dioxide (CO_2), water vapour (H_2O), atmospheric nitrogen (N_2) and oxygen (O_2). The remaining fraction is composed of harmful pollutants such as carbon monoxide (CO), hydrocarbons (HC) and nitrogen oxides (NO_x) (Agarwal, et al., 2011) (Jääskeläinen, 2011).

Formation of diesel emissions during combustion

The nitrogen oxide emissions consist of nitrogen monoxide, 30,01 *g/mol* and nitrogen dioxide 46,0055 *g/mol*, with the latter being considered the more toxic of the two (Agarwal, et al., 2011) (Jothithirumal & Jamesgunasekaran, 2012). It is primarily nitrogen monoxide that forms during the combustion of diesel. The *Zeldovich Mechanism* (Zeldovich, et al., 1947) (Heywood, 1988) (Zhao, 2010) describes the formation and decomposition of nitrogen monoxide from atmospheric nitrogen at a near stoichiometric air-to-fuel ratio during combustion. The primary reactions include:

$$O + N_2 \rightarrow NO + N \quad (2)$$

$$N + O_2 \rightarrow NO + O \quad (3)$$

$$N + OH \rightarrow NO + H \quad (4)$$

Nitrogen monoxide is formed in both the flame front and post flame regions, with the post flame region producing a higher concentration of nitrogen monoxide (Heywood, 1988) (Mollenhauser & Tschoeke, 2010). The high rise in temperature and pressure during *premixed combustion* initiates the formation of nitrogen monoxide in the flame front region. This period is however very short and the flame front region very small. The bulk of the nitrogen monoxide is therefore formed during *rate controlled combustion* in the post flame region, with the high temperature levels generated by *premixed combustion* (Heywood, 1988) (Zhao, 2010).

The formation of nitrogen oxide is therefore very temperature dependent, as the following equation demonstrates (Heywood, 1988):

$$\frac{d[NO]}{dt} = \frac{6 \times 10^{16}}{T^{0.5}} \exp\left(\frac{-69{,}090}{T}\right)[O_2]_e^{0.5}[N_2]_e \quad (5)$$

The equation above also illustrates the sensitivity of nitrogen monoxide formation to the oxygen concentration present inside the combustion chamber which result in high nitrogen monoxide concentrations.

Although most of the nitrogen oxides formed during combustion is nitrogen monoxide, researchers have found that with diesel there is still a considerable fraction of nitrogen dioxide present when measured at the exhaust pipe, especially at low load conditions without exhaust gas recirculation. The reason for this is the propensity of nitrogen monoxide to convert to nitrogen dioxide by reacting with free radicals such as hydroperoxyl (HO_2), present in the exhaust gas (Heywood, 1988) (Mollenhauser & Tschoeke, 2010).

$$NO + HO_2 \rightarrow NO_2 + OH \quad (6)$$

The fraction of nitrogen dioxide decreases as the engine load increases, since the presence of cooler regions inside the exhaust manifold at low load may quench the nitrogen dioxide, preventing it from forming nitrogen monoxide in the presence of monoxide (O) (Heywood, 1988).

$$NO_2 + O \rightarrow NO + O_2 \quad (7)$$

When diesel exhaust is inducted into the engine it replaces a certain volume of atmospheric air in the total induction charge. The induction charge therefore contains less oxygen than a pure charge of atmospheric air, effectively diluting it (Jothithirumal & Jamesgunasekaran, 2012) (Ladommatos, et al., 1998). Less oxygen reduces the air-to-fuel ratio which is directly linked to the composition of the subsequent exhaust emissions (Byttner & Holmberg, 2008), as explained above.

The use of exhaust gas recirculation has unwanted consequences for diesel exhaust emissions in terms of an increase in particulate matter, hydrocarbons and carbon monoxide. Ordinarily the formation of hydrocarbons in a non-exhaust gas recirculation engine is not a concern due to diesel engines running on excess air. Hydrocarbons form when the combustion cycle is not completed due to either lack of oxygen or the walls of the combustion chamber being too cold, a phenomenon known as cold quenching (Reifarth, 2010) (Khair & Jääskeläinen, 2015). As explained above, exhaust gas recirculation dilutes the induction charge resulting in less available oxygen for combustion. With less oxygen, available for combustion, some of the diesel fuel injected into the engine does not take part in any chemical reaction and remains unburnt (Mollenhauser & Tschoeke, 2010).

Recalling section 2.2.1, it should be noted that combustion never occurs without contaminants, as the volumetric composition of atmospheric air is approximately 78,08 % nitrogen and 20,95 % oxygen with various other miscellaneous gases. This

results in carbon monoxide being formed during combustion, since not every carbon atom can bond with two monoxide atoms to form carbon dioxide.

The use of exhaust gas recirculation is therefore often complimented with the use of post treatment techniques such as diesel particulate filters (DPF) and diesel oxidation catalysts (DOC) (Reifarth, 2010) (Heywood, 1988).

The specific heat of exhaust gas is also considerably higher, due to inert gases, than that of the atmospheric induction charge leading to a lower flame temperature which in turn lowers the peak combustion temperature (Jothithirumal & Jamesgunasekaran, 2012). The formation of nitrogen oxides is virtually non-existent below 2000 K, which is one of many reasons exhaust gas recirculation has been implemented with such success in diesel engines (Agrawal, et al., 2004).

Different types of exhaust gas recirculation systems

The exhaust gas recirculation system requires only a valve and a pipe which routes a portion of the exhaust gas from the exhaust manifold to the intake manifold of the engine. Modern exhaust gas recirculation systems are much more complex because of the requirements by legislation on the manufacturers of internal combustion engines. Components of the modern exhaust gas recirculation system include control valves, heat exchangers, pumps and mass flow meters (Jääskeläinen & Khair, 2012) (van Basshuysen & Schäfer, 2004). Exhaust gas recirculation systems can be classified according to temperature and pressure.

Temperature classification refers to whether an exhaust gas recirculation system is cooled or not. Uncooled systems allow the exhaust gas to recirculate to the intake manifold without being cooled. Cooled systems, on the other hand, cools the exhaust gas to lower the induction charge temperature. The exhaust charge cooler performs the same action as an intercooler does on a turbocharger. To increase volumetric efficiency, the exhaust charge is cooled down to increase the charge density. Cooling the exhaust charge also acts to keep the combustion temperature as low as possible to minimize the formation of nitrogen oxides (Agarwal, et al., 2011) (van Basshuysen & Schäfer, 2004).

Cooling the exhaust charge too far initiates condensation, forming water droplets which have been linked to engine wear such as corrosion of the combustion chamber. To avoid condensation of the exhaust, the temperature is controlled slightly above dew point (Reif, 2014). The accurate temperature control when using an exhaust charge cooler is therefore of critical importance.

Pressure classification refers to either the *low-pressure route system* or the *high-pressure route system*. On the low-pressure route, also known as the long route (LR), the passage for the recirculated exhaust gas is located downstream of the turbine and upstream of the compressor. The power output of the turbocharger is therefore not adversely affected due to the placement of the exhaust gas

recirculation system as the entire exhaust charge is utilised to drive the compressor. This enables the use of exhaust gas recirculation under low and high engine load conditions, broadening the useable range of exhaust gas recirculation thus facilitating significant nitrogen oxide reduction (Reifarth, 2010).

The adoption of Euro VI emissions standards has led many manufacturers to adopt the low-pressure route exhaust gas recirculation systems, seen in Figure 4. The low-pressure system is often capable of higher exhaust gas recirculation rates. (Pierburg GmbH, 2013)

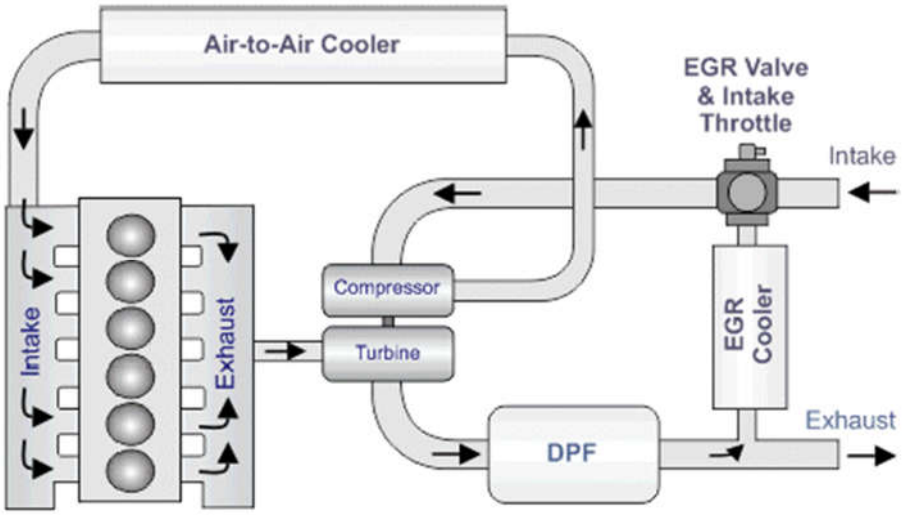

Figure 4: Low-pressure EGR system (Jääskeläinen & Khair, 2014)

The advantage/disadvantage of this arrangement is that whilst fuel economy is improved by moving the turbocharger into a more efficient part of the compressor map, the compressor must however compress both the atmospheric and EGR charges (Reif, 2014). A further drawback of this system concerns the introduction of particulate matter into the intercooler which can lead to clogging of the intercooler airways and therefore a reduction in volumetric efficiency and thermal efficiency (Jothithirumal & Jamesgunasekaran, 2012). This phenomenon is often mitigated by the introduction of a diesel particulate filter between the turbine outlet and the exhaust gas recirculation system inlet (Reifarth, 2010).

To facilitate the flow of the exhaust charge, the exhaust gas recirculation valve must be throttled to produce a sufficient pressure drop to allow the exhaust gas to be mixed into the atmospheric charge air. The positioning of the exhaust gas recirculation valve at either the exhaust exit, or the atmospheric air intake accomplishes this. It should be noted that according to Reifarth and Angstrom (2009), the fuel economy is much better with the exhaust gas recirculation valve positioned at the exhaust exit.

The long pipe length of the low-pressure route system, including the intercooler, length, responds poorly to the change in recirculated exhaust gas demand as the entire volume first must first be discharged into the intake manifold before the composition of the induction charge can be altered. The inclusion of the intercooler along with the recirculated exhaust gas cooler, this routing system increases the cooling capacity of this system leading to lower induction charge temperatures (Reif, 2014) (van Basshuysen & Schäfer, 2004).

The high-pressure route system or the short route (SR), as it is also known, passes the exhaust gas from upstream of the turbine to downstream of the compressor, seen in Figure 5. As with the low-pressure system, mentioned above, the placement of the exhaust gas recirculation valve accounts for various considerations. Placement of the valve at the cold side of the recirculated exhaust gas cooler often leads to a reduction in production costs as the materials used to produce the valve is less expensive. A valve placed on the hot side of the cooler however has a better transient response (van Basshuysen & Schäfer, 2004).

The role of variable geometry turbochargers become apparent when considering the pressure drop necessary across this exhaust gas recirculation loop to drive the exhaust gas into the intake manifold. When the turbocharger is operating at a high efficiency the pressure difference across the high-pressure route system is negligible (Jääskeläinen, 2013) (Zhao, 2010). The variable geometry turbocharger therefore must adjust alongside the exhaust gas recirculation valve, to facilitate flow. Fouling is of a lesser concern in the high-pressure route system than in its counterpart. The exhaust gas recirculation valve must still be routinely cleaned as does the exhaust charge cooler, if present (Jääskeläinen & Khair, 2014).

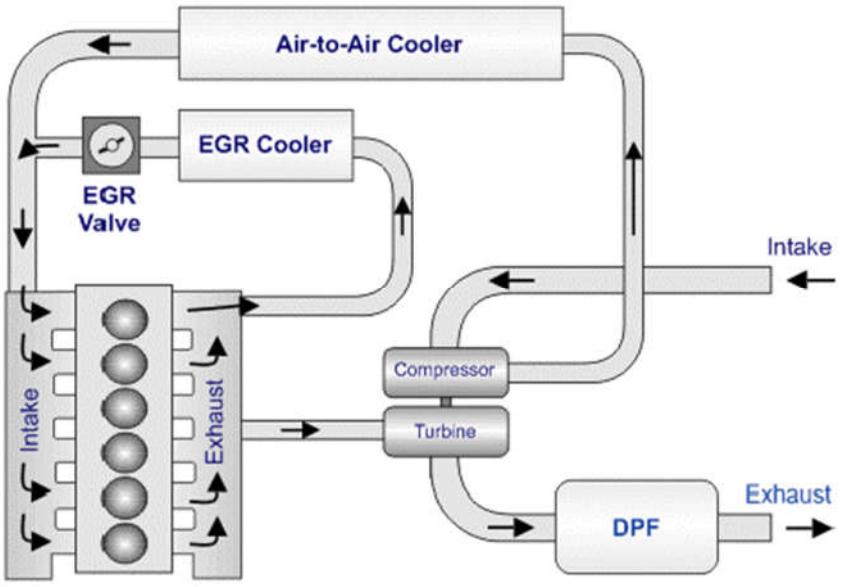

Figure 5: High-pressure EGR system (Jääskeläinen & Khair, 2014)

The simplicity of the high-pressure route system is the reason it is most commonly utilised in modern mass production engines. The short fall is that the efficiency of the turbochargers is decreased due to part of the exhaust gas being tapped off before the turbine, thus less energy is available to drive the turbine wheel. More advanced exhaust gas recirculation systems utilise both the low and high-pressure systems in a hybrid configuration to achieve the best possible efficiency across a wide array of driving conditions (Reifarth, 2010).

Exhaust gas recirculation valves

Modern exhaust gas recirculation systems make use of various components to achieve the best possible nitrogen oxide reduction whilst maintaining the highest possible engine efficiency. An important component in this system is the exhaust gas recirculation valve, mentioned before. Exhaust gas recirculation valves are actuated via pneumatics, hydraulics or electricity. Most valves utilise a poppet design, whilst more advanced valves use a rotary design (Pierburg GmbH, 2013).

Pneumatic valves are actuated by an electro-pneumatic converter which uses the control signal from the engine control unit to generate a vacuum, lifting the valve from its seat. The hysteresis encountered between the valve opening and closing has caused manufacturers to adopt other valves which respond more rapidly to changes in control signal (Jääskeläinen & Khair, 2012) (van Basshuysen & Schäfer, 2004) (Reif, 2014).

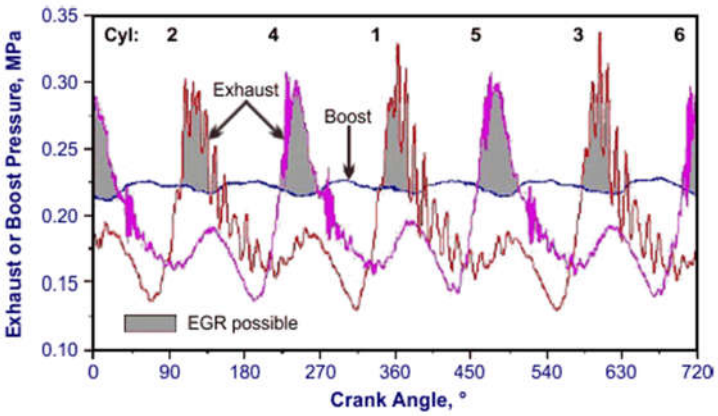

Figure 6: Exhaust versus intake pressure pulsations (Pfeifer, et al., 2002)

Due to the cyclical operation of the internal combustion engine, exhaust flow is pulsating in nature, which often leads to reverse flow in the system. Recirculated exhaust gas flow is only possible when the pressure in the intake manifold is lower than the exhaust manifold, which is why variable geometry turbochargers are often used in conjunction with the exhaust gas recirculation valves.

By closing the variable vanes on the turbine, the engine control unit can ensure that there exists a sufficient pressure drop over the exhaust gas recirculation route, to facilitate exhaust flow. Figure 6 illustrates the pulsations of a complete four-stroke

cycle and the periods when recirculated exhaust gas flow is possible (Reifarth, 2010) (Pfeifer, et al., 2002).

To negate the possibility of reverse flow occurring as often happens with poppet valves, a Reed valve can be used (Reifarth, 2010). This is a type of one-way valve that prevents reverse flow in the exhaust gas recirculation system, by closing off when there is a pressure differential that will lead to reverse flow. This valve does not need to be controlled as the actuation of the petals is controlled by the pressure differential over the valve. These valves however, present a problem when used in an exhaust gas recirculation system as they tend to clog and increase flow resistance (Jääskeläinen & Khair, 2012).

Recirculated exhaust gas flow measurement

The performance of exhaust gas recirculation is often described by the exhaust gas recirculation rate. The exhaust gas recirculation rate can be defined in two ways. First is to define the rate by volumetric means in terms of the carbon dioxide concentration present in both the intake and the exhaust, as seen below (Baert, et al., 1999).

$$EGR\ Rate = \frac{[CO_2]_{intake} - [CO_2]_{ambient}}{[CO_2]_{exhaust} - [CO_2]_{ambient}} \times 100\% \quad (8)$$

The exhaust gas recirculation rate can also be defined on a mass basis by using the total mass of recirculated exhaust gas charge and the mass of the fresh atmospheric intake charge (Jääskeläinen & Khair, 2014) (Müller, 2010).

$$EGR\ Rate = \frac{q_{m,EGR}}{q_{m,EGR} + q_{m,atmospheric}} \times 100\% \quad (9)$$

The measurement of exhaust gas mass however, presents a difficult problem. Since the fluid being measured is compressible, most methods used produce only approximations of the exhaust gas mass flow rate. The extreme pulsations in the exhaust flow produced by the engine further compounds the complexity of any attempt at measuring the exhaust flow directly. Nevertheless, researchers have attempted to do just that, as real-time measurement of the exhaust gas flow rate allows for the engine control unit to improve the transient response to changing operating conditions, thereby adjusting the exhaust gas recirculation rate more quickly to optimize the nitrogen oxide reducing process. Numeric modelling has also been employed to calculate the exhaust gas recirculation rate (Patane, et al., 2016) (Buenaventura, et al., 2013) (Olin, 2007) (Wahlström & Eriksson, 2011).

The flow rates of fluids are measured using a variety of different measures. Restriction flow meters are examples of the classical way of measuring the flow rate of a fluid. These flow meters are classified as differential pressure flow meters and are among the most widely used flow meters in both the industry as well as

laboratory setups due to their design simplicity and affordability (Laurantzon, 2010). A variety of different devices use this principle such as the orifice plate, the venturi tube, and the nozzle. Other differential flow meters include the laminar flow meter and the Pitot tube meters.

These flow meters are mostly utilised for steady, incompressible, laminar mass flow measurements, since turbulent flow and high-pressure ratios introduce high degrees of uncertainty to the calculated mass flow. This makes restriction flowmeters difficult to implement in exhaust gas recirculation systems as a method to obtain the charge flow rate since exhaust flow is turbulent and highly pulsating (Laurantzon, 2010).

Nevertheless, there are studies which have attempted to utilise this method even though restriction flowmeters lead to a loss in pressure as opposed to the more expensive yet nonintrusive methods such as ultrasonic (Olfert & Checkel, 2007) and electromagnetic flow measurements.

Restriction flow meters use Bernoulli's equation and total mass flow through a cross section to determine the flow speed of the fluid through the flow meter. (Laurantzon, 2010). The pressure drop through the restriction is related to the flow speed via the Bernoulli equation, Equation (10) (Cengel & Cimbala, 2006),

$$\frac{p}{\rho} + \frac{1}{2}c^2 + gz = Constant \tag{10}$$

and the mass flow rate, q_m, for a constant density fluid, is then determined by the continuity equation, Equation (11) (Cengel & Cimbala, 2006).

$$q_m = \rho c A \tag{11}$$

To obtain the mass flow rate between two points along a streamline in a restriction flow meter, the above equations are combined to give (Cengel & Cimbala, 2006):

$$q_m = A_2 \sqrt{\frac{2\rho(p_1 - p_2)}{(1 - (A_1/A_2)^2)}} \tag{12}$$

$$= A_2 \sqrt{\frac{2\rho(p_1 - p_2)}{(1 - (d_1/d_2)^4)}} \tag{13}$$

The above equation, Equation (13), is the idealized form, neglecting any loss. To adjust it to real world applications a discharge coefficient, C_d, is introduced to approximate the real mass flow rate considering any energy losses. Since exhaust gas is mainly comprised of air, an expansibility factor, ε, also needs to be introduced to account for the compressibility of the fluid. To simplify the design process of

any restriction flowmeter the diameter ratio, d_1/d_2, is expressed as β. Equation (13) is then expressed as Equation (14) (Cengel & Cimbala, 2006):

$$q_m = C_d \varepsilon A_2 \sqrt{\frac{2\rho(p_1 - p_2)}{(1 - (\beta)^4)}} \tag{14}$$

The values for the discharge coefficient and the expansibility factor can either be determined experimentally (Cengel & Cimbala, 2006) or referenced form various standards for restriction flowmeters such as ISO 5167-1 (2003).

In terms of design, the *orifice plate* is the simplest in design. Figure 7 shows its construction which comprises of a plate perpendicular to the direction of flow, with a circular hole, concentric to the inside diameter of the pipe. Depending on its application the edges of the hole may either be sharp, bevelled or rounded, which influences the discharge coefficient.

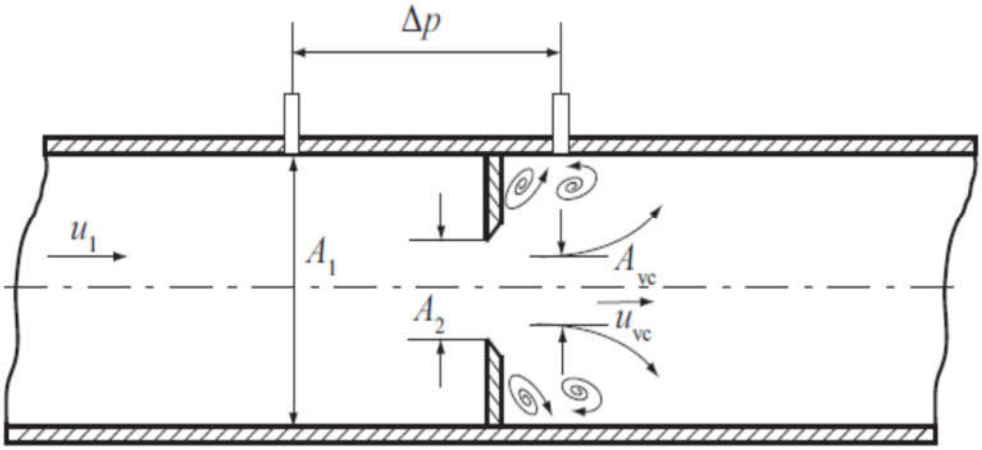

Figure 7: Orifice plate (Laurantzon, 2010)

Orifice plates have a significant permanent pressure loss over the plate owing to the sudden change in flow area, which induces swirl and separated flow as the fluid passes through the orifice, making its implementation to a high-pressure exhaust gas recirculation system difficult. This is due to the high-pressure system relying on a high recirculated exhaust pressure to drive the exhaust gas charge into the intake manifold to replace a portion of the atmospheric charge.

This effect can be mitigated using a *nozzle* instead of a plate, as shown in Figure 8. The gradual change in flow area reduces the pressure loss through the nozzle by mitigating the effects of swirl and separated flow.

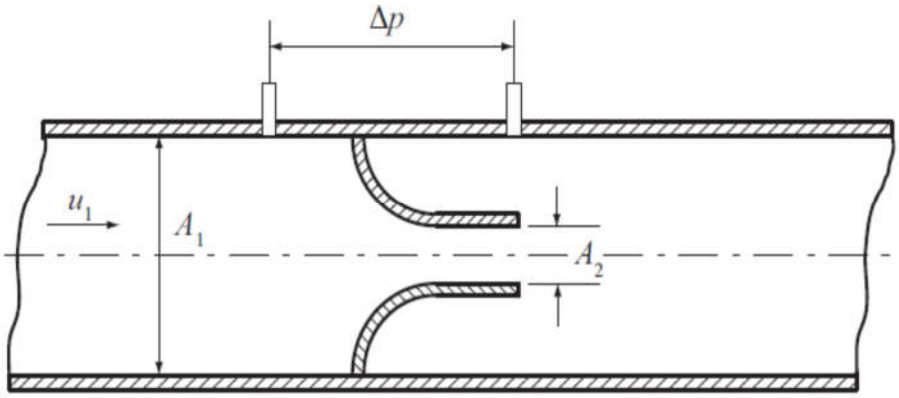

Figure 8: Nozzle meter (Laurantzon, 2010)

The venturi tube, seen in Figure 9, eliminates swirl and separation of flow by means of gradual convergent and divergent sections. The permanent pressure loss across the device is therefore minimal with only minor frictional losses impacting pressure recovery. It also boasts the best discharge coefficient of the three mentioned devices when manufactured according to standards (ISO 5167-4, 2003)

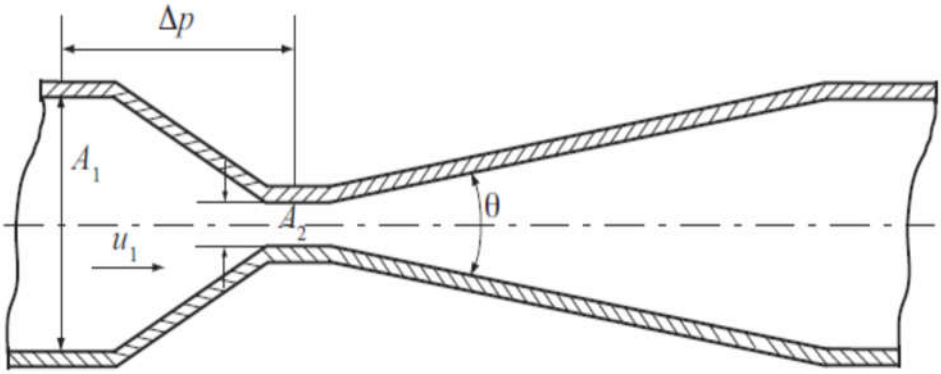

Figure 9: Venturi tube (Laurantzon, 2010)

The cost of each of these meters however, rise as the manufacturing requirements of each successive meter becomes more complicated as is evident when comparing the orifice, nozzle and venture tube meters (Cengel & Cimbala, 2006).

Using differential pressure transducers/transmitters is acceptable when acquiring steady state flow measurements. The pulsating nature of exhaust flow must be addressed appropriately when taking differential pressure measurements which often utilise tubes to differentiate between two pressure tapping locations introducing a time lag in acquiring the pressure measurement. If a high degree of

accuracy is required for instantaneous pressure measurements, then flush mounted absolute pressure transducers/transmitters must be considered to mitigate any acquisition lag whilst sampling (Laurantzon, 2010).

The difficulty in measuring exhaust flow is further compounded by the very nature of its composition. The particulate matter present in exhaust gas has a propensity to adhere to any surface, thus making any form of flow measurement using a device inserted into the flow stream, such as the laminar flow meter and Pitot tube or annubar, problematic as they would have to be cleaned regularly.

The laminar flow meter can however be used for the measurement of the atmospheric air intake charge, as the flow stream can be filtered, mitigating the effect fouling can have on a device with a honeycomb structure to straighten the gas flow (Cengel & Cimbala, 2006).

Section 3.2 addresses the selection of flow meters to measure the recirculated exhaust gas charge and the atmospheric air intake charge.

2.2.3. Forced induction

Forced induction is accomplished by using either a turbocharger or a supercharger. Both devices compress the inlet air to force a higher mass of air, than in a naturally aspirated engine, into the combustion chamber, hence the name. The higher density air inside the cylinder allows for more fuel to be combusted. The result is more energy released per cylinder during each combustion cycle which in turn results in more overall engine power (Nice, 2000).

To aid in conciseness of this review only the turbocharger is reviewed. The turbocharger sections consist of a turbine and compressor connected by the centre housing.

Turbocharger construction

To facilitate the explanation of the expansion and compression processes in the turbocharger, the general construction is first considered. Figure 10 shows a sectioned turbocharger, revealing the internal construction of a turbocharger. The turbine section consists of the flow inlet followed by the spiralling channel called the volute. The volute's cross section area decreases, accelerating the flow, until it reaches the stator, which induces swirl in the flow, allowing it to impart torque to the rotor, also known as an impeller (Zhao, 2010) (Jääskeläinen & Khair, 2016).

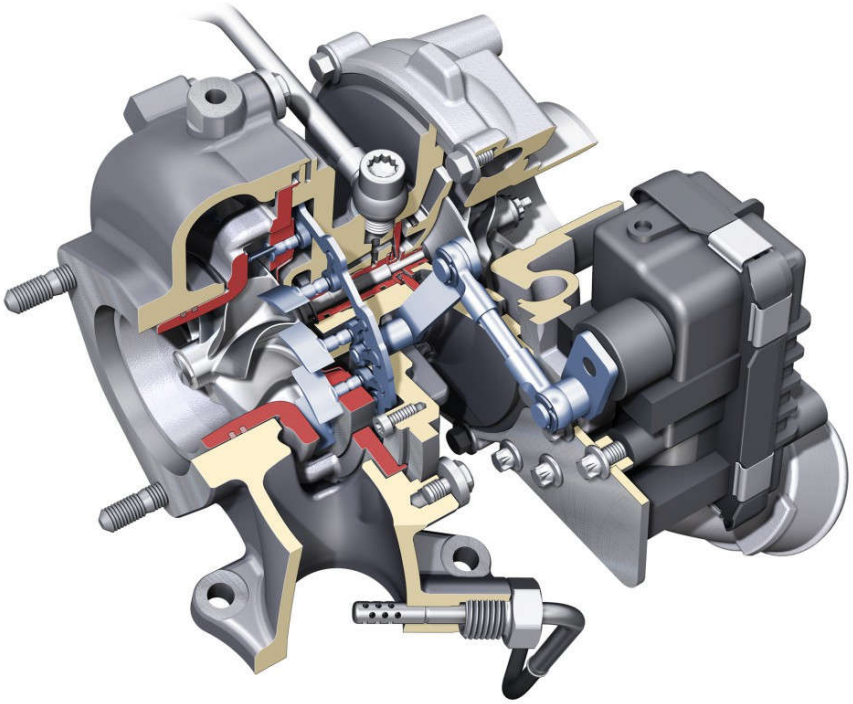

Figure 10: VGT construction (Audi AG, 2016)

The impeller converts the torque into shaft power for the turbine output shaft. Once the flow passes through the impeller, it exits to the diffuser, which converts the remaining kinetic energy to static pressure. Heat resistant materials such as cast iron and stainless steel are used in the manufacturing of the turbine housing, due to the high temperature of the exhaust gas (Hiereth & Prenninger, 2007). The rotating components such as the impeller and shaft are mainly manufactured using aluminium due to its light weight and excellent machinability (Jääskeläinen & Khair, 2016).

The centre housing contains the support system for the turbine-compressor common shaft comprising of bearings and seals. The centre housing is most commonly manufactured form cast iron, but aluminium has also been known to be used in special applications (van Basshuysen & Schäfer, 2004). It is important to note the role of the bearings and seals in the centre housing of the turbocharger. The bearings in the turbocharger must control the radial and axial movement of the turbocharger shaft and wheels whilst at the same instance minimize any frictional losses between the turbine and compressor due to the extreme rotational speeds of the shaft at high engine speeds. The bearings are lubricated with oil which also acts as a heat transfer medium (Jääskeläinen & Khair, 2016) (Zhao, 2010).

The primary purpose of the seals are to prevent the exhaust and intake air from escaping through the base of both turbine and compressor housings. They must deal with the high temperature and pressure related to the operation of the turbocharger and therefore the centre housing often has cooling channels when the lubrication

oil proves insufficient in reducing the operating temperature. Deflectors and flingers are responsible for preventing the oil from escaping into the turbocharger housings, not the seals (Jääskeläinen & Khair, 2016).

The inlet of the compressor section starts at the centre of the compressor housing, aligned with the compressor shaft. As the charge flows from the inducer through the rotor/impeller, it makes a 90° turn into the exducer which pushes the charge through a narrow diffuser into the volute, with an increasing cross-sectional area from the diffuser to compressor exit. The volute of the compressor converts velocity into static pressure (Hiereth & Prenninger, 2007).

Turbine operating principle and design

The principle of operation behind the turbine is to use the energy from the exhaust gas flow to drive the turbine. The exhaust gas flow through the turbine is adiabatic and ideally isentropic. The enthalpy of an ideal gas is only dependent on time and therefore represents the maximum obtainable efficiency for the energy transfer in a turbine. Figure 11, shows the deviation of the actual expansion process from the ideal by an increase in entropy. The increase in entropy and correlating decrease in enthalpy is caused by several sources in the turbine such as the inlet, stator, rotor, diffuser and the exit which cause energy losses (Hiereth & Prenninger, 2007).

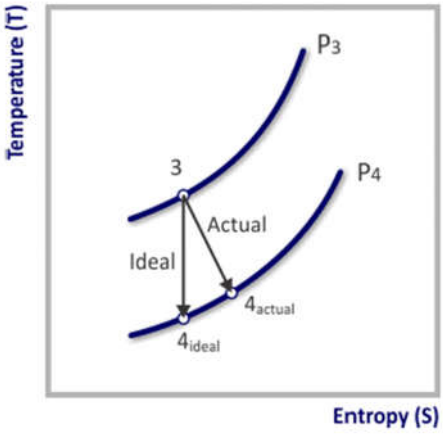

Figure 11: Ideal versus actual expansion process (Jääskeläinen & Khair, 2016)

A general design approach for the inlet of the turbine, is to design it as large as possible reducing the velocity of the flow as much as possible to minimize frictional losses. Radial flow turbochargers, found on most modern production vehicles, have higher losses than axial flow turbochargers due to the tangential turning of the flow and the acceleration through the volute. Frictional losses are also more severe due to the increased flow length (Jääskeläinen & Khair, 2016).

Stator losses are caused primarily by friction within the vanes, elaborated upon below, but minor losses also occur due to the flow being redirected towards the

impeller. The accumulation of particulate matter on the vane surfaces may lead to blockages which increase exit losses on the trailing edges of the vanes. In addition to the same frictional losses experienced by the stator, the rotor must contend with efficiency issues due to tip clearance which may lead to windage losses (Hiereth & Prenninger, 2007). If the tip clearance between the turbine housing and the impeller blade shroud edge is too large, the flow leaks from the high-pressure side of the blade to the low-pressure side of the blade. The torque delivered to the shaft is consequently reduced due to the reduced tangential force acting on the impeller blades (Jääskeläinen & Khair, 2016).

Turbine designs can vary greatly depending on its intended application. Traditional turbochargers have a fixed geometry, where the stator has a fixed inlet area to direct the exhaust flow towards the impeller. This can be accomplished by stationary vanes equally spaced around the perimeter of the stator. The problem with using a fixed geometry turbine is its efficiency across a wide range of inlet flow conditions.

The limitations of fixed geometry turbines are that each turbine has a specific speed range in which it performs as intended. Large turbines perform well at high engine speeds whereas smaller turbines perform better at lower engine speeds. This problem was first brought about when manufacturers started producing smaller turbochargers to reduce turbo lag. Large turbochargers had a delay in delivering the intended boost required of the turbocharger at low engine speeds. This is due to the inertia of the moving parts that need to be overcome (Hiereth & Prenninger, 2007).

The simplest solution to reduce the inertia of the turbochargers was to design smaller turbochargers with smaller turbines. The problem with this solution however is that the smaller turbochargers tend to choke on the excess exhaust gas flow delivered at higher engine speeds. This excess exhaust gas flow produced by the engine therefore needs a waste gate or a bypass to avoid over-boost and over-speeding of the turbocharger at higher engine speeds. The waste gate or bypass however, lowers the overall efficiency of the turbocharger (Nice, 2000).

More advanced solutions call for the installation of multiple turbochargers, each to deal with a separate engine speed range. These designs are not only costly and technically difficult to implement but also adds unwanted mass to the overall engine design.

This lead to the design of the variable geometry turbocharger (VGT). The design of a variable geometry turbocharger functions on the principle of varying the inlet flow area to the turbine impeller. This can be accomplished by various designs such as the moving wall, sliding ring, variable area and variable vane designs which all vary the inlet flow area to the turbine impeller using different methods. The flexibility of a variable turbocharger is therefore drastically better as opposed to a fixed geometry turbocharger when considering the applicable engine speed range for a single turbocharger versus multiple turbochargers, regardless of the design used (Jääskeläinen, 2013) (Feneley, et al., 2017).

The design of the variable geometry turbocharger enables it to handle all the exhaust flow without a bypass route, as mentioned previously. On engines fitted with exhaust gas recirculation, discussed in section 2.2.2, the variable geometry turbocharger fulfils another important role in regulating the exhaust backpressure, which drives the exhaust gas through the recirculation route into the intake manifold (Jääskeläinen & Khair, 2011) (Hiereth & Prenninger, 2007).

The variable vane design, such as the variable geometry turbocharger design featured on the engine test bench, consists of a series of vanes equally spaced on a certain pitch circle diameter, as shown Figure 12. These vanes vary the inlet flow area by rotating around the individual pivots holding the vanes in place. These pivots are secured by an annular ring surrounding the outside perimeter of the turbine wheel (Jääskeläinen, 2013). At low engine speeds with minimal exhaust gas flow the vanes have a very small inlet area, whereas at high engine speeds with maximal exhaust gas flow, the actuator shown in the figure above, rotates the pivots to maximise the inlet flow area (Arnold, 2004) (Carter, et al., 2010) (Hawley, 1991).

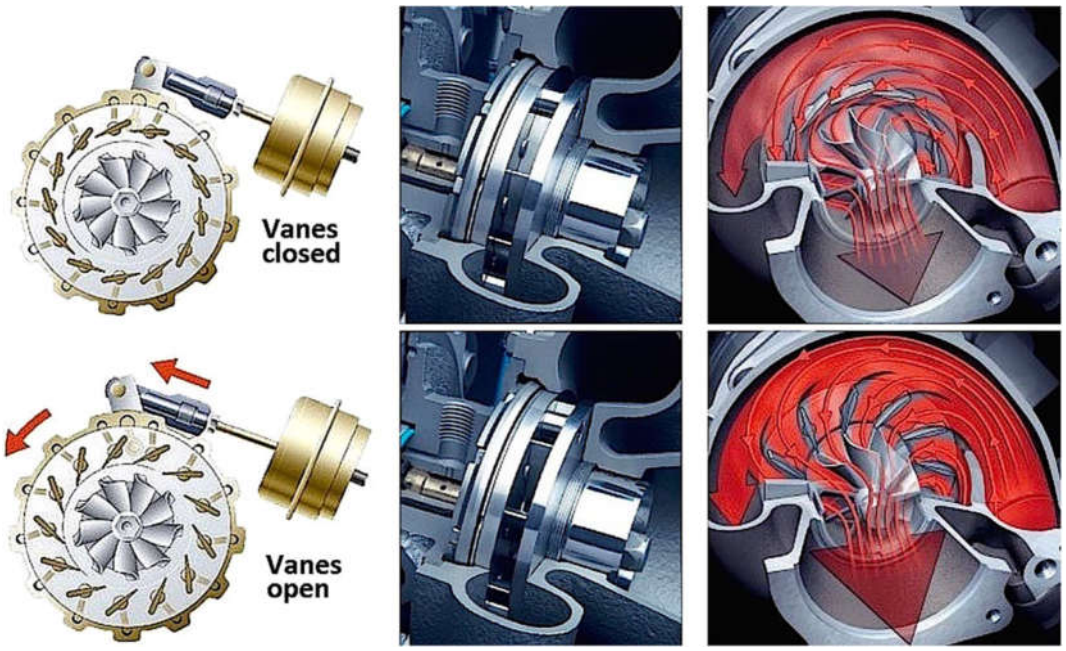

Figure 12: Variable vane design (Feneley, et al., 2017)

The pivoting of the vanes not only alter the inlet flow area but also changes the angle at which the exhaust flow enters the impeller. With a fixed exhaust flow, it is the angle of the vanes that control the speed of the turbine impeller, with the open position ensuring the maximum attainable impeller speed. Due to the pivoting action of the vanes, the clearance between the vanes and turbine impeller varies thus inducing unwanted losses. The vanes are also prone to vibration under high flow conditions (Jääskeläinen, 2013). The variable vane design is however, one of the most utilised designs in the automotive industry.

Compressor operating principle and design

To understand the complexities of the compression process, a few basic principles are first discussed. Figure 13, illustrates the difference between an ideal and actual compression process. The ideal process is considered isentropic, with the change in enthalpy being a function of temperature only.

Due to several inefficiencies, the actual compression process consumes more energy, leaving the charge air with a higher temperature than the ideal compression process. Any designed intercooler therefore requires a higher cooling capacity to account for the inefficiencies of the actual compression process (Baines, 2005).

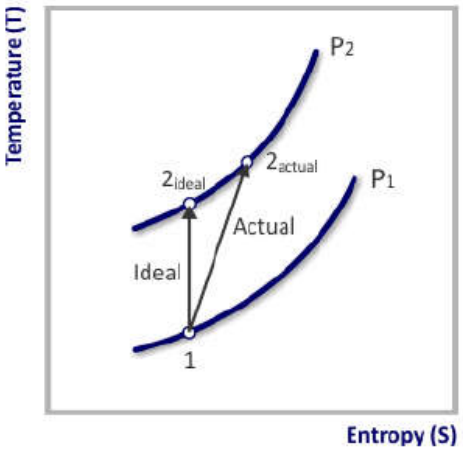

Figure 13: Ideal versus actual compression process (Jääskeläinen & Khair, 2016)

To compress the charge entering the the compressor, kinetic energy needs to be imparted to the charge. This is accomplished by the compressor wheel, which accelerates the charge to very high speeds. As the charge passes through the impeller blades on the compressor wheel, the cross sectional area it flows through increases, converting some of the kinetic energy imparted to the flow to static pressure whilst additional energy is simultaneously being added to the flow.

Once the flow exits the compressor wheel no more energy is imparted to the charge. The remaining kinetic energy must be converted to static pressure by the diffuser and volute sections of the compressor (Jääskeläinen & Khair, 2016).

The design of the compressor wheel in a turbocharger is important to the application, as the shape of the blade profile can significantly impact durability and performance. As mentioned previously, there are significant losses associated with the flow of the charge through the compressor wheel.

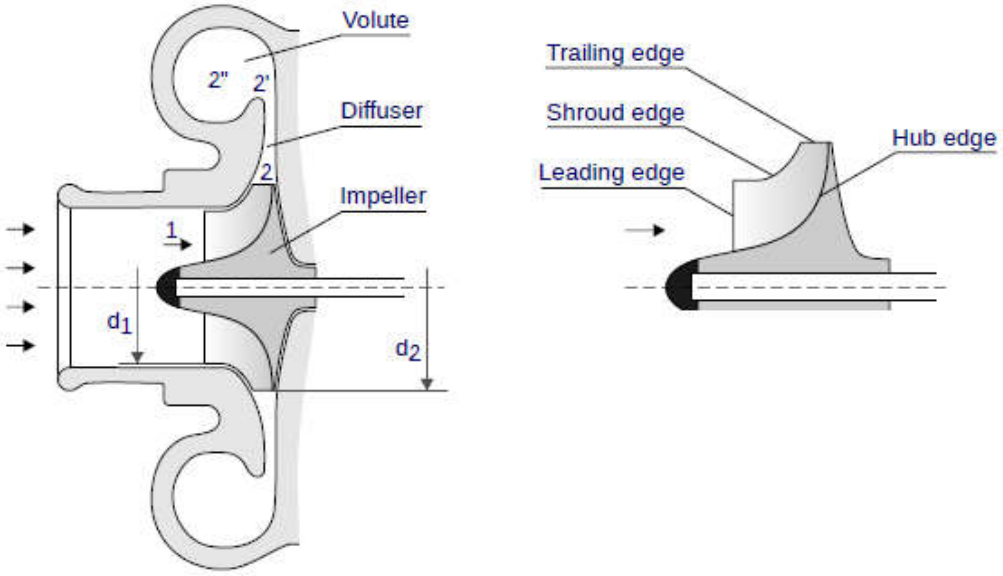

Figure 14: Cross section of radial flow compressor (Jääskeläinen & Khair, 2016)

Figure 14 illustrates a cross section of a radial flow compressor. Note the three regions on the compressor wheel. The leading edge is designed for scooping up the the charge whilst the trailing edge must propel the charge out radially after the flow has changed direction and accelerated through the blade length (Golloch, 2005). For optimal flow guidance along the impeller, compressor blades benefit from a higher blade count than is typically used in turbines. The reduced inlet area between blades at the leading edge may however cause choking. One solution to this problem is splitter blades, as seen in Figure 15 (Golloch, 2005).

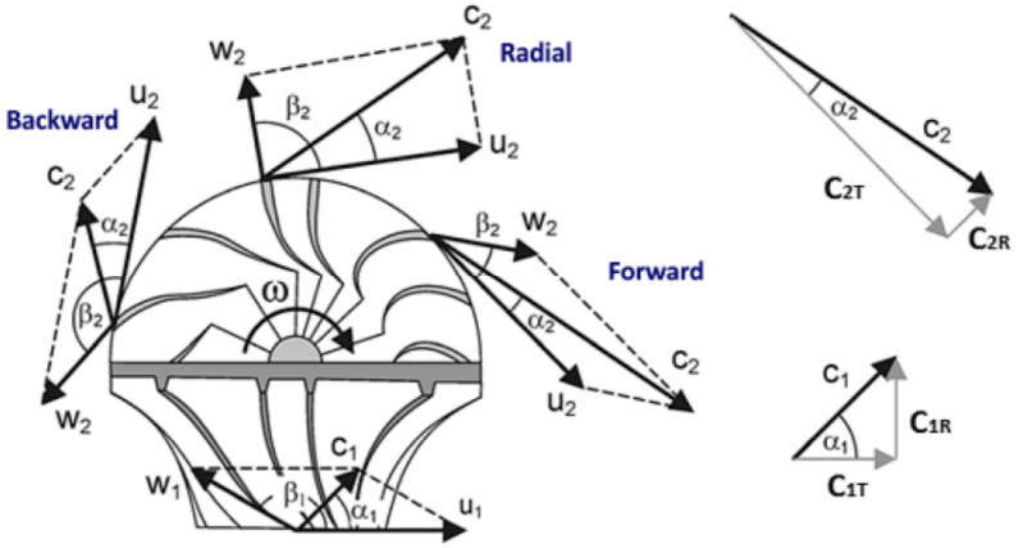

Figure 15: Different compressor wheel blade designs (Golloch, 2005)

Different profiles for the trailing edge of the blades affect the performance of the compressor in unique ways. From a performance standpoint, the optimal curvature on the trailing edge would be the backwards profile when considering efficiency. Backwards curved blades unfortunately suffer from a sharp decrease in pressure ratio for any given flow rate as opposed to the radial curvature. The blades of the impeller have very tight tolerances which are often accomplished by using an abradable soft coating on the surface of the blades that wears away on contact with the outer housing of the compressor. This ensures that the blade clearance is kept to a minimum to ensure the reverse flow is kept to a minimum (Jääskeläinen & Khair, 2016).

Compressor mapping

Compressor mapping is a tool engineers use to optimize the control of either a fixed or variable geometry turbocharger. A good approximation is to consider the compression process to be isentropic. The efficiency of the turbocharger determines how closely the turbocharger approximates the ideal model (Jääskeläinen & Khair, 2016).

The actual outlet temperature of the compressor is higher than the ideal model due to various inefficiencies that can be traced to primarily to the design of the compressor wheel (Honeywell, Garrett, 2017).The flow limits are defined by *surge* and *choking* for the low and high limits respectively.

Surging occurs when the air flow separates at the low-pressure side of the blade near the inlet due to a very low angle of departure from the blade tip. This causes the pressure in the diffuser to decrease below that of the inlet pressure whereupon the flow reverses. Eventually the pressure in the diffuser drops enough for the flow to rectify itself and discharge to the compressor outlet (Jääskeläinen & Khair, 2016) (Hiereth & Prenninger, 2007). The surge line encompasses the upper limit of the compressor operating envelope as seen Figure 16 (Honeywell, Garrett, 2017).

Choking is reached when the air velocity becomes too great for the flow to remain attached to the blades. Flow separation occurs between the impeller blades which narrow the flow area between the blades until the flow becomes blocked, at a Mach number of one (Jääskeläinen & Khair, 2016). No amount of increase in compressor wheel speed will increase the mass flow at this point. For any constant compressor wheel speed, represented by the curves seen in Figure 16, the maximum mass flow rate is determined at the critical pressure ratio of one (Hiereth & Prenninger, 2007).

Manufacturers specifically tune their compressors to avoid sonic flow therefore the choke line is often drawn at the edge of an efficiency island. For Garrrett turbochargers the choke line is set to fifty-eight percent efficiency (Honeywell, Garrett, 2017).

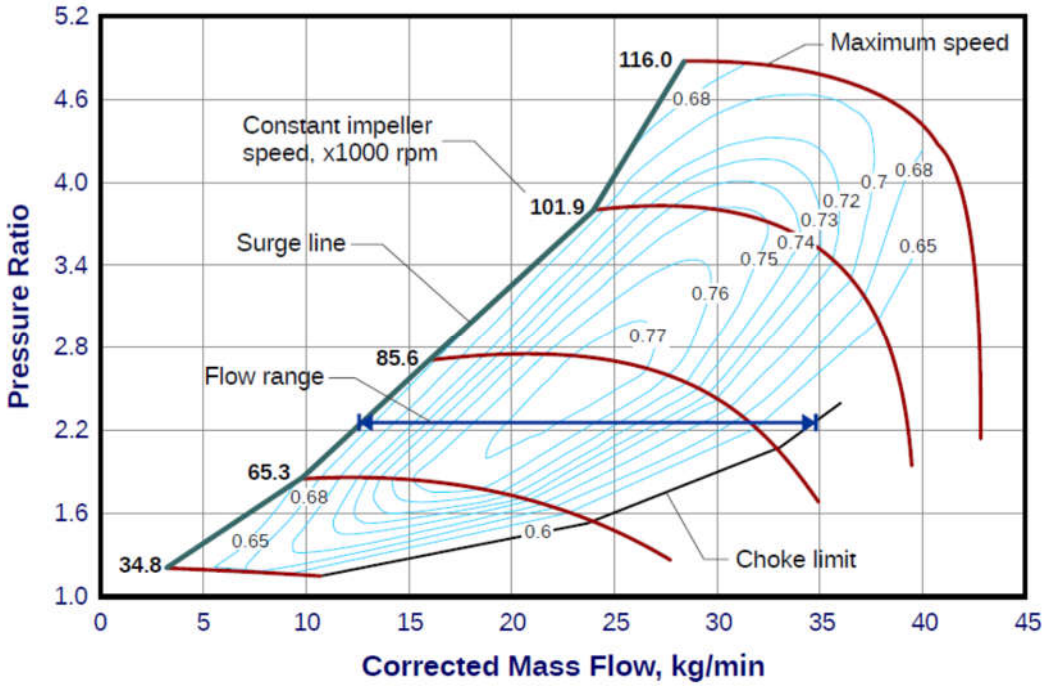

Figure 16: Typical compressor map (Jääskeläinen & Khair, 2016)

Compressor maps indicate the mass flow rate versus pressure ratio. The surge line, choke limit and the maximum compressor wheel speed encompass the turbochargers operating envelope as shown in Figure 16. *Efficiency islands* are the concentric regions contained inside the operating envelope (Honeywell, Garrett, 2017). The highest efficiency is achieved in the centre of the envelope, as seen above. The calculation of compressor efficiency can be done according to Equation (15) (Nguyen-Schäfer, 2015).

$$\eta_{compressor} = \frac{\left(\frac{p_{2t}}{p_{1t}}\right)^{\left(\frac{\kappa-1}{\kappa}\right)} - 1}{\left(\frac{T_{2t}}{T_{1t}}\right) - 1} \tag{15}$$

To compile a compressor map for a turbocharger, on an engine test bench, requires extensive experimental runs of the engine and turbocharger to determine the operational envelope within which the turbocharger can operate safely. This is a difficult task since, repeated surging inside the turbocharger can lead to damaging the compressor.

The challenges are compounded when determining the envelope for a variable geometry turbocharger since the position of the variable vanes affect the speed of the turbine impeller and therefore the compressor wheel (Jääskeläinen & Khair, 2016).

Compressor speed sensors

Compressor wheels are light-weight and precision balanced to ensure optimal operation. It is therefore not advised to measure the compressor wheel speed by any physical mechanical means such as a shaft encoder or variable reluctance speed sensors. Contactless sensors are more desirable when measuring the compressor wheel speed.

Passive eddy current sensors use a permanent magnet to produce a permanent magnetic field. As the compressor blades pass through the magnetic field they induce eddy currents, allowing a coil or inductor to detect each blade. This type of sensor requires no excitation source (Jaquet, 2016).

Active eddy current sensors use an inductor-capacitor (L-C) circuit to induce eddy currents in the compressor blades. This is accomplished by the discharge of the capacitor to the inductor, which creates a magnetic field, until the capacitor voltage reaches zero. The current will continue flowing due to the inductors resistance to current change, allowing it to charge the capacitor with a voltage opposite of the original charge by reducing the magnetic field of the inductor. This reaction is repeated in perpetuity or until the internal resistance of the circuit diminishes the oscillations. The active component is thus introduced as an excitation source which ensures the oscillations continue. The oscillation frequency of this circuit is altered as a blade passes the sensor thereby producing an electrical signal used to calculate the speed (Jaquet, 2016).

Inductor-resistor (L-R) circuits are also used to measure speed. These circuits consist of an excitation source and an inductor. The inductor has a time constant depending on the inductance and internal resistance of the coil. The time constant is measured by a time-to-digital converter. A change in the time constant will produce a pulse from the time-to-digital converter. As the compressor blade passes the coil, the inductance of the coil will change leading to a change in the time constant of the circuit. The change in inductance is influenced by the type of metal the compressor wheel is manufactured from (ACAM, 2015).

The above sensor technologies all use high precision digital signal processing units to amplify and use the signal obtained from the sensor to calculate the speed. The sampling rate of these devices are also very high allowing for the accurate detection of speeds up to 320 000 *RPM*.

Advantages to these sensor technologies are that they rely on magnetic fields, making them immune to errors caused by common fouling. Disadvantages may include the requirement for the compressor wheel to be manufactured from a conductive material such as aluminium or titanium, limiting its use.

2.3. Summary

Numerous studies have been done on the mixing of different crude derived and organic fuels and the effect they have on the performance and emissions of compression ignition engines. Biodiesel-diesel blends generally exhibit higher peak in-cylinder pressures and increased heat release rates when combined with exhaust gas recirculation. Brake specific fuel consumption in general increases due to the lower calorific value of biodiesel-diesel blends. Nitrogen oxides and carbon dioxide emissions show an increase and correspondingly a decrease in particulate emissions with biodiesel blended fuels (Liaquat, et al., 2013) (Can, et al., 2016) (Zhang & Balasubramanian, 2016).

Ethanol-diesel blends suffer from instability in the presence of water and have a flashpoint comparable to that of petrol. Soot, carbon dioxide and nitrogen oxides emissions decrease with the addition of ethanol to crude derived diesel. The brake specific fuel consumption however increases for increased ethanol content (Datta & Mandal, 2016) (Ghadikolaei, 2016) (Lei, et al., 2011) (Jääskeläinen, 2016).

The formation of nitrogen oxides during combustion on an engine with exhaust gas recirculation is primarily due to the dilution effect, with the thermal and chemical effects to a lesser degree (Ladommatos, et al., 1998). High pressure exhaust gas recirculation systems are most widely used today in large scale production due to their simple design which often only comprise of a pipe and pneumatic poppet valve (van Basshuysen & Schäfer, 2004). The flow through these valves can be measured or modelled in a variety of different ways, but literature suggests the venturi tube has been implemented with some success in assisting with determining the exhaust gas recirculation rate (Laurantzon, 2010) (Jääskeläinen & Khair, 2014).

Turbocharging proves an effective measure in boosting engine performance by inducing a compressed charge into the engine (Mollenhauser & Tschoeke, 2010). It also serves to ensure that the pressure differential required for a high-pressure exhaust gas recirculation to function correctly is maintained by use of variable vane technology to control the boost pressure (Reif, 2014) (Jääskeläinen & Khair, 2014).

Advancement in compressor speed sensor technology has seen widespread adoption in the automotive industry. The technology can aid in more precise engine control and thereby improved performance and reduced emissions (Jaquet, 2016). It is also useful in determining the compressor map of any given compressor.

3. DIESEL ENGINE MEASUREMENTS

The development of the 1.9 litre TDI engine test bench consists of various stages, including partial dismantling of the engine test bench to install the new upgrades and to optimize the setup in terms of simplicity and safety. The process of refurbishing the engine test bench setup including the dynamometer, fuel conditioning unit intercooler, throttle unit, driveshaft coupling modification and cooling water supply circuit is discussed in Appendix A.

In this chapter, the previous measurement setup is discussed briefly as well as the new additions to the engine test bench, since these additions aim to expand on the measurement capabilities of the engine test bench further. These additions include the instrumentation of the variable geometry turbocharger and exhaust gas recirculation systems as well as an upgraded version of the LabVIEW measurement program developed by Blom (2015).

3.1. Overview of the setup

The measurement capabilities of the TDI test bench Kotze (2013) developed consisted primarily of in-cylinder pressure measurement and engine crank angle position measurement. Blom (2015) expanded upon the capabilities by including emissions analysis to the test bench. The previous setups used LabVIEW to acquire and record in-cylinder pressure and crank angle position data. The emissions data recorded by (Blom, 2015), was obtained by manually recording the data from standalone emissions analysers. For this project, the LabVIEW acquisition software is expanded further to obtain data from the exhaust gas recirculation and turbocharger systems.

This data is obtainable via the VCDS (Vag-Com Diagnostic Software) package linked to the original equipment manufacturer (OEM) engine control unit via USB interface. It is possible to log and save data obtained from the engine control unit in VCDS to a file, however there are limitations to this approach. The data obtained is logged according to time and it would therefore be difficult to compare the logged data to the data obtained from the LabVIEW program, which logs data according to the crank angle position of the engine. Further limitations include the lack of temperature, pressure and compressor wheel speed. All expanded measurements are incorporated into one interface, thereby eliminating any discrepancies that may occur due to comparing data obtained from more than one interface. This includes the measurements for the exhaust gas recirculation system and the variable geometry turbocharger.

Various parameters are useful in characterising exhaust gas recirculation and turbocharger systems. Temperature and pressure are the most widely used in the industry to from part of a good control strategy incorporating exhaust gas recirculation systems. More advanced systems incorporate exhaust gas flow sensors as well as exhaust gas composition sensors to measure the intake and recirculated

exhaust charges, specifically nitrogen oxides and oxygen (Jääskeläinen, 2016). Mass air flow (MAF) and manifold absolute pressure (MAP) sensors are primarily used by the engine control unit to monitor the intake charge air of the engine. These sensors typically include temperature sensors in addition to their primary measured parameter.

Monitoring actuators, specifically the exhaust gas recirculation valve and the variable geometry turbine vanes is often accomplished by displacement sensors. These sensors can also aid in detecting any actuators faults by recording the actual actuation position and comparing it to the position specified by the engine control unit (Jääskeläinen, 2016).

To determine the thermodynamic characteristics of a gas flow, the total pressure, static pressure and the static temperature must be determined. This can become a complex procedure as it is not always feasible to install several sensors in one location, as this will disturb the flow and possibly impact the operating characteristics of the device being measured in unpredictable ways, such as a probe close to the inlet of a turbine on a turbocharger.

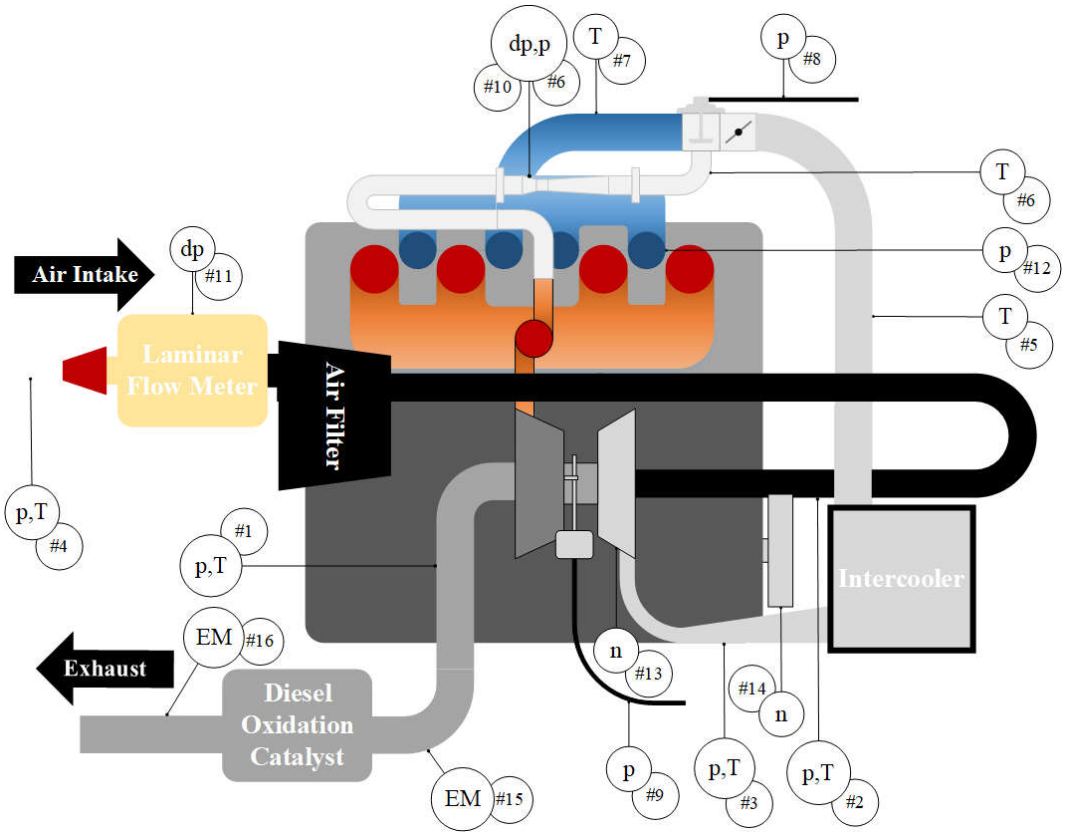

Figure 17: Sensor layout on the 1.9L TDI

The expanded measurement setup consists of two sections, namely the exhaust gas recirculation section and the variable geometry turbocharger section. The parameters measured are primarily pressure and temperature. In addition to this, the compressor wheel speed of the variable geometry turbocharger is also measured. The actuation of the exhaust gas recirculation valve and the vane adjustment of the turbine is measured by characterising the displacement against pressure. Figure 17, shows the layout of the sensors used to obtain the measurements. Table 3 lists the positions measured as well as the measurement type of the sensors used to acquire the measurements. The following sections detail the considerations when selecting the appropriate instrumentation for each application.

Table 3: Measuring points on the experimental setup

#	**Position**	**Measurement type**
1	Turbine outlet	Pressure, Temperature
2	Compressor inlet	Pressure, Temperature
3	Compressor outlet	Pressure, Temperature
4	Atmosphere	Pressure, Temperature
5	Post intercooler	Temperature
6	EGR charge	Pressure, Temperature
7	Intake manifold	Temperature
8	EGR valve vacuum line	Pressure
9	VGT actuator vacuum line	Pressure
10	EGR venturi tube	Differential pressure
11	Air intake laminar flow meter	Differential pressure
12	Cylinder	Pressure
13	Compressor wheel	Rotational speed
14	Crank shaft	Position
15	Pre-diesel oxidation catalyst	O_2, CO, CO_2, NO_X emissions
16	Post diesel oxidation catalyst	Smoke emissions

3.1.1. Temperature

When taking any temperature measurement, it is important to consider the effect the sensor has on the actual value. Any measurement must be reproducible and comparable to other similar engine test bench setups. Static temperature is measured at the wall in internal flows, where the gas velocity is zero. Measuring static temperature in internal flow presents difficulties however, as the sensor probe is prone to errors induced by heat transfer from the surrounding wall material (Zvizdić, 2014). An important parameter to consider therefore, is the total or stagnation temperature, defined as the temperature at a point in a flow field where the local velocity of the fluid is zero.

The total temperature measurement, is the sum of the static and dynamic temperature measurements, as shown by Equation (16) (Nguyen-Schäfer, 2015). In internal gas flow, the total temperature is measured by an ideal probe inserted into the ideal flow which brings the flow to rest, converting the kinetic energy into internal energy thus adiabatically increasing the local temperature measured at that point (Benson, 2014). The static temperature is then obtainable via the isentropic gas equation, seen in Equation (17) (Nguyen-Schäfer, 2015).

$$T_t = T_s + T_d = T_s + \frac{c^2}{2\,c_p} \tag{16}$$

$$T_s = T_t \left(\frac{p_t}{p_s}\right)^{(\kappa-1/\kappa)} \tag{17}$$

The application of Equation (17) in practical applications is problematic as the sensor probe is subject to probe effects such as viscosity, thermal conductivity, impact and diabatic effects (Zvizdić, 2014). The measurement the probe produces is in fact an equilibrium measurement which deviates from the measurement an ideal environment. A dynamic correction factor, *K*, is therefore applied to account for these effects as seen in Equation (18) (Benedict, 1984).

$$T_t = T_s + K\,T_d = T_s + K\frac{c^2}{2c_p} \tag{18}$$

Type K thermocouples with fully shielded stainless steel probes are used to measure the temperatures. A dynamic correction factor of 0.9 is used for this setup, as convective effects dominate the flows (Benedict, 1984) (Childs, 2001).

3.1.2. Pressure

As with temperature the total or stagnation pressure is the sum of static and dynamic pressures. The static pressure is measured at the wall of the conduit through a small hole. Care must be taken to ensure there are no burrs left from the drilling lest these protrusions induce dynamic effects which will cause measurement errors. The total pressure is measured by a probe inserted into the flow with the hole facing into the flow, allowing the probe to measure the full pressure of the flow along that streamline (Hall, 2015). This is not always practical; therefore, the dynamic pressure can be accounted for with Equation (19) (Nguyen-Schäfer, 2015).

$$p_t = p_s + p_d = p_s\left[1 + \frac{(\kappa-1)Ma^2}{2}\right]^{\frac{\kappa}{\kappa-1}} \tag{19}$$

Pressure transmitters are the most common sensors utilised in most industrial environments, to measure pressure, as they are nearly immune to electrical

interference. Another advantage to a current based signal is that it can be transmitted over longer distances without a degradation in signal. This aspect makes pressure transmitters particularly suitable for the test cell environment as there are many potential sources of electrical interference.

Pressure transmitters from Huba Control and WIKA are used for the steady state acquisition of the exhaust gas recirculation and turbocharger pressures. Differential pressures are measured by Endress+Hauser pressure transmitters. Appendix D shows the manufacturer specifications (WIKA, 2016) (Huba, 2013) (Endress+Hauser, 2016).

3.1.3. Fuel consumption rate

A common metric to analyse the performance of an engine with regards to its power output and fuel consumption, is the brake specific fuel consumption (BSFC). Equation (20) (Heywood, 1988) shows the calculation for brake specific fuel consumption, with $q_{m,\,fuel}$ the mass flow rate of the fuel and, P_B, the brake power derived from the dynamometer speed and torque measurements.

$$BSFC = \frac{q_{m,fuel}}{P_B} \tag{20}$$

The fuel flow is measured by an AVL 730 dynamic fuel balance meter. This instrument is a gravimetric fuel consumption meter. It interfaces with the engine control software detailed in section 4.2. Specifications are outlined in Appendix D.

3.1.4. Emissions

Various methods are applied to measure the emissions profile of an engine. For each constituent component of diesel exhaust a different principle of measurement is applied. The emissions analysers used for this project are described below.

The soot density is measured by an AVL 415 smoke meter. The sampling probe is positioned post catalytic converter with the sampling line relayed to the control room where the unit is situated. A sample volume is drawn through the line by the instrument onto the filter paper. A reflectometer measures the “blackness” level and correlates it to the *Filter Smoke Number* (FSN). The unit is operated manually, with measurements recorded to a test sheet.

The sampling line for the Dräger MSI 150 and Ultra tune exhaust gas analysers is positioned as a separate line pre-catalytic converter. This line passes through a ceramic wool filter, a particulate filter and finally a refrigerated condenser unit before the sample volume is measured by the exhaust gas analysers. This is done to protect the measurement instrumentation and condition the sample volume. The Ultra tune analyser uses an infrared spectrometer to measure the carbon monoxide,

carbon dioxide and hydrocarbon levels. The oxygen is measured using a chemical sensor module.

The Dräger utilises an electrochemical sensor to detect carbon monoxide, nitrogen monoxide and nitrogen dioxide species. The calibration of the emissions instrumentation was checked before use. See Appendix D for equipment and layout specifications (AVL, 1998) (Dräger, 2011) (Ultra tune, 2010).

3.2. The exhaust gas recirculation system

As of 2015, the capability of quantifying the amount of exhaust gas recirculated through the engine was limited to information obtained from the engine control unit via VCDS. The only parameter indicative of the exhaust gas recirculation at any given operating point is the specified mass air flow at the inlet, which is measured by a hot wire anemometer sensor. This specified quantity stipulates how much atmospheric air forms part of the total intake charge, thereby indirectly stating how much exhaust gas must be recirculated per stroke of the engine.

Figure 18, shows a typical mass air flow (MAF) map obtained from data off an OEM engine control unit. This map is used by the engine control unit to control the amount of exhaust gas being recirculated to the intake manifold. The amount of charge exhaust gas is regulated by adjusting the poppet valve allowing a specified quantity of exhaust gas to replace a fraction of the atmospheric charge air to form the total intake charge. (Jääskeläinen, 2016).

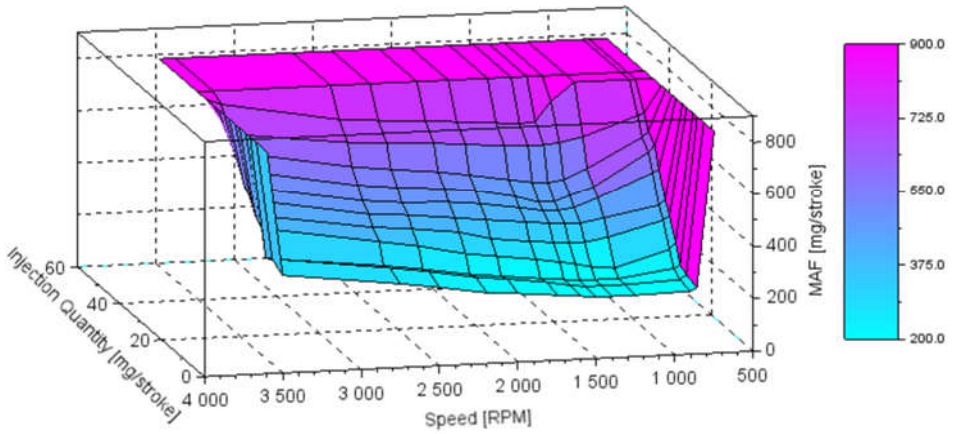

Figure 18: Typical OEM MAF map for a turbocharged diesel engine

The actuation of the poppet valve is measured by characterising the vacuum pressure of the actuator with the percentage lift of the valve. This is done to aid in detecting when the exhaust gas recirculation is deactivated by the engine control

unit. The output of the measurement was verified by the exhaust gas recirculation duty cycle obtained from VCDS.

The need to measure the exhaust gas recirculation more directly in real-time rather than simply referring to the specified mass air flow quantity is desired. The most common method of defining the exhaust gas recirculation is determining the exhaust gas recirculation rate, mentioned in section 2.2.2. It was decided early on to restrict the measuring of the exhaust gas recirculation rate to mass flow methods. Continuously measuring carbon dioxide concentrations requires very sophisticated equipment, which the facility does not house at present.

The individual mass flows of the atmospheric and exhaust gas recirculation must therefore be measured. The following sections detail the design methodology followed in selecting appropriate measuring devices.

3.2.1. Recirculated exhaust flow rate

Literature suggests various methods of determining mass flow rate of the recirculated exhaust gas. The general trend suggests an exponential increase in complexity and cost of the measuring system, the higher the degree of accuracy required and the lower impact to the normal operation of the engine, as seen in Table 4, adapted from Laurantzon (2010).

Table 4: Mass flow measurement methods (Laurantzon, 2010)

Measuring device	Pressure loss	Range	Accuracy
Orifice plate	High	3:1	2.4 % FS
Nozzle meter	Medium	3:1	2 % FS
Venturi tube	Low	3:1	1 % FS
Laminar flow meter	High	10:1	1 % Range
Pitot tube	Very Low	3:1	5 % FS

The different layout options for the exhaust gas recirculation system as discussed in section 2.2.2, was considered. Too keep the current setup as simple and robust as possible, as little as possible custom alterations were made.

The venturi tube is chosen as the preferred method since it has the lowest pressure loss of all the non-invasive flow meters and the best accuracy. The application of venturi tubes to measure the mass flow rate of recirculated exhaust gas in heavy duty trucks also factored into the decision to utilise this design (Jääskeläinen & Khair, 2012). Possible drawbacks include inaccuracies at low flow speeds, possibly due to momentary flow reversal from the pulsations produced from the engine exhaust, as noted by Laurantzon (2010).

The ISO 5167 standard for differential pressure measurement devices was used as a guideline, bearing in mind that some of the design criteria set in the standard cannot be adhered to due to size constraints (ISO 5167-4, 2003). The compact design of the venturi tube allows for the close mounting of the device to the engine as shown in Figure 19. A bracket was manufactured to support the weight of the venturi tube, relieving any stress it put on the mounting points on the exhaust manifold.

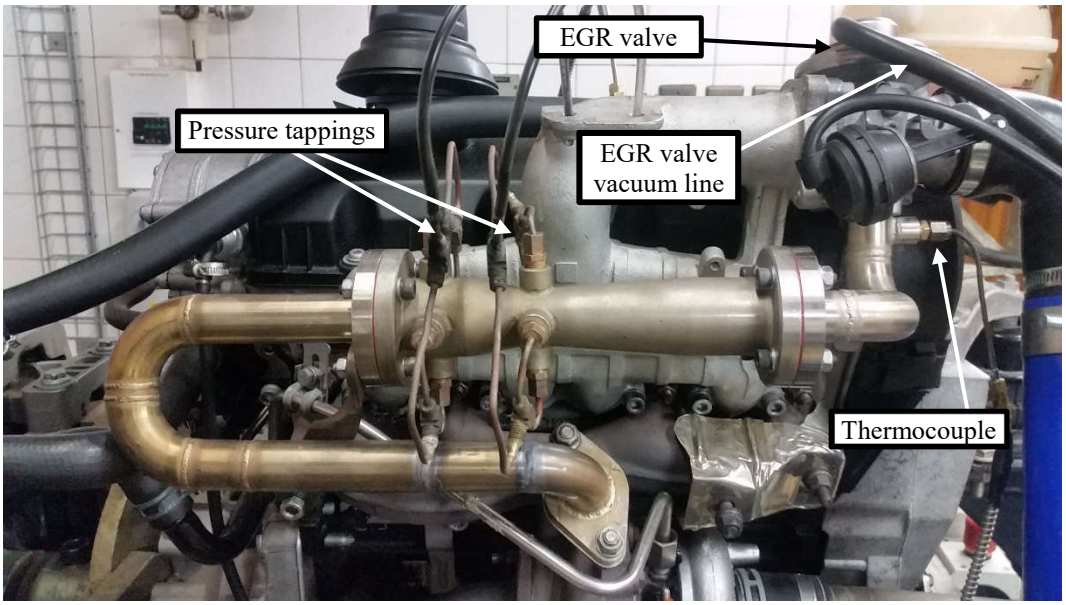

Figure 19: Recirculated exhaust gas flow measurement setup

Temperature and pressure measurements on the system are used to determine the approximate density of the exhaust gas, as well as the mass flow rate. The poppet valve lift is measured by monitoring the vacuum in the line. The intake manifold and exhaust gas recirculation poppet valve were cleaned to prevent the valve operation from being impaired due to excessive fouling. Calibration of the manufactured venturi tube was performed to obtain its characteristic volumetric flow curve. The calibration process is described in Appendix C.4.

3.2.2. Atmospheric air intake flow rate

The determination of the exhaust gas recirculation rate requires not only the mass flow rate of the recirculated exhaust gas, but also the mass flow of the atmospheric air charge. The Meriam laminar flow meter used by Blom (2015) to verify the mass air flow readout from VCDS, is used in this case to assist with the determination of the air mass flow rate. Calibration was performed on the laminar flow meter to verify that the calibration equation used by Blom (2015) is still valid. The calibration is further detailed in Appendix C.5. Figure 20 shows the measurement setup for the atmospheric air intake.

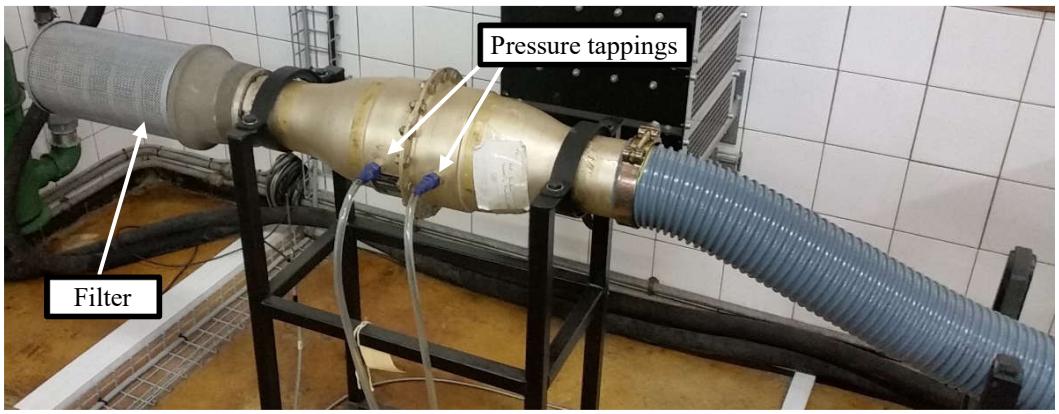

Figure 20: Atmospheric air intake flow measurement setup

3.3. The variable geometry turbocharger

The motivation behind the instrumentation of the variable geometry turbocharger stems from the need to obtain direct measurements of the operating conditions pre-and-post for both the turbine and compressor. As of 2015, the measurement capabilities on the engine test bench only measured boost pressure and charge temperature via the manifold air pressure sensor on the variable geometry turbocharger.

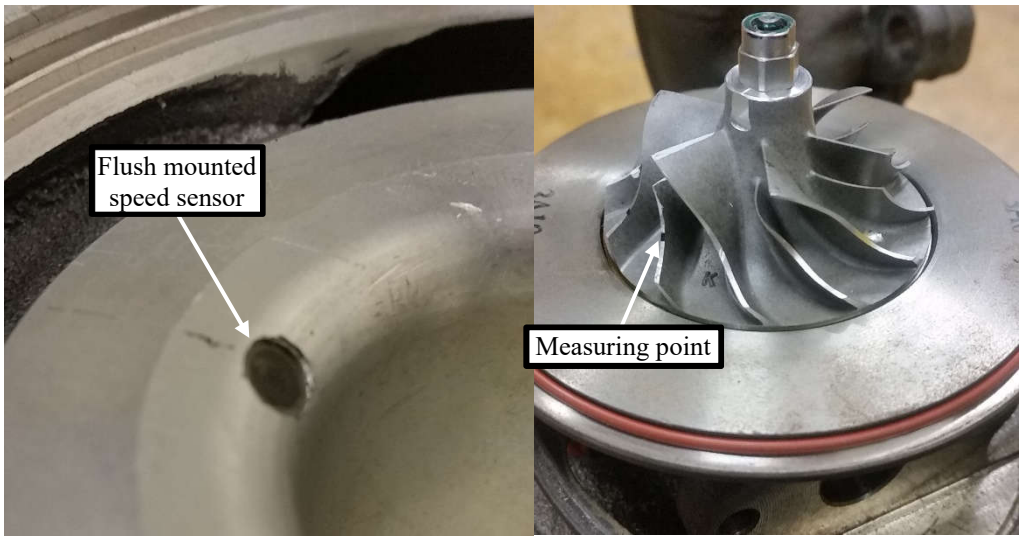

Figure 21: Compressor speed sensor installation

The work done by Romagnoli & Martinez-Botas (2012) was used as a framework to establish the sensor layout for the turbocharger. The instrumenting of the turbocharger necessitated the dismantling the turbocharger currently installed on the TDI engine. The positioning of the compressor wheel speed sensor is critical in obtaining a reliable speed reading. The sensor is therefore positioned according to

the manufacturer specifications (ACAM, 2015). Care was taken to position the sensor at a 45° angle to the axis of rotation, with a 1 *mm* clearance between the shroud edge of the compressor wheel and the sensor shown by the flush mounting of the sensor head with the diffuser wall in Figure 21.

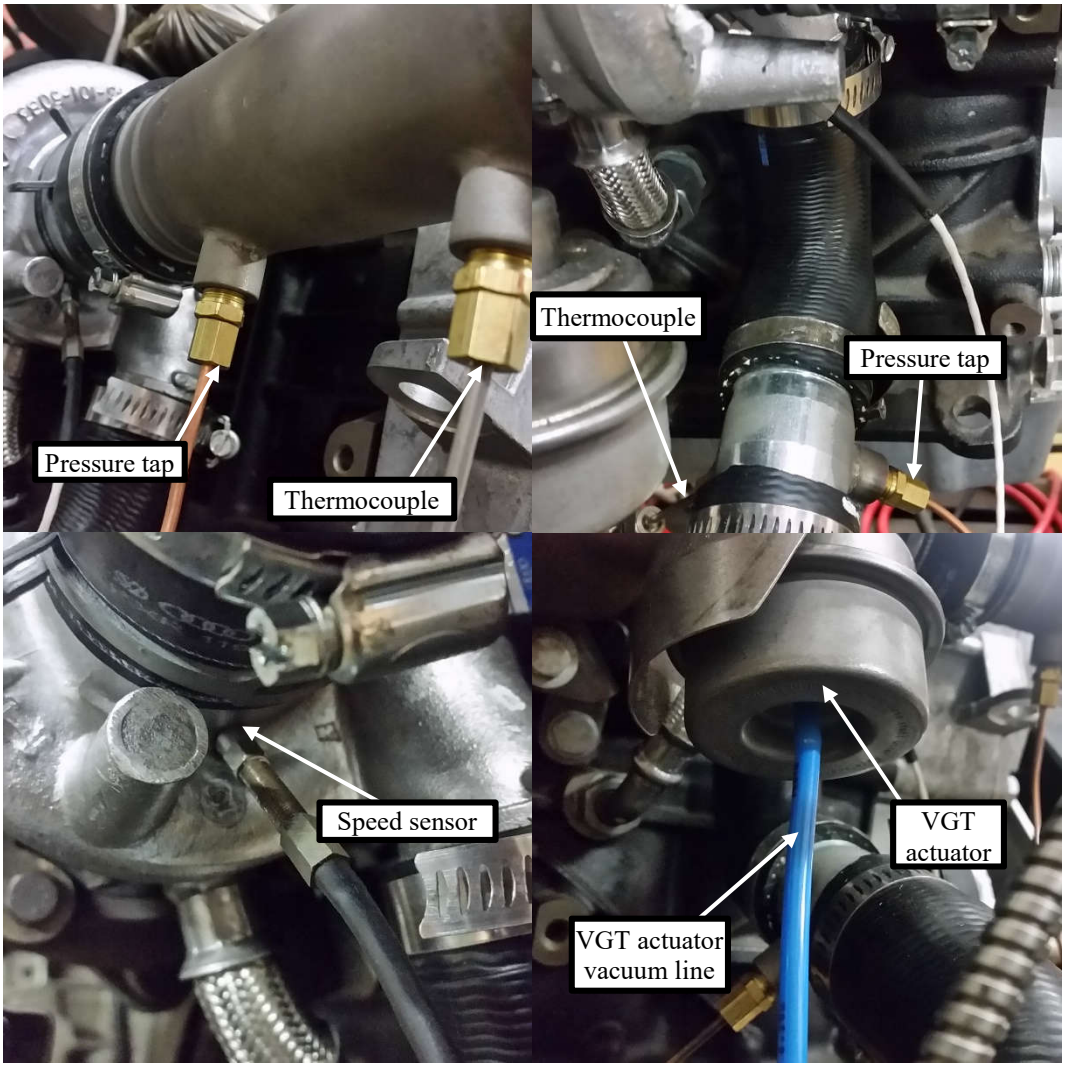

Figure 22: Sensor positions on variable geometry turbocharger

A PICOTURN© rotational speed sensor and digital signal processing unit is used to measure the rotational speed of the aluminium compressor wheel of the turbocharger. This sensor uses an L-R circuit as mentioned in section 2.2.3. Refer to Appendix D for the manufacturer specifications of the rotational speed sensor (ACAM, 2015).

Figure 22, shows the sensor locations installed to the turbocharger. The positioning of the pressure and temperature sensors ensures that the normal operation of the

turbocharger is impacted minimally due to the insertion of probes into the air paths of both the intake and exhaust air. To that end, the sensors are mounted on separate straight pipe lengths, upstream and downstream of the compressor. The actuation of the variable vanes is measured similarly to the actuation of the poppet valve, described earlier in section 3.2.1.

3.4. Development of the LabVIEW graphical user interface

One of the key areas Blom (2015) recommended be improved upon, is the LabVIEW data acquisition program. The instrumentation and sensor setup used to measure the in-cylinder pressure, consisted of the Optrand PSIglow-A pressure transducer and a Kübler Sendix 5020 incremental shaft encoder. These sensors were coupled to a National Instruments X-Series USB 6351 data acquisition device. The advantage to this setup is that in-cylinder pressure can be captured according to the crank angle of the engine by allowing the data acquisition device to use the shaft encoder's signal as an external clock. Top dead centre of the cylinder can be pegged by synchronizing the encoder's zero position, i.e. the Z index signal, with that of the piston.

The expanded LabVIEW measurement program builds upon previous work. The suitability of the in-cylinder pressure transducer and the shaft encoder to the measurement setup is not discussed in this thesis as the motivation for the use of these sensors has already been discussed by Blom (2015). The additional sensors and instrumentation used in this study are however discussed in the following sections.

3.4.1. Performance characteristics of sensors and instrumentation

The test bench setup primarily deals with steady state acquisition of data. The static performance characteristics of the sensors and instrumentation is therefore important. The characteristics include the sensitivity, zero offset, non-linearity, hysteresis, noise and resolution of the measuring equipment.

Sensitivity of sensors often follow a linear trend between the measured parameter and output signal the sensor generates, as seen in Figure 23(a). This sensitivity is constant over the entire measurement range unless the sensor develops a variable sensitivity over its measuring range, commonly referred to as non-linearity, seen in Figure 23(c).

Zero offset is simply a deviation from the referenced output signal, stipulated by the manufacturer, seen in Figure 23(b). Hysteresis is defined as the discrepancy between ascending and descending output values for the same measurement value over the measuring range, seen in Figure 23(d) (NASA, 2010).

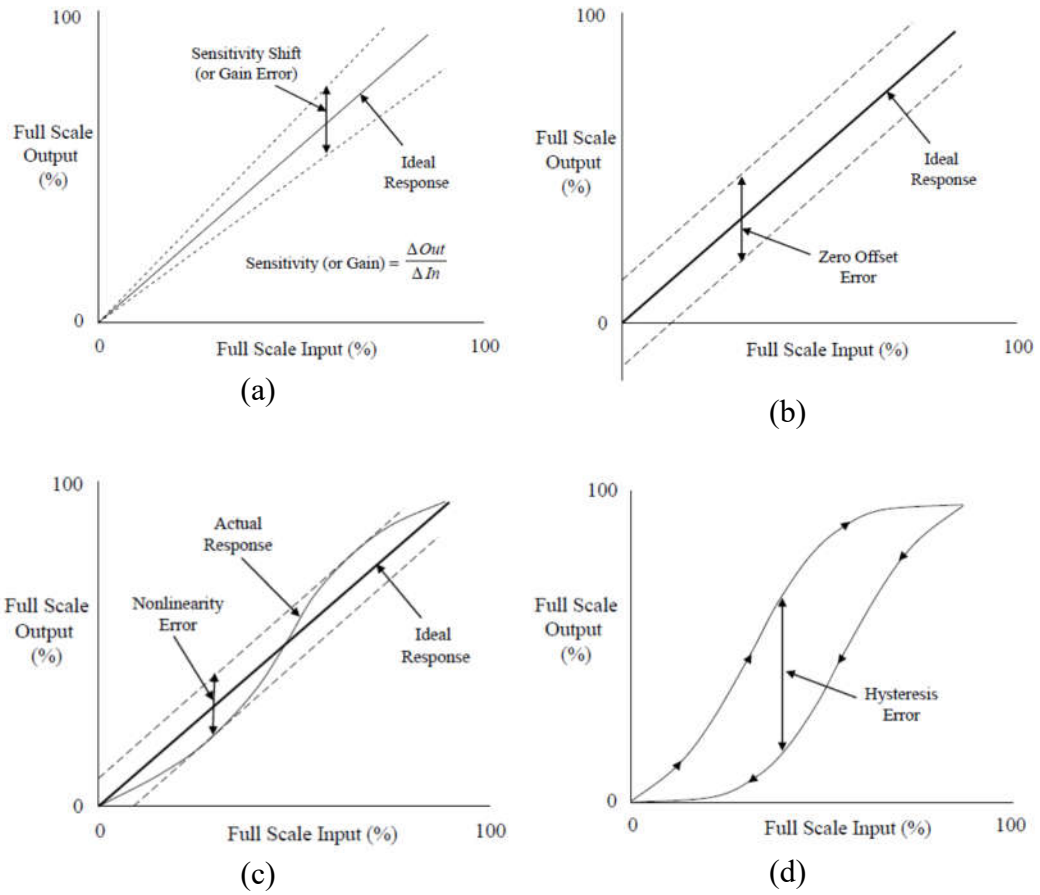

Figure 23: Static performance characteristics of measuring equipment (NASA, 2010)

The resolution of an instrument is a result of the device's sensitivity to registering a change in a continuously varying signal and outputting the observed change in a series of discrete outputs to approximate the input. This characteristic is closely related to noise also known as electrical interference, since an instrument with sufficiently high resolution will register the noise on a signal much more precisely than an instrument with a poor resolution.

These performance characteristics are vital, therefore calibration is performed on each sensor with the same instrumentation that is used during the experiments. The calibration serves to eliminate the errors associated with sensitivity and the zero offset as these characteristics can be compensated for in software. Calibration furthermore establishes the severity of the remaining static characteristics, since it is difficult to compensate for these characteristics without individually characterising the sensors. See Appendix C for further details on the calibration.

Certain dynamic performance characteristics are also important. The response time of the sensors and the stability of the sensor and instruments are of concern when testing on an engine which, due its nature of operation, produces pulsations in the

intake and exhaust flows. Even at steady state operating conditions, the engine control unit is still constantly controlling the engine via the various actuating components, such as the exhaust gas recirculation poppet valve and the variable vane actuator.

For the sensors to be able to register sudden changes in control output, the dynamic response time, i.e. the ability of a sensor to respond quickly to a change in input, must be as low as possible. Often this is where the consideration of performance versus cost comes into play. The stability of measuring equipment refers to its potential to retain its specified performance characteristics without need for calibration. Priority was therefore given to sensors with appropriate dynamic response times and long-term stability. See Appendix D for sensor specifications.

3.4.2. Instrumentation specification

With the above characteristics in mind, the selection of not only suitable sensors but instrumentation is important in ensuring the most accurate measurement setup possible. The selection of sensors has been discussed in section 3.1. The following section describes the instrumentation, i.e. the data acquisition devices selected.

The National Instruments USB-6351 features multiple analogue voltage inputs and outputs as well as digital inputs and outputs. The analogue inputs can be configured in a variety of ways depending upon the application. For the pressure transmitters, the analogue inputs are configured as referenced single ended (RSE) connections, allowing for optimal use of the number of inputs. Per manufacturer recommendations, to alleviate the effect of electrical interference, the differential pressure sensors, speed sensor and in-cylinder pressure sensor are configured as differential analogue inputs, since these inputs transmit voltage instead of current and are prone to electrical interference. Table 5 shows the relevant manufacturer specifications (National Instruments, 2015).

Table 5: X-Series USB-6351 specifications (National Instruments, 2015)

Maximum multiple channel sample rate	1,00 MS/s
Number of analogue input channels	8 differential/16 single ended
Analog-to-Digital Conversion	16 bits
Response Time	1 µs

During previous testing a marked degree of electrical interference was noticed on the temperature measurements. This phenomenon was random and difficult to diagnose. It was decided that a separate temperature logger be introduced to measure the additional temperature measurements.

The second data acquisition device is dedicated to high precision temperature measurements. A National Instruments USB-4350 is chosen to acquire the temperature measurements. This device is outfitted with an analogue-to-digital converter with built-in noise rejection to deal with the random electrical interference. It also features cold junction compensation which the USB-6351 does not. Table 6 shows the relevant manufacturer specifications (National Instruments, 2005).

Table 6: USB-4350 specifications (National Instruments, 2005)

Maximum multiple channel sample rate	1.1 S/s
Number of analogue input channels	16
Error	0,69 °C

3.4.3. Data acquisition program development

The primary objectives for the LabVIEW data acquisition program, is to make full use of the instrumentation available. To this end the in-cylinder pressure measurement and exhaust gas recirculation system with turbocharger measurements are combined to utilise the same data acquisition device.

Some restrictions imposed by the instrumentation includes, different maximum sampling rates between the instrumentation devices. Driver software of the two instruments are incompatible making it difficult to synchronize the clocks between the devices. Each device only has one timing engine, making it impossible to sample at multiple sampling rates at the same instance.

Two separate programs are implemented to capture the exhaust gas recirculation and turbocharger measurements as well as the in-cylinder measurements respectively. This allows the user to switch between acquiring the in-cylinder pressure traces or the exhaust gas recirculation and turbocharger measurement data. It also serves to avoid an overload of information on any one of the front panels.

Figure 24 shows the design of the graphical user interface (GUI). Each measurement location is represented by an analogue indictor comprising a pressure gauge and thermometer. Histogram charts for pressure and temperature allows for the detection of irregular measurements and to aid in determining when steady state operating conditions have been established at any desired operating point.

Speed indicators are displayed in the centre of the GUI. The actuation of the poppet valve and variable vanes are represented by two indicators below the speed gauges. A tab control on the bottom right contains the settings and preferences for sample time and calibration.

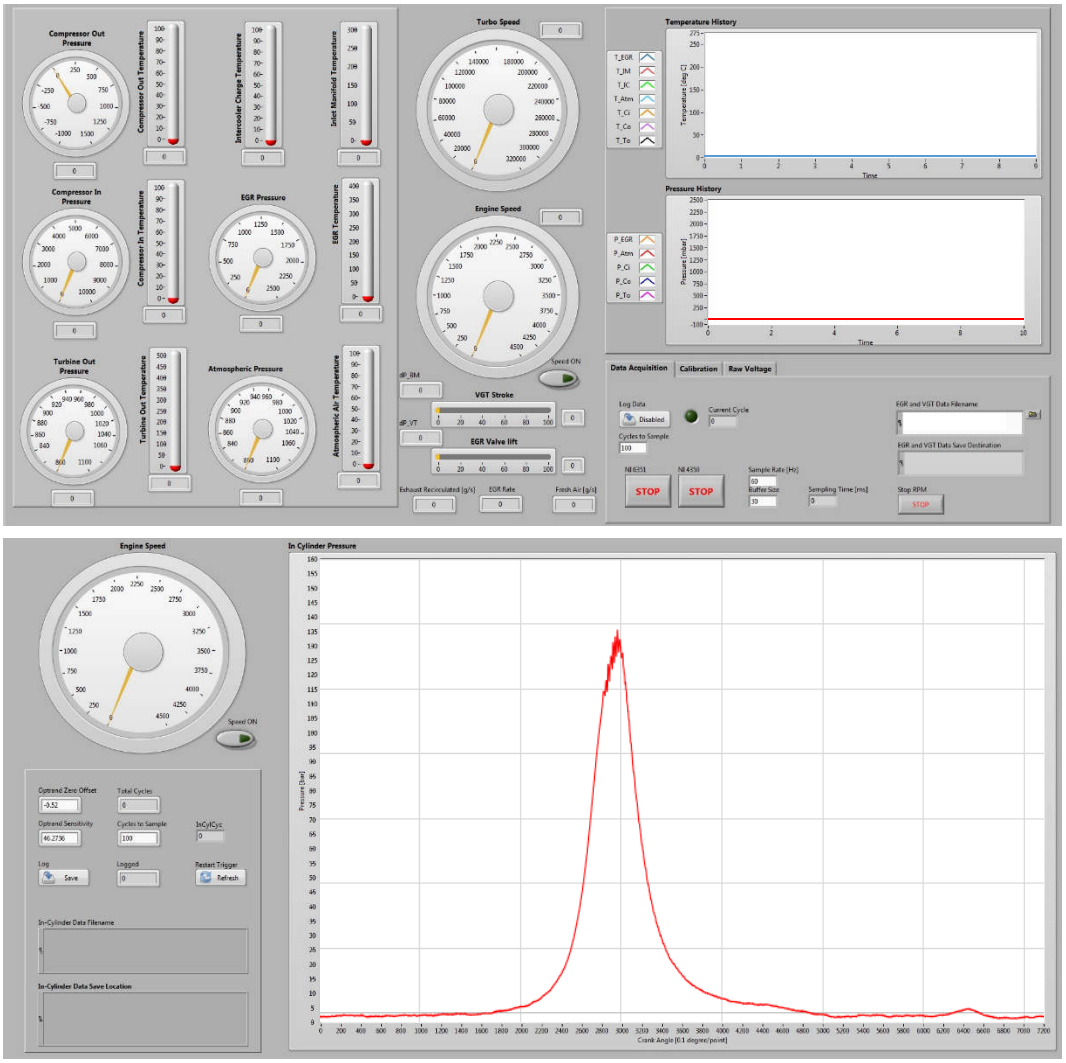

Figure 24: LabVIEW data acquisition front panels

The wiring of the sensors inside the test cell to the instrumentation inside the control room is accomplished by using the shortest length of cabling possible, with proper shielding and grounding practices. As most of the pressure measurements are accomplished using pressure transmitters, the risk of electrical interference is kept to a minimum.

The pressure transmitters are driven by a 24 V_{DC} excitation voltage. The current output is converted to an analogue voltage output by inserting a high quality, 500 Ω resistor between the analogue input and ground terminals of the NI 6351 device, converting the 4-20 mA signal to a 2 to10 V signal. The differential Endress+Hauser pressure transmitters have custom circuitry supplying 24 V_{DC} excitation transformed from a 220 V_{AC} input. The circuitry also converts the current output of the device to voltage.

3.5. Summary

In addition to the upgrades recommended by Blom (2015), discussed in Appendix A, the test bench was fitted with a venturi tube to measure the recirculated exhaust flow rate. The laminar flow meter used previously to validate the VCDS mass air flow measurements was incorporated to the test bench to allow the acquisition of both the recirculated exhaust and the fresh intake air. This enables the determination of the exhaust gas recirculation rate in real-time via the new data acquisition program discussed in section 3.4. The variable geometry turbocharger in its capacity to support the exhaust gas recirculation is also instrumented. Figure 25 shows the upgraded test bench.

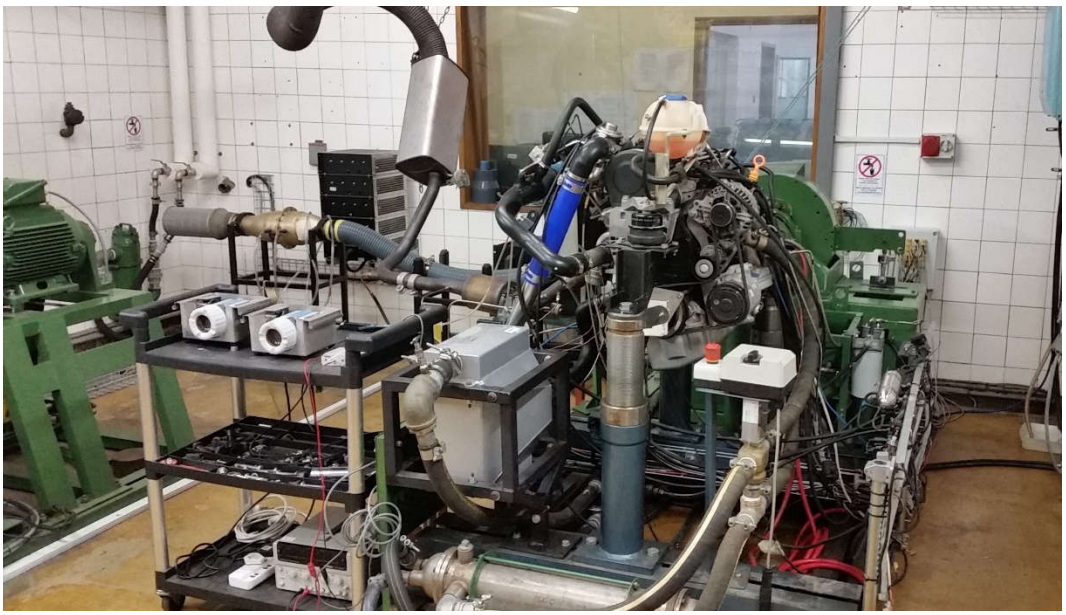

Figure 25: Upgraded test bench

4. EXPERIMENTAL DESIGN

The experimental design focusses on the influence of the exhaust gas recirculation system on the engine performance with regards to exhaust gas emissions and fuel consumption when running the engine on different fuels. As most exhaust gas recirculation strategies are deployed in the engine's typical operating range of 1600 *RPM* to 3000 *RPM*, the test protocol centres largely in this range (Heywood, 1988) (Abd-Alla, 2002). The role of turbocharging is investigated in its capacity to support the exhaust gas recirculation system.

4.1. Experimental protocol

The experimental testing follows a bracket-based protocol. Each test fuel is preceded by the synthetic 50 *ppm* ultra-low sulphur diesel (ULSD) bracket fuel. All experimental test points are performed in sequence from the lowest to highest load for the three speed set points. At the end of the twenty-four test points, the first test point of 1800 *RPM* at 20 *N.m* is repeated. This method of testing serves to establish repeatability to ensure reproducible results. Figure 26 represents the test points within the operating range of the engine. Before a test commences, all measurements are recorded without the engine running. All tests are performed at steady-state conditions.

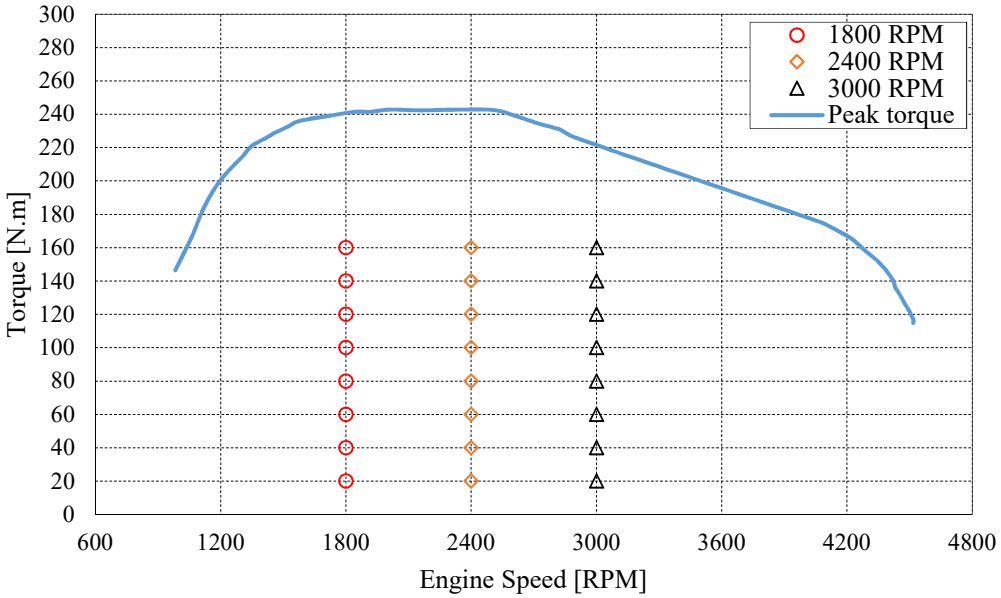

Figure 26: Experimental test points for batch testing of fuels

The synthetic 50 *ppm* ULSD, mentioned above, is used to establish repeatability of engine performance. This fuel also serves to detect and diagnose any irregularities in engine operation and which could impact on engine performance.

Crude derived 50 *ppm*, ULSD is used as the base fuel for blending during the experimental protocol. It also serves as the test fuel at the end of the experimental procedure. This fuel does not alter the engine performance or emissions significantly from the synthetic ULSD. Figure 27 illustrates the experimental procedure.

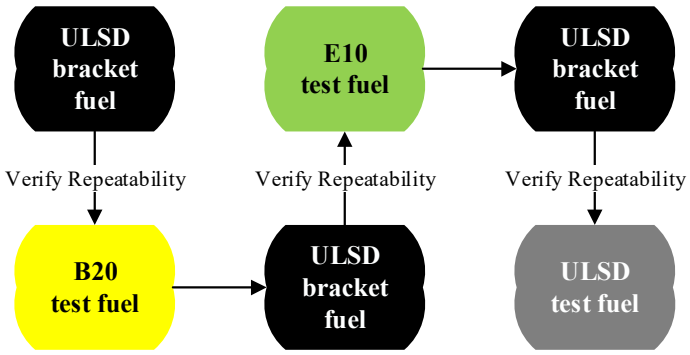

Figure 27: Experimental procedure

The blends are made using local, commercially available, biodiesel and ethanol. Table 7 disassembles the fuel blends into their constituent fuel percentages. The crude derived ULSD is also tested at the end of the procedure as seen in Figure 27.

Table 7: Fuel blend composition

	Volume percentage [%]		
Fuel blend designation	**Crude derived ULSD**	**Biodiesel**	**Ethanol**
B20	80	20	0
E10	90	0	10

The operating conditions for the experimental procedure is maintained for all the test points recorded. Table 8 shows the operating conditions. The full load performance of the engine was checked by Blom (2015) after completing his test programme with the engine performance within OEM specification. Before testing commenced, the peak torque performance was rechecked and found to be within the OEM specification.

Table 8: Operating conditions for experimental testing

Operating conditions	**Maximum allowable/set point temperature**
Engine oil temperature	100 °C
Engine coolant temperature	92 °C
Fuel inlet temperature	25 °C
Post-intercooler temperature	35 °C

4.2. Control of experimental equipment

The control of the engine is accomplished by the Engine Test Automation (ETA) software. This program interfaces with the Allen Bradley MicroLogix 1200 programmable logic controller (PLC). The PLC is connected to the dynamometer controller, load cell amplifier, and fuel consumption meter. The program measures and calculates parameters such as the speed, torque, power, brake specific fuel consumption, oil pressure and various operating temperatures on the engine. According to SAE J1349 (2008), the power for a boost-controlled diesel engine does not need to be corrected for barometric pressure.

The program is configured to run in two modes. For the speed control mode, the user has control over the throttle position and speed set point. The Schenck LSW 24/18 dynamometer controller is sent a speed set point via ETA. To ensure the engine does not exceed this set point, the controller applies a load as necessary. This mode is utilised for full load performance testing.

The second control mode is torque control. In this mode the user inputs the desired speed and torque set points. The programmable logic controller then adjusts the throttle position as necessary to maintain a stable operating point. This mode is used during partial load testing. As seen in Figure 26, all the test points are situated at partial load points. The experimental protocol was therefore performed using the torque control mode.

The VCDS program, mentioned in section 3.3, is a general diagnostic tool used to interrogate the different control modules on the engine control unit. It can be used to identify faults on the engine by consulting the error codes generated by the engine control unit, or by logging real-time data of several sensors and input control signals. The error codes on VCDS were checked to verify that the engine was operating as per OEM specification before any experiment commenced. Table 9 shows the engine specifications (VAG, 2003).

Table 9: Engine specifications (VAG, 2003)

Type	TDI, four-cylinder, in-line engine
Displacement	1896 cm^3
Stroke/Bore	79.5 mm/95.5 mm
Compression ratio	19 : 1
Peak torque	240 N.m @ 1800 RPM to 2400 RPM
Peak power	74 kW @ 4000 RPM
Emissions standard	Euro III
Engine management	Bosch EDC 15 P
Emission control	EGR and DOC
Firing sequence	1-3-4-2

4.3. Data acquisition and processing

The sampling of all data occurs at steady state operating conditions. The ETA, and LabVIEW graphical user interfaces are used to determine when the measurements have stabilized, before data logging commences for the specific operating point. Care is taken to ensure the operating conditions, stated in Table 8, are controlled and not exceeded to ensure confidence in the repeatability of the results.

With the exclusion of the in-cylinder measurements, all pressure measurements are sampled over a period of 20 seconds in LabVIEW, at a 60 *Hz* sample rate by the National Instruments USB-6351 data acquisition device. The temperature, to filter out any unwanted electrical interference, is sampled at 1 *Hz* by the National Instruments USB-4350 data acquisition device, also over the same period.

To obtain a good average of the brake specific fuel consumption, the measurements obtained from ETA are sampled over a period of 30 seconds after steady state operating conditions were obtained. The sample rate of the in-cylinder pressure measurements is dependent on the speed of the engine, and therefore to ensure consistency, 100 cycles are captured for 1800 *RPM* at 20 *N.m* and 160 *N.m* and for 3000 *RPM* at 20 *N.m* and 160 *N.m*.

To analyse the steady state data, the mean and standard deviation of each measurement in the sample data is taken. The population standard deviation is used to determine the deviation of each measurement at any specific operating point. This is done to identify any outlying data points which could adversely affect the steady state result. Any identified outliers are investigated to try and determine the source of the outlier data. Outliers identified as noise are disregarded.

5. ANALYSIS OF EXPERIMENTAL RESULTS

The primary objective of the experimental testing was to determine the influence exhaust gas recirculation has on the performance of the turbocharged diesel engine running on different biofuel blends. Exhaust gas constituents were also measured to determine the effect exhaust gas recirculation has on exhaust emissions. The focus therefore lies on the control of the exhaust gas recirculation poppet valve and the actuation of the variable vanes on the variable geometry turbocharger.

These two engine control inputs, and injection quantity, or throttle position, influence the operating conditions of the engine at a given load and engine speed. Whether the control of the poppet valve and the variable vanes are open or closed loop, is investigated in the following sections by considering the exhaust gas recirculation rate and the boost pressure at different operating points.

The hypothesis is that for an engine optimised to run on ULSD, any fuel blend with a lower calorific value, will require higher injection quantities to maintain the same operating point.

5.1. Exhaust gas recirculation rate

Throughout literature it has been proven that a higher exhaust gas recirculation rate is directly proportional to lower nitrogen oxides at any operating point (Abd-Alla, 2002). It is accepted practice that exhaust gas recirculation only be employed at low-to-mid range operating points as the application of exhaust gas recirculation at higher operating points yield diminishing returns in reducing nitrogen oxides and reduces maximum engine power (Stone, 1992) (Heywood, 1988). The poppet valve and variable vanes were not controlled manually on the present setup. The exhaust gas recirculation rate is controlled by the engine control unit.

The quantity of recirculated exhaust gas is determined by the opening and closing of the poppet valve. The boost pressure of the intake charge is regulated by controlling the position of the turbocharger variable vanes. The faster the compressor wheel spins, the more air is compressed leading to a greater mass air flow rate through to the intake manifold. It should be noted that the boost pressure is limited at each operating point as the boost pressure must never exceed the recirculated exhaust pressure whilst the poppet valve is still open.

Figure 28 through Figure 32, below, show the exhaust gas recirculation rate for the varying engine speeds of 1800 to 3000 *RPM*. As expected the exhaust gas recirculation rate decreases as the load on the engine increases for any given speed. For the crude oil derived ULSD, the decrease in exhaust gas recirculation rate is nearly linear for the lower load points between 20 *N.m* and 100 *N.m* at all the speed set points.

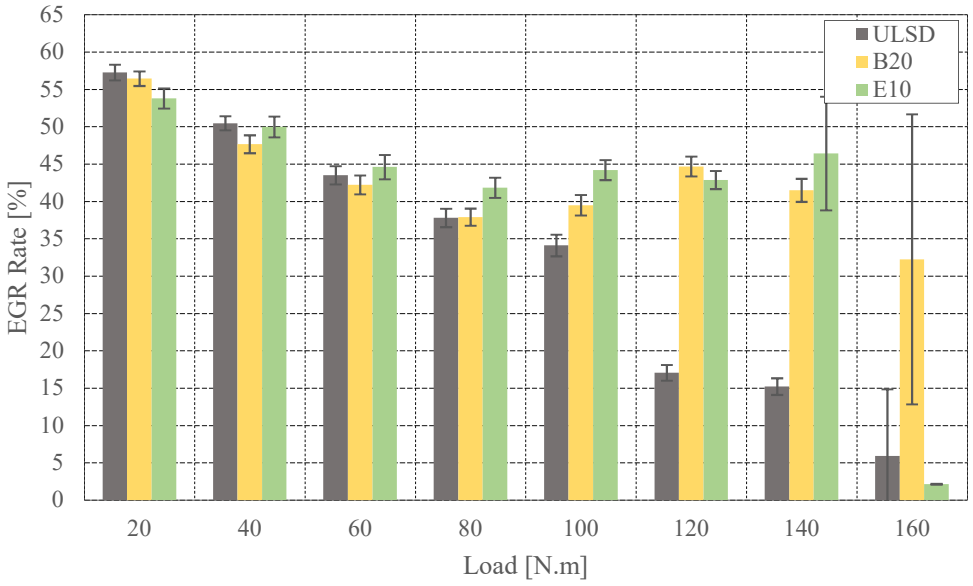

Figure 28: Exhaust gas recirculation rate at 1800 RPM

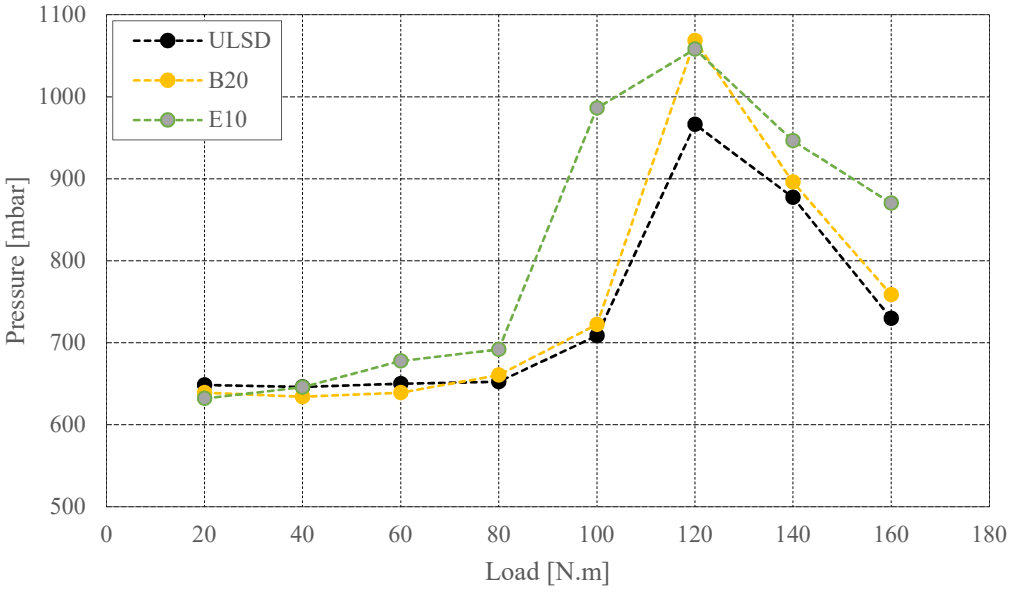

Figure 29: Differential pressure over poppet valve at 1800 RPM

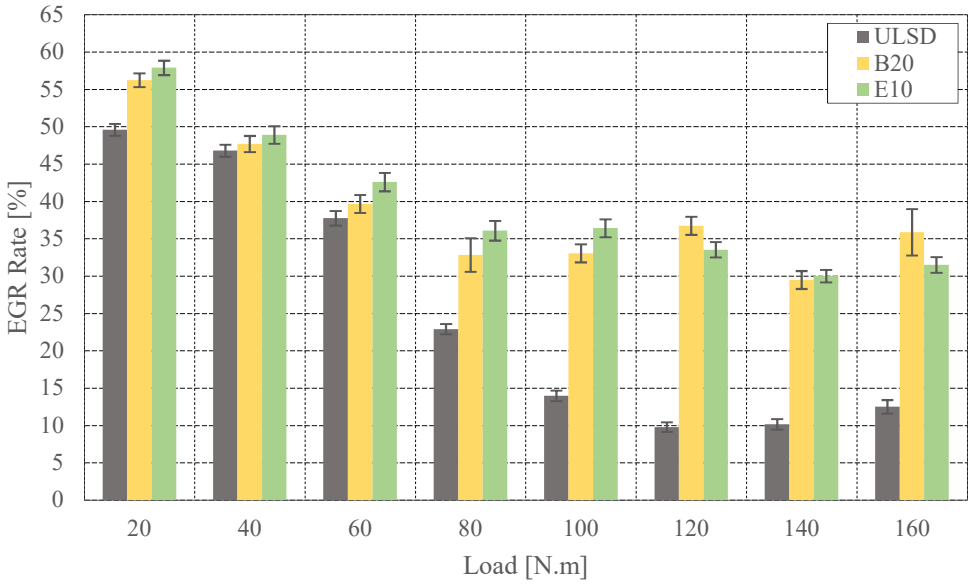

Figure 30: Exhaust gas recirculation rate at 2400 RPM

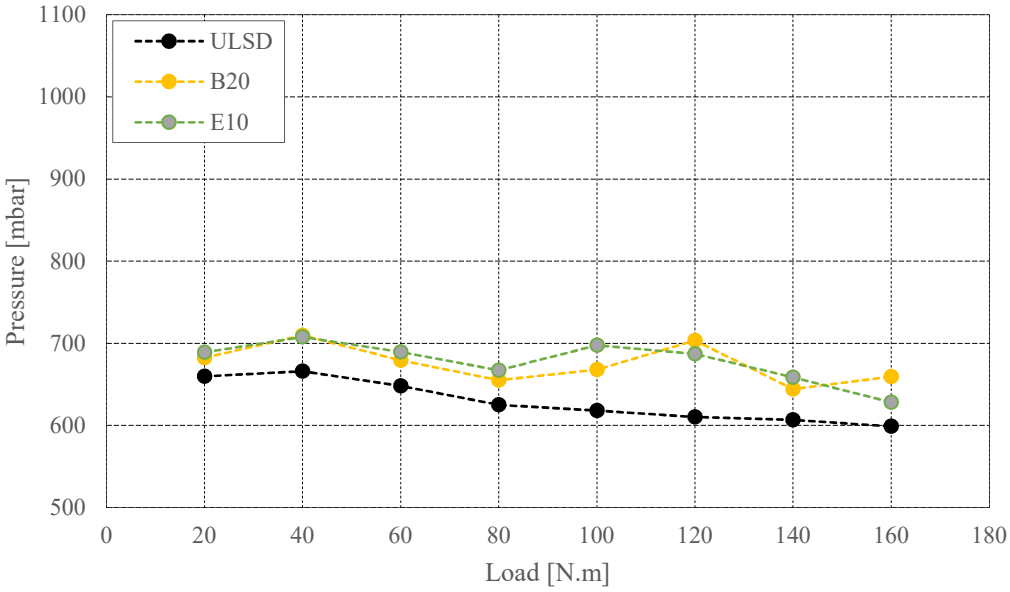

Figure 31: Differential pressure over poppet valve at 2400 RPM

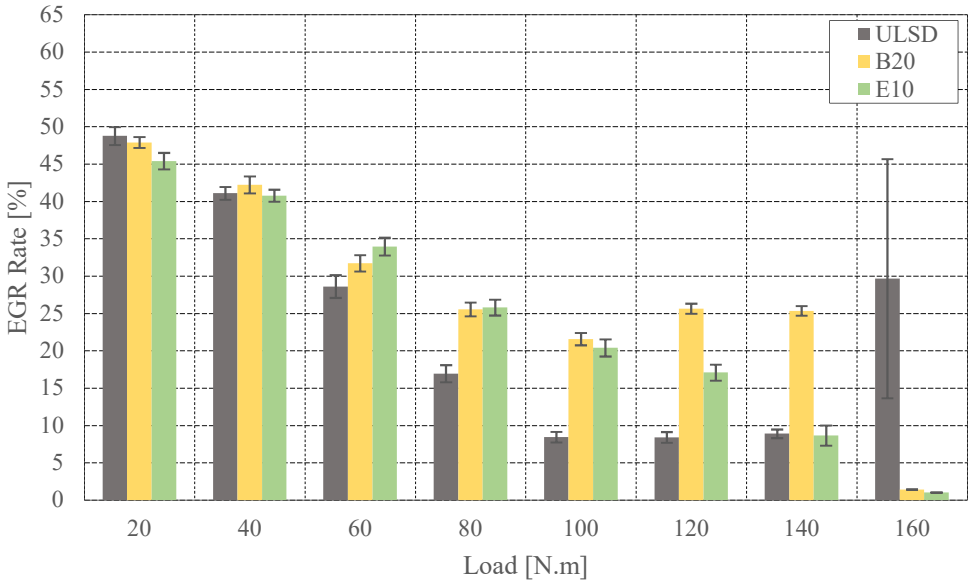

Figure 32: Exhaust gas recirculation rate at 3000 RPM

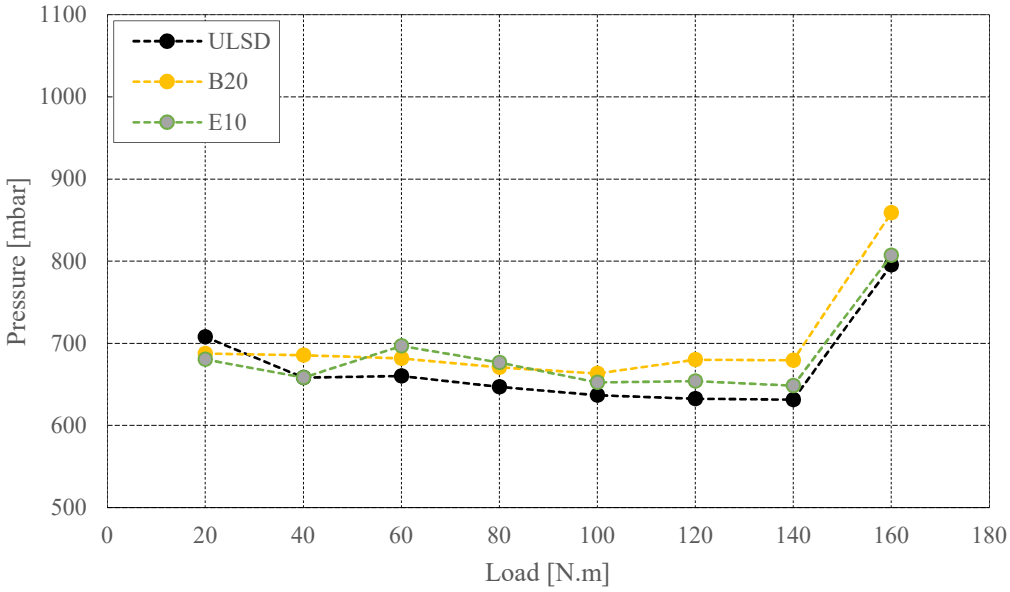

Figure 33: Differential pressure over poppet valve at 3000 RPM

Higher exhaust gas recirculation rate trends between 80 *N.m* and 160 *N.m* for the B20 and E10 blends versus that of ULSD are observed for all speed set points. The higher exhaust gas recirculation rate was found to result from a higher recirculated exhaust gas mass flow rate. The cause for the higher recirculated exhaust gas mass flow rates were investigated. It was determined that the pressures for the B20 and E10 blends in the exhaust gas recirculation route are higher than that of the ULSD fuel. This resulted in a higher differential pressure across the poppet valve leading to more of the atmospheric air intake charge mass being replaced by the recirculated exhaust gas charge. The phenomenon explained above is most clearly illustrated by comparing Figure 30 to Figure 31. Comparing the other speed set points yield similar results. When the poppet valve is closed the differential pressure can no longer drive recirculated exhaust to the intake manifold.

The high exhaust gas recirculation rate for the B20 blend at 1800 *RPM* at 160 *N.m* is due to the erratic opening and closing of the poppet valve, observed during testing and illustrated by the large standard deviation, over time, at that point. This phenomenon could be due to the operating point being in the part of the map where the exhaust gas recirculation transitions from being active to inactive. The control is dependent upon engine speed and throttle position, which are continuously adjusted by ETA to maintain a stable operating point. A similar observation was made for the ULSD at 3000 *RPM* at 160 *N.m* and the E10 blend at 1800 *RPM* @ 140 *N.m*.

For the 3000 *RPM* at 160 *N.m* set point, this effect is eliminated with the B20 and E10 fuel blends as the amount of injected fuel required to maintain the same load is increased, thereby shifting the operating point to another site on the engine control map. This enables the poppet valve to remain closed effectively eliminating any exhaust gas recirculation at these points. Exhaust gas recirculation rates for all operating points are consistent with literature (Ladommatos, et al., 1998) (Abd-Alla, 2002).The behaviour of the engine control unit with regards to the poppet valve suggest that the exhaust gas recirculation is accomplished via a closed loop control strategy (VAG, 2003) (Reif, 2014).

5.2. Exhaust gas emissions

The following section details the results obtained from the emissions analysers detailed by section 3.1.4. The exhaust gas constituents analysed include nitrogen oxides, soot, oxygen, carbon monoxide and carbon dioxide. The concentration of these constituents in relation to the exhaust gas recirculation rate and each other are discussed and compared to results obtained in literature.

5.2.1. Nitrogen oxides

The results obtained in this project as well as the results of Blom (2015), show the same growing trend in nitrogen oxides in the exhaust gas as the load increases. As with previous findings, as soon as the exhaust gas recirculation is deactivated, the

concentration of nitrogen oxides increases significantly negating the dilution effect as seen in Figure 34 and Figure 36. No significant improvement between the different fuels can be seen at any of the speed ranges with regards to nitrogen oxides emissions. It is the combustion process inside the cylinders that primarily drive the production of nitrogen oxides as substantiated by many sources in literature (Agarwal, et al., 2011) (Ladommatos, et al., 1998) (Ghadikolaei, 2016).

When comparing Figure 34 and Figure 36 the engine speed does have a noticeable effect of the production of primarily nitrogen monoxide as the increase in piston speed reduces the time for nitrogen monoxide formation. Comparing the 160 *N.m* operating points the nitrogen oxide levels are very similar at approximately 650 *ppm* with no exhaust gas recirculation active at this point.

The influence of turbocharging in conjunction with exhaust gas recirculation is apparent at the high load operating points. The increase in nitrogen oxides grow as the exhaust gas recirculation diminishes, and this change is especially apparent when the exhaust gas recirculation is switched off.

With only high compressed atmospheric air the formation of nitrogen oxides is enhanced by the thermal effect as well as the negation of the dilution effect (Ladommatos, et al., 1998).

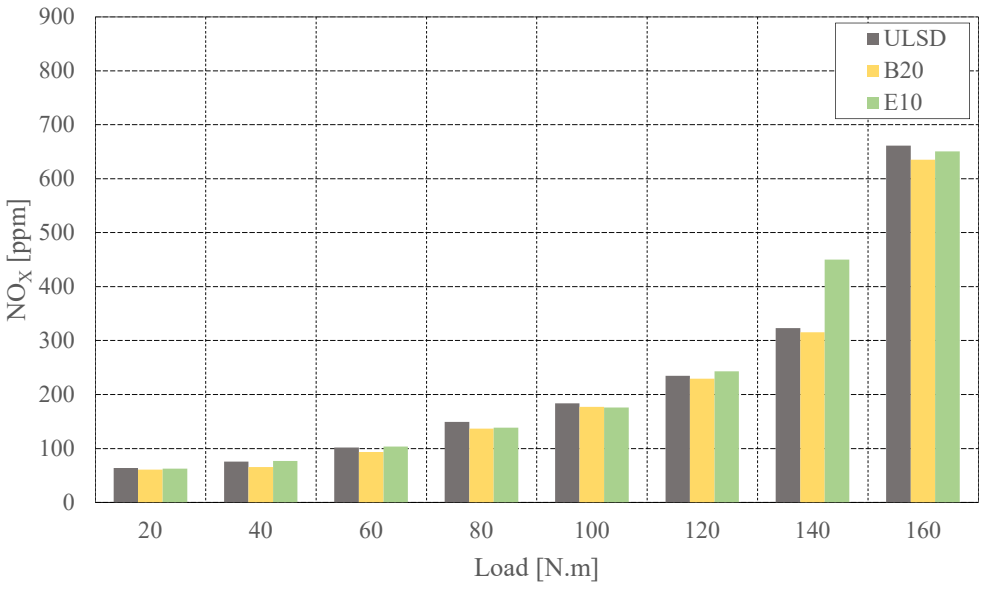

Figure 34: Nitrogen oxides concentration at 1800 RPM

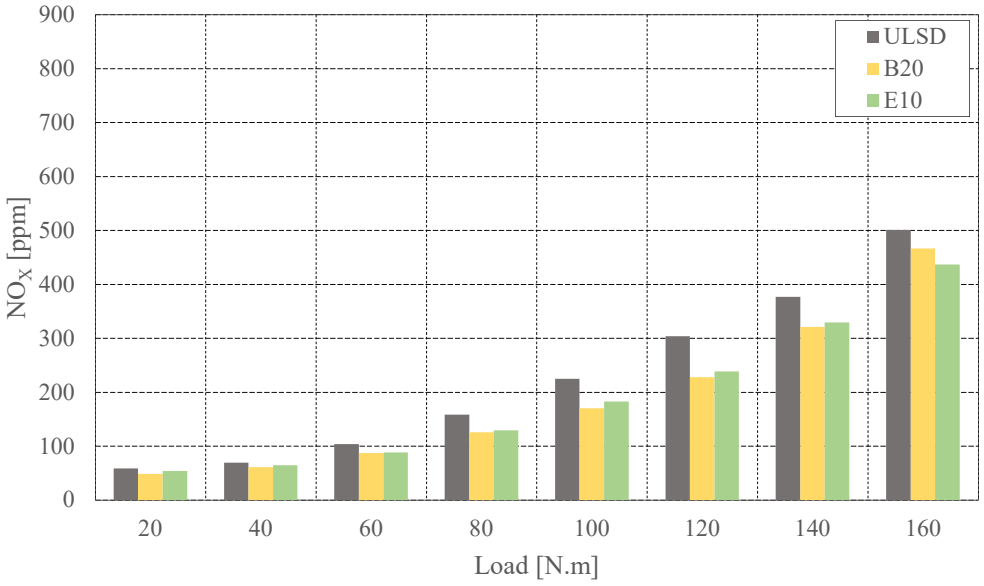

Figure 35: Nitrogen oxides concentration at 2400 RPM

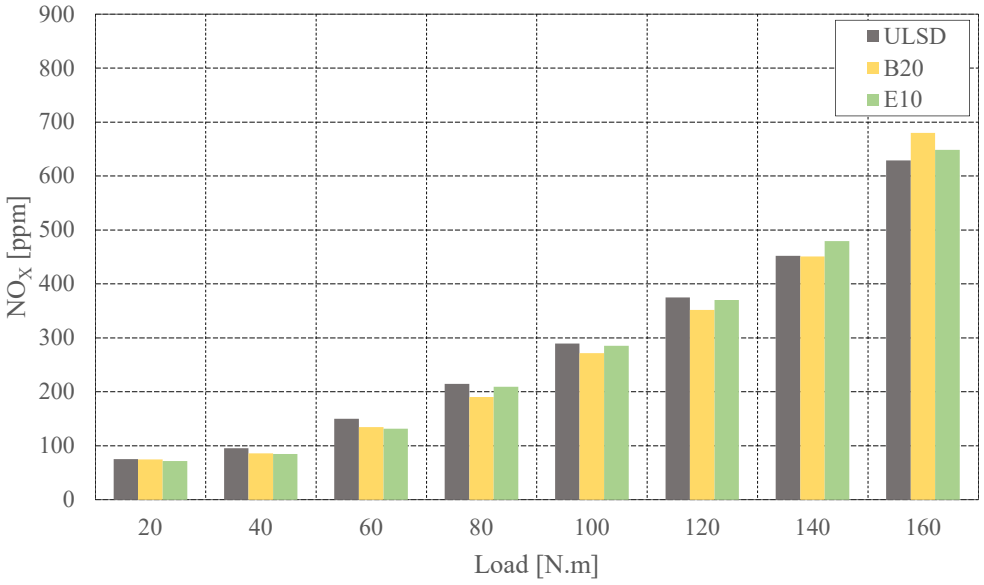

Figure 36: Nitrogen oxides concentration at 3000 RPM

5.2.2. Soot

In general ethanol addition to diesel shows a decrease in filter smoke number across the load range for 1800 *RPM*. This trend also holds true for the B20 blend when considering 1800 *RPM* as a slight reduction in filter smoke number versus the ULSD is observed when looking at Figure 37. This is consistent with literature which suggests a higher percentage in biodiesel corresponds to a lower filter smoke number (Abu-Hamdeh & Alnefaie, 2015) (Rashedul, et al., 2014).

The decrease in filter smoke number observed at the higher load points across the speed ranges, is due to improved combustion at higher temperatures resulting in higher nitrogen oxides at these points as seen in Figure 34 to Figure 36. This is substantiated in literature where an increase in nitrogen oxides production usually leads to a decrease in soot formation, as soot readily oxidizes in the presence of increased oxygen (Heywood, 1988) (Ladommatos, et al., 1998). The filter smoke numbers for the synthetic and crude derived 50 *ppm* diesel were compared and found to correlate well.

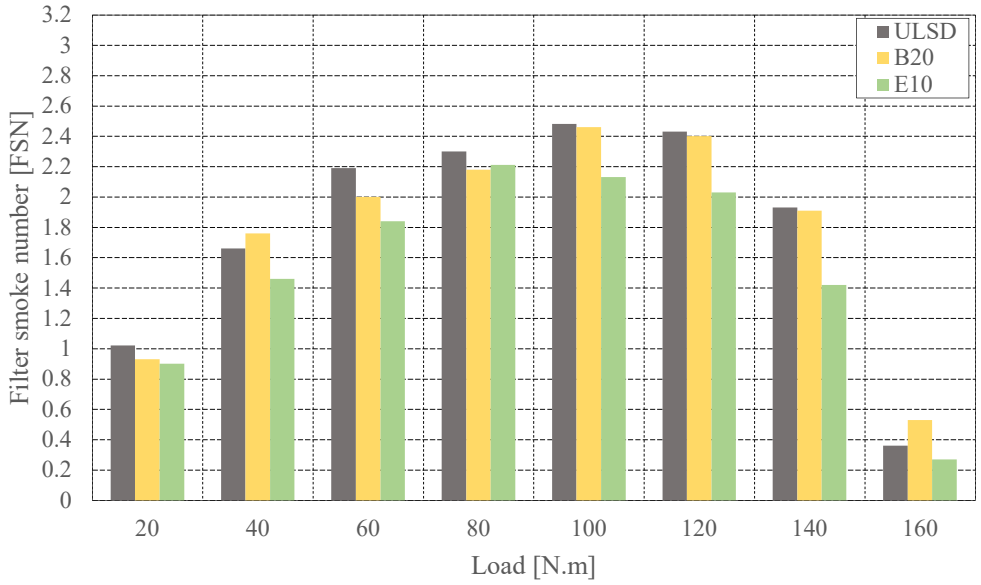

Figure 37: Soot at 1800 RPM

Figure 38 presents a break in the expected trend of ULSD having highest the filter smoke number. In this case at 2400 *RPM*, the B20 blend consistently has the highest filter smoke number of the three fuels tested. The E10 blend also exhibits higher levels of filter smoke number from 80 *N.m* onwards. Figure 39 however, follows the trend of the expected reduction in filter smoke number for the B20 and E10 fuel blends. Filter smoke numbers at 3000 *RPM* are consistent with Blom's (2015) results.

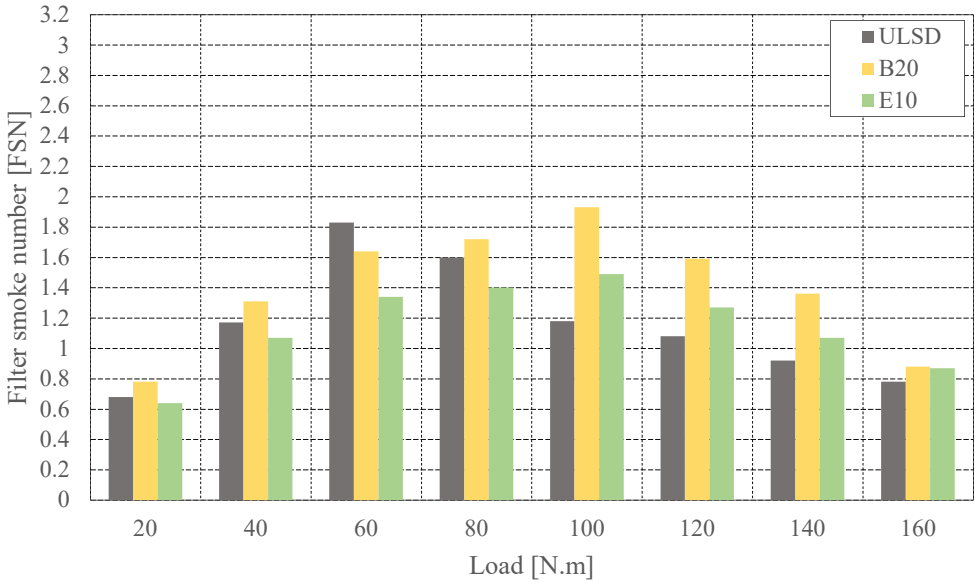

Figure 38: Soot at 2400 RPM

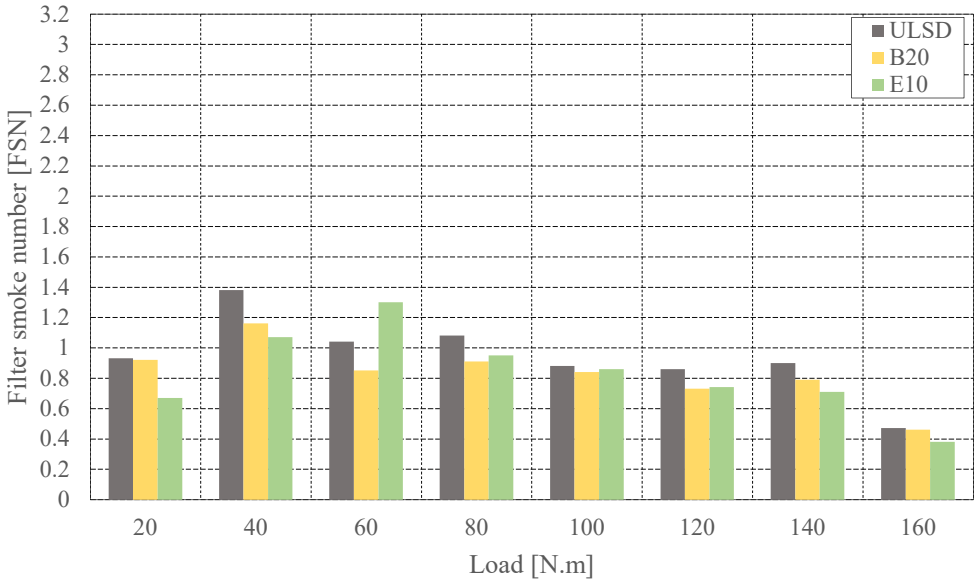

Figure 39: Soot at 3000 RPM

5.2.3. Oxygen

Oxygen concentration for all fuel blends show a decrease in concentration with an increase in load for each speed set point as illustrated by Figure 40 to Figure 42. This is a function not only due to the increasing fuel delivery to the engine but also of the diminishing influence of the dilution effect of recirculated exhaust gas being introduced to the intake manifold (Ladommatos, et al., 1998).

The increase of the oxygen concentration at 160 *N.m* for both the 1800 *RPM* and 3000 *RPM* is explained by the exhaust gas recirculation being deactivated. This allows only atmospheric air into the intake manifold which negates the dilution effect the recirculated exhaust gas has on the total intake charge (Ladommatos, et al., 1998) (Abd-Alla, 2002). This conclusion is substantiated when considering the trend shown in Figure 41.

The oxygen concentration shows a steady decreasing trend with no significant increases in oxygen concentration as any added oxygen is used to form more nitrogen oxides due to the combustion temperature increasing with the increase in load. This observation is reinforced by looking at Figure 41, where exhaust gas recirculation was present for all the load points at the 2400 *RPM* speed set point.

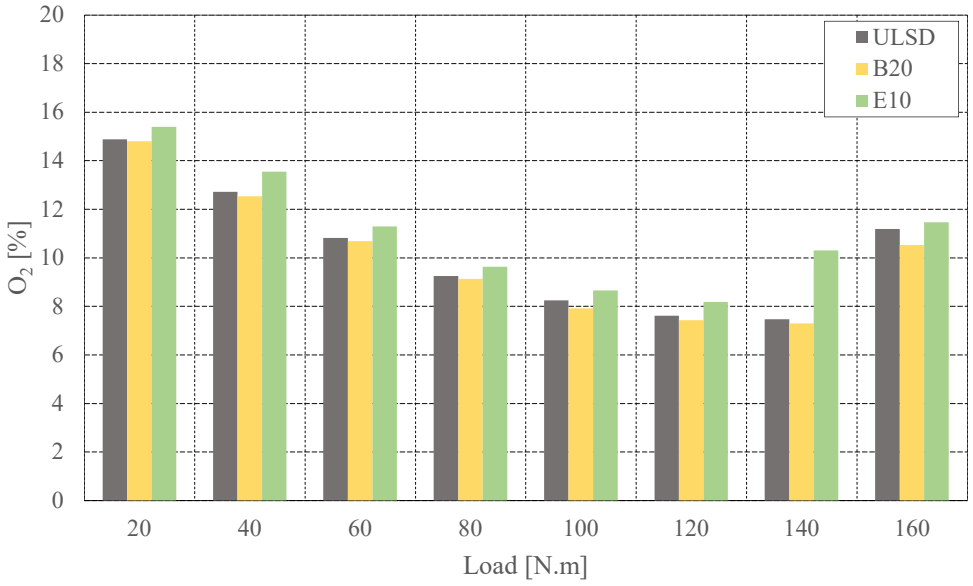

Figure 40: Oxygen concentration at 1800 RPM

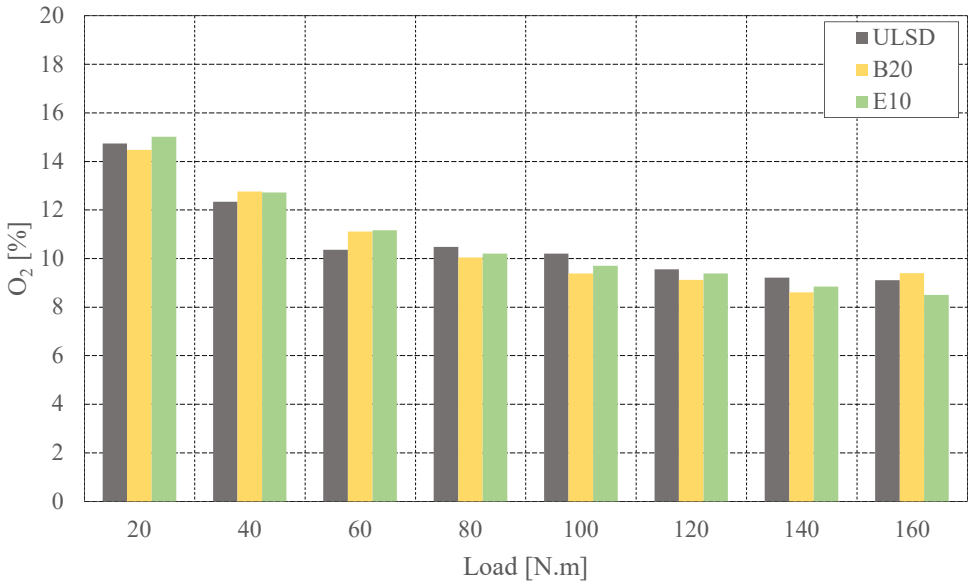

Figure 41: Oxygen concentration at 2400 RPM

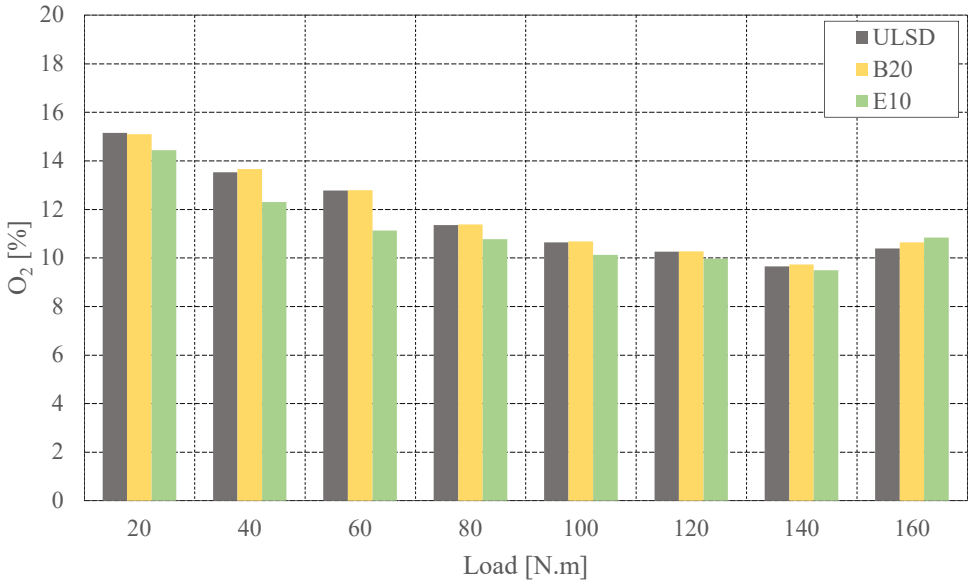

Figure 42: Oxygen concentration at 3000 RPM

The higher level of oxygen for the E10 blend at 1800 *RPM*, 140 *N.m* is due to the control function of the engine control unit at that point. The engine displayed very erratic control of the poppet valve at this point, leading to surges in fresh air being induced to the intake manifold, which in turn gives rise to the higher oxygen concentration at this point when compared to the other fuels. This phenomenon was re-tested and confirmed to occur at this set point The levels of oxygen present in the exhaust gas, for the rest of the set points, is consistent when compared to results in literature (Ladommatos, et al., 1998) (Rashedul, et al., 2014).

5.2.4. Carbon dioxide

The formation of carbon dioxide is highly dependent on the concentration of oxygen during combustion, allowing the carbon monoxide to form carbon dioxide in the presence of excess oxygen. Figure 43 shows a consistent trend of carbon dioxide concentration, with the E10 blend showing the lowest levels in carbon dioxide. The B20 blend consistently has the highest concentration of carbon dioxide across all operating points at the 1800 *RPM* speed range. This could be due to partial combustion at lower speeds, similar to results obtained by Maina (2014). This trend becomes much less pronounced at higher speeds, as Figure 44 and Figure 45 shows.

The influence of exhaust gas recirculation at this speed is clearly visible when comparing it with the 1800 *RPM* and 3000 *RPM* speed ranges. Whenever the exhaust gas recirculation is deactivated the amount of carbon dioxide drops between 15 to 30 percent when comparing the 140 *N.m* with the 160 *N.m* load point as seen in Figure 43 and Figure 45 as less dilution from the carbon dioxide in the recirculated exhaust gas results in a greater volume percentage oxygen. Carbon dioxide levels are consistent when comparing the results to similar studies in literature (Maina, 2014).

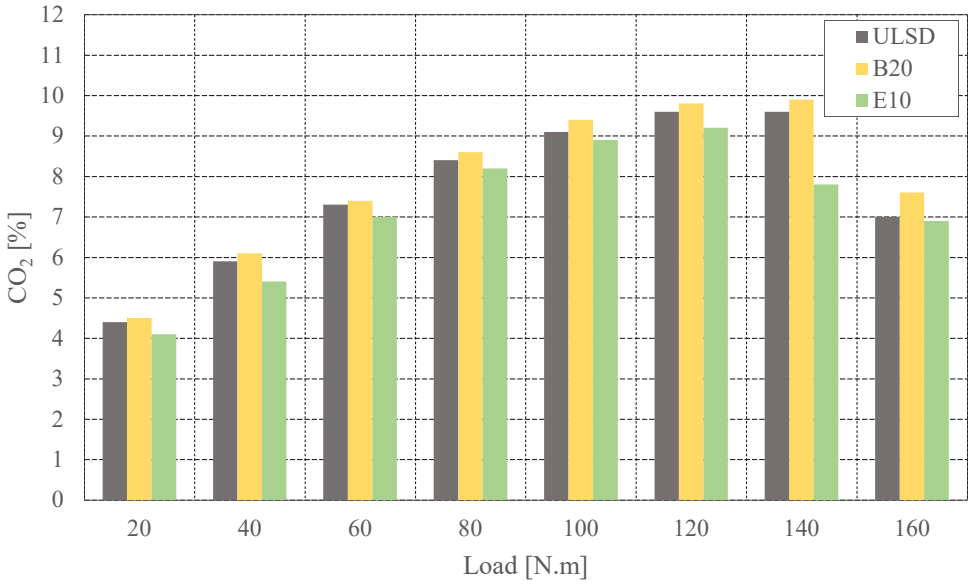

Figure 43: Carbon dioxide concentration at 1800 RPM

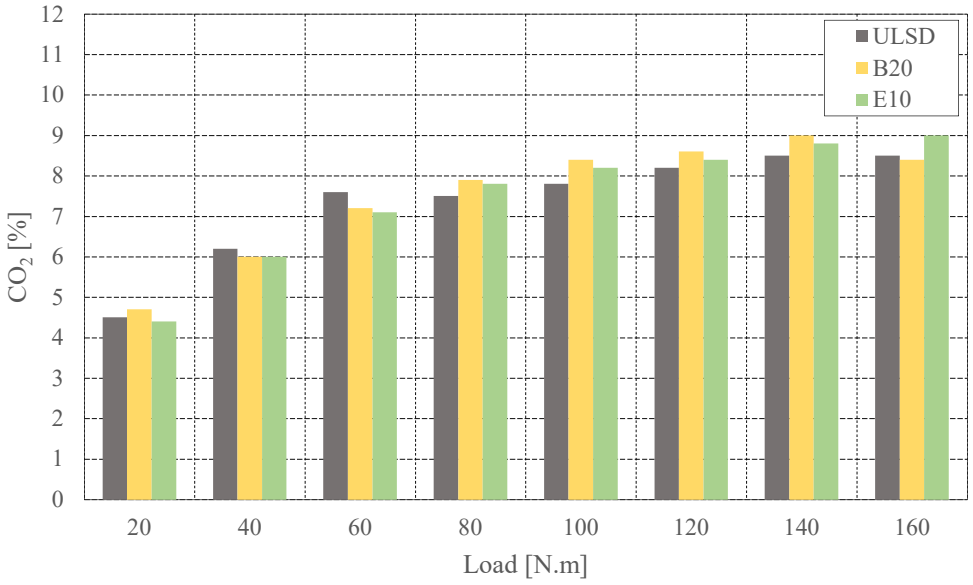

Figure 44: Carbon dioxide concentration at 2400 RPM

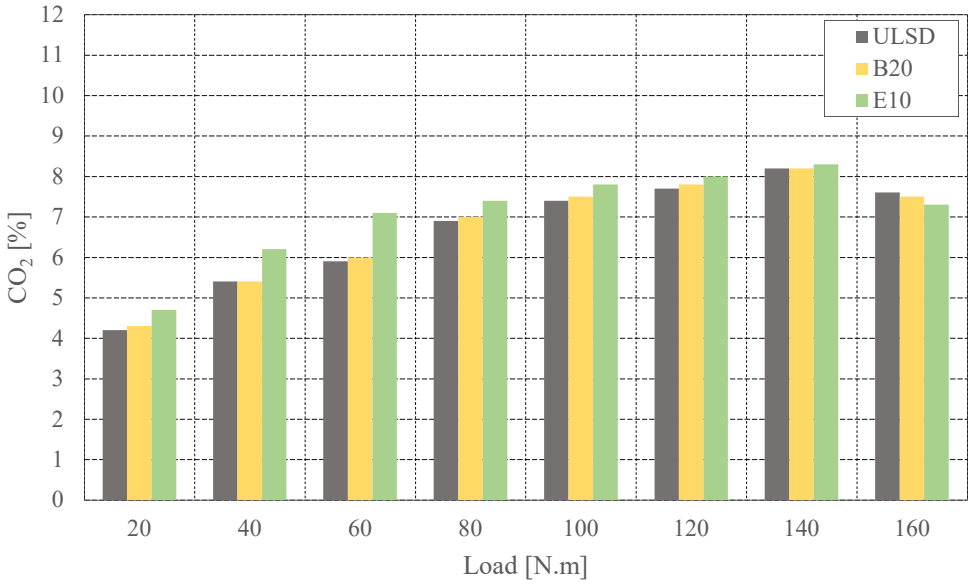

Figure 45: Carbon dioxide concentration at 3000 RPM

5.2.5. Carbon monoxide

Carbon monoxide rates decrease with decreasing exhaust gas recirculation rate. The recirculated exhaust gas displaces the oxygen in the inlet (Stone, 1992). The overall lower levels of carbon monoxide in diesel engines are mainly due to combustion efficiencies resulting from partial combustion, as in an ideal diesel combustion no carbon monoxides are formed (Datta & Mandal, 2016) (Mollenhauser & Tschoeke, 2010). An increase in load usually leads to an increase in combustion efficiency and has been shown in literature to produce lower carbon monoxide emissions. Low levels of carbon monoxide are often an indicator of a well-designed engine (Heywood, 1988).

The carbon monoxide for all fuels decrease with an increase in load for all three speed set points seen in Figure 46 to Figure 48. The results correlate well with the results obtained by Blom (2015), with initial carbon monoxide levels being very high when compared to the other fuels operating points. As with Blom (2015) the difference between the ULSD and the B20 fuels the carbon monoxide are negligible.

Figure 48 shows a steady decrease in carbon monoxide levels for the ULSD and B20 fuels. Carbon monoxide levels for E10 are initially significantly higher but decrease quickly to match the ULSD and E10 fuels. Increases in carbon monoxide levels are consistent with literature (Ghadikolaei, 2016) (Richards, 2014).

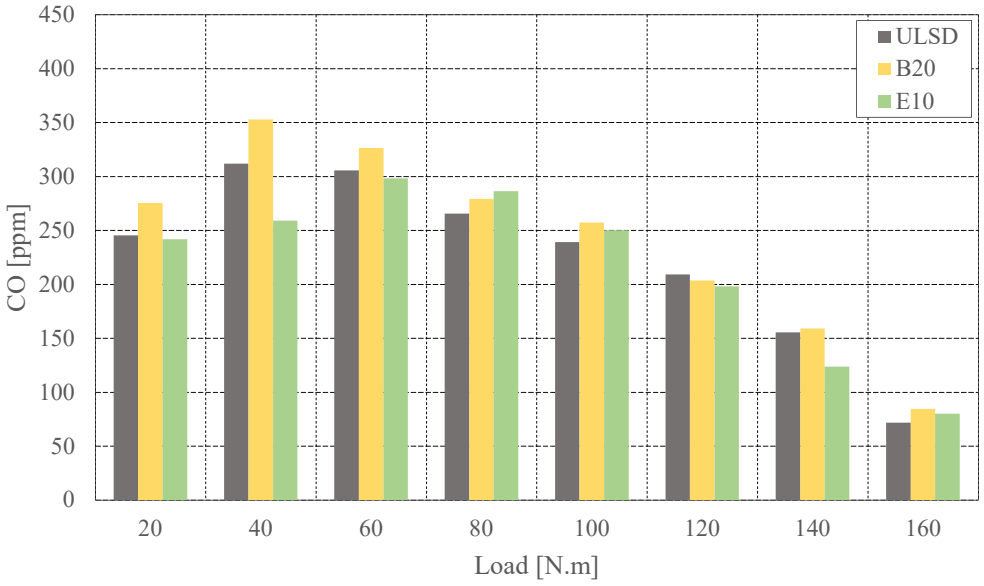

Figure 46: Carbon monoxide concentration at 1800 RPM

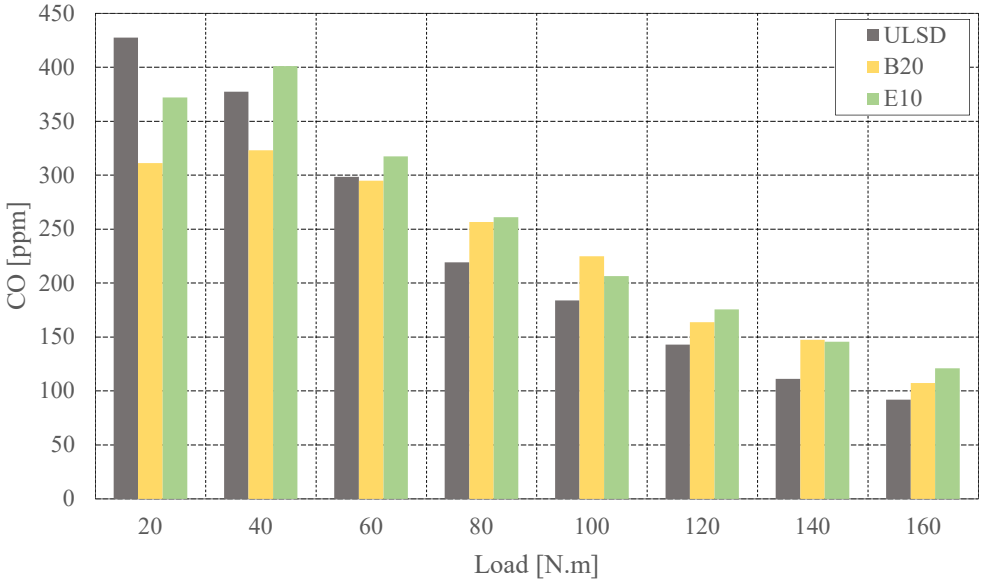

Figure 47: Carbon monoxide concentration at 2400 RPM

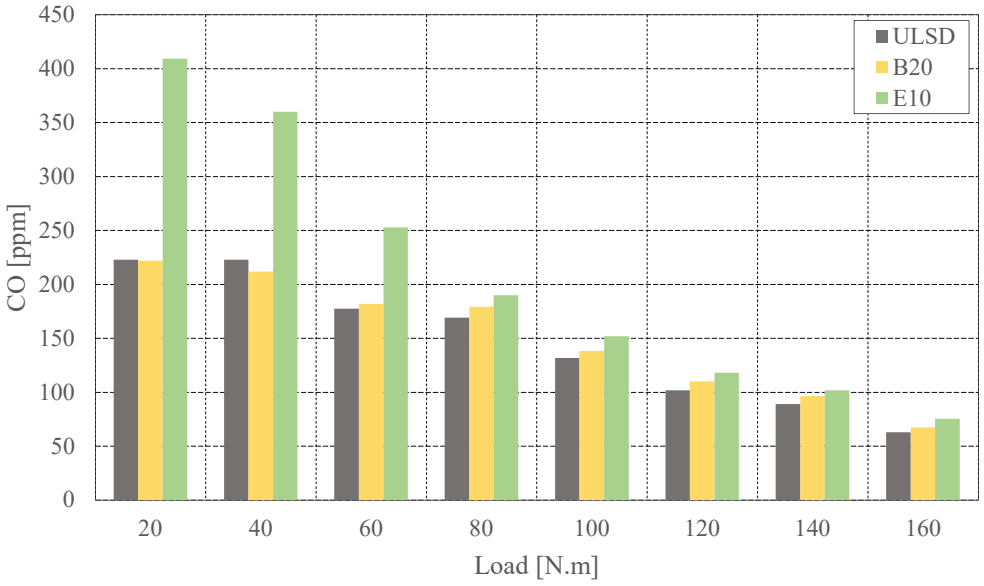

Figure 48: Carbon monoxide concentration at 3000 RPM

5.3. Brake specific fuel consumption

The brake specific fuel consumption for the different fuel blends are largely consistent, with the B20 blend having a slightly higher fuel consumption over most of the operating points. The low load fuel consumption for the E10 blend showed higher fuel consumption than the other two blends for speeds of 1800 *RPM* and 2400 *RPM*, as seen in Figure 49, Figure 50 and Figure 51. This trend quickly dissipates as the load increases however. The higher brake specific fuel consumption for the biofuel blends can be attributed to the higher exhaust gas recirculation rates for these fuels (Stone, 1992).

The slight increase in fuel consumption can also be attributed to the lower calorific value of the B20 and E10 as these blends need a higher injection quantity per stroke to operate at the same operating point than the ULSD fuel (Richards, 2014). This is supported when interrogating VCDS as slightly higher injection quantities are observed. The results obtained by Blom (2015) in literature corroborate this finding (Datta & Mandal, 2016).

No noticeable improvement in fuel consumption can be attributed to the deactivation of the exhaust gas recirculation system at 160 *N.m*. With regards to the control strategy employed by the engine control unit, the conclusion can be made that for low fraction biofuel blends such as the B20 and E10, fuel consumption is not adversely impacted in the short term.

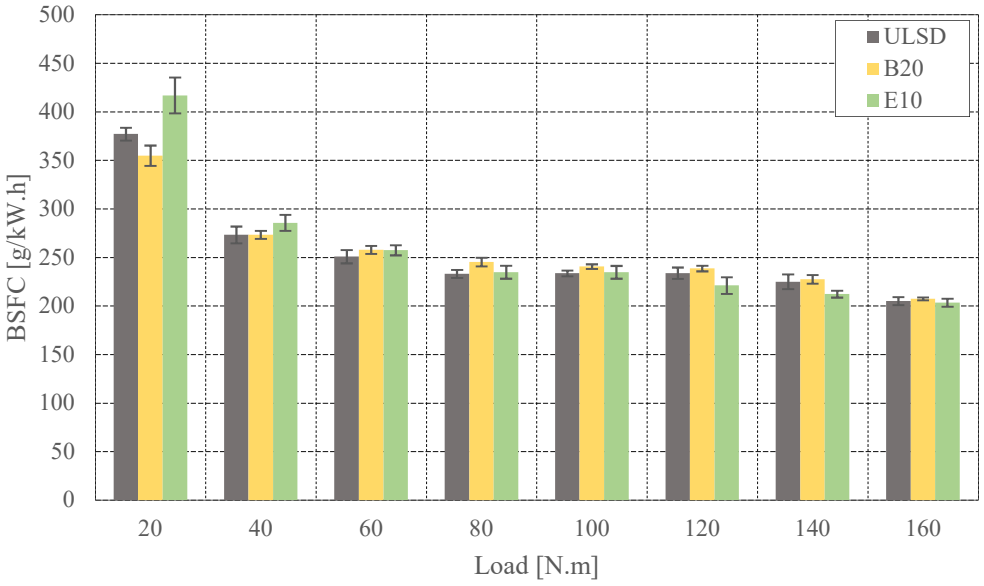

Figure 49: Brake specific fuel consumption at 1800 RPM

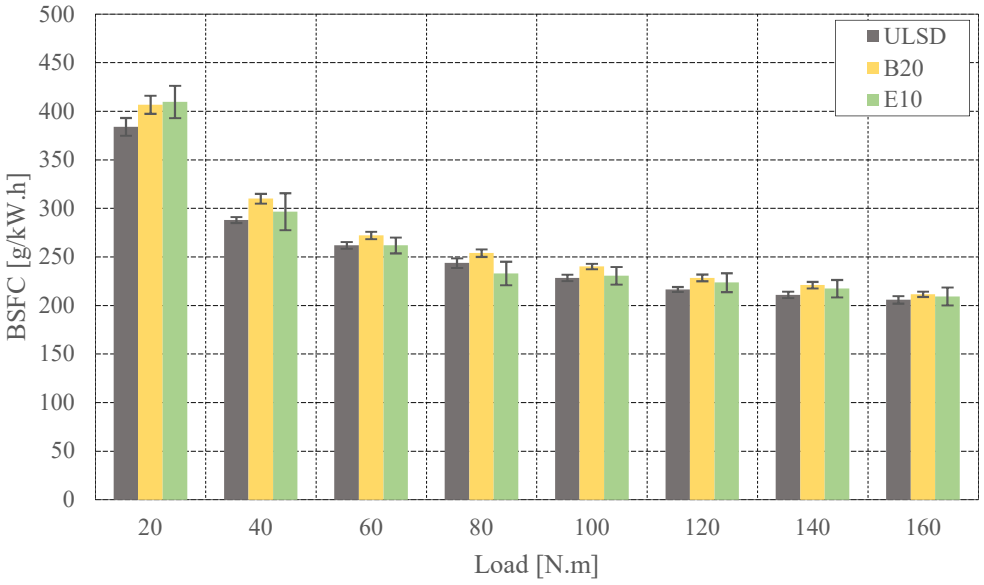

Figure 50: Brake specific fuel consumption at 2400 RPM

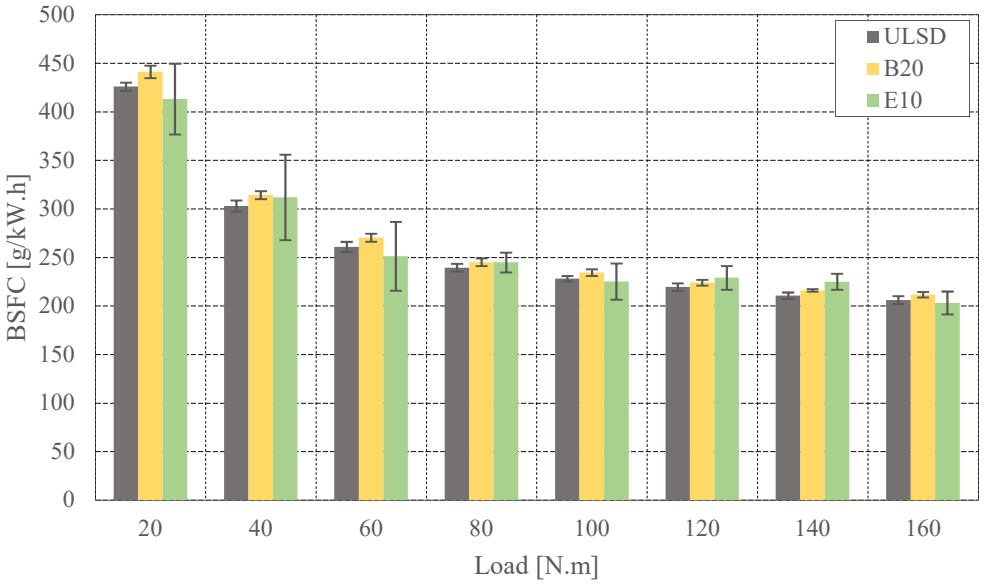

Figure 51: Brake specific fuel consumption at 3000 RPM

The general trend would suggest that an increased exhaust gas recirculation rate results in a higher brake specific fuel consumption. This finding is substantiated in literature (Zheng, et al., 2004) .

5.4. Exhaust gas and intake air temperatures

The intake air and exhaust gas temperatures are important parameters to consider when analysing different fuels especially biodiesel and ethanol blended fuels, as these fuels change the combustion phenomena inside the cylinder. The reason for cooled exhaust gas recirculation system becomes apparent when considering the intake and exhaust temperatures in an engine equipped with exhaust gas recirculation. Higher intake air temperature will lead to a higher exhaust gas temperature which is recirculated to the intake manifold. Higher intake charge temperatures facilitate the increased formation of nitrogen oxides during combustion (Jääskeläinen & Khair, 2011) (Ladommatos, et al., 1998).

The results obtained by Blom (2015) show the same increasing trend for the exhaust gas temperatures with increased load observed in literature (Datta & Mandal, 2016). The slightly lower temperatures obtained are expected since the charge air cooling has been improved by replacing the OEM intercooler with a water-to-air intercooler, which lowers the post-intercooler charge air temperature mixing with the recirculated exhaust gas considerably. The increased latent heat of vaporization is responsible for the lower exhaust gas temperatures as seen in Figure 52 to Figure 54. This finding was established by Blom (2015) and is corroborated in literature (Cole, et al., 2000)

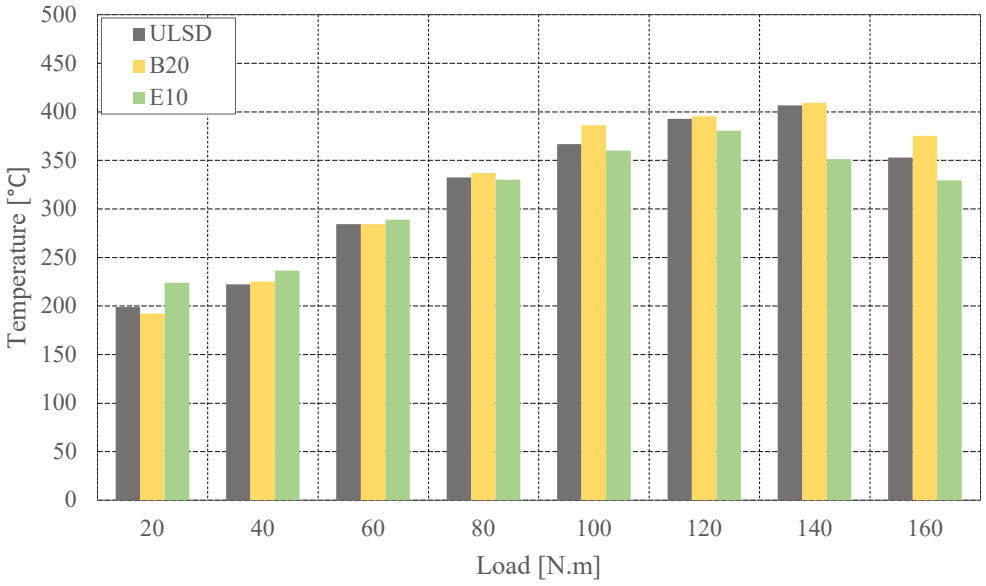

Figure 52: Exhaust gas temperature at 1800 RPM

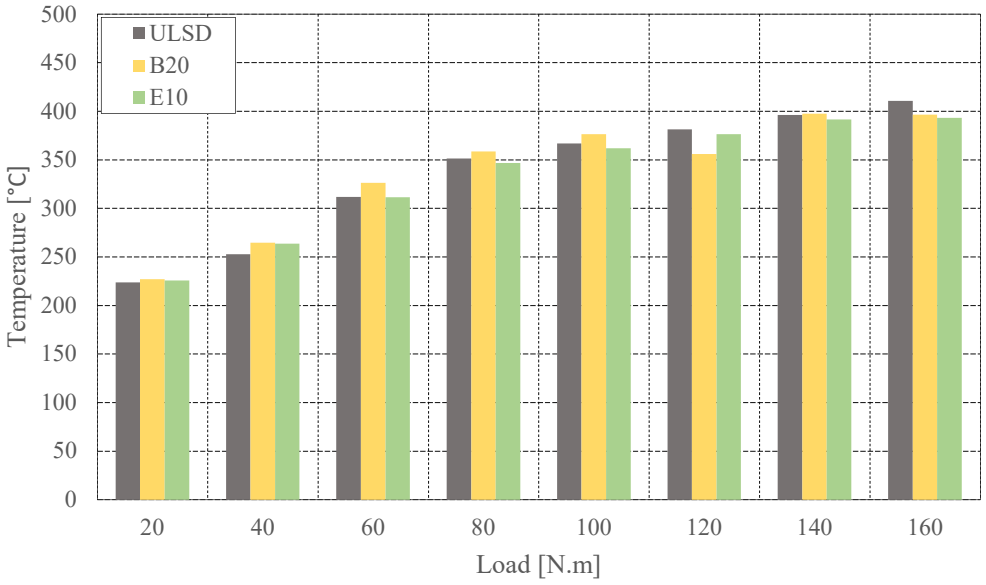

Figure 53: Exhaust gas temperature at 2400 RPM

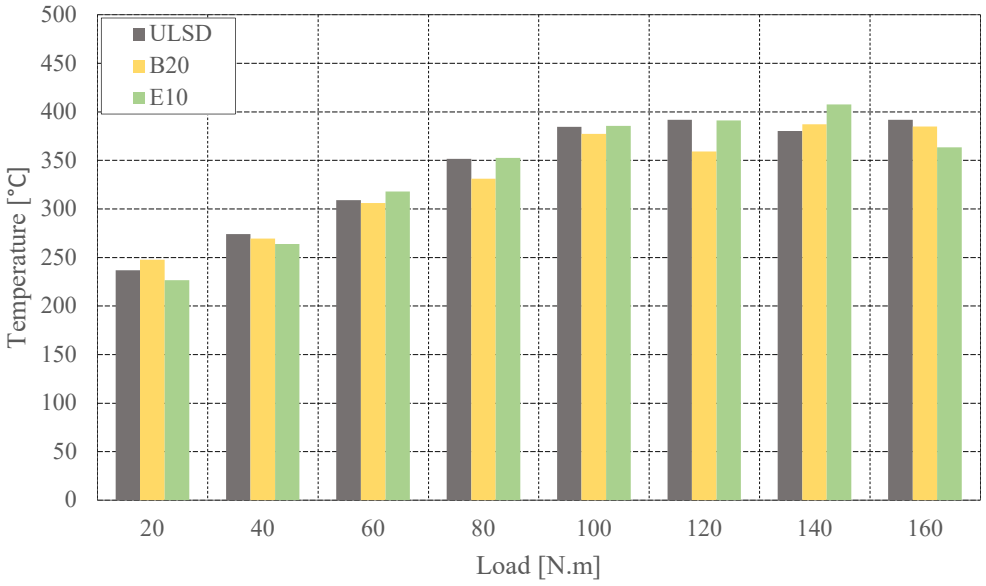

Figure 54: Exhaust gas temperature at 3000 RPM

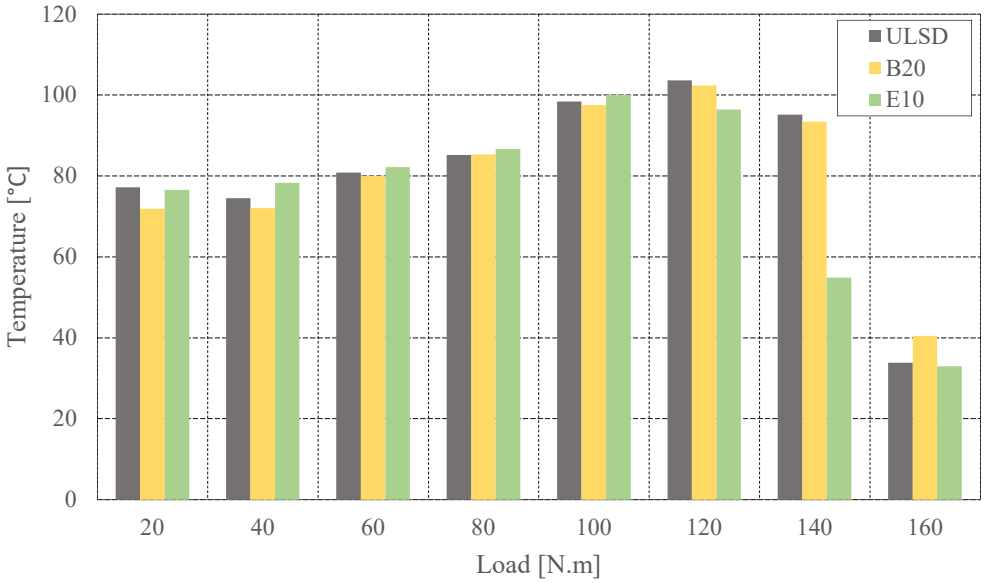

Figure 55: Intake charge temperature at 1800 RPM

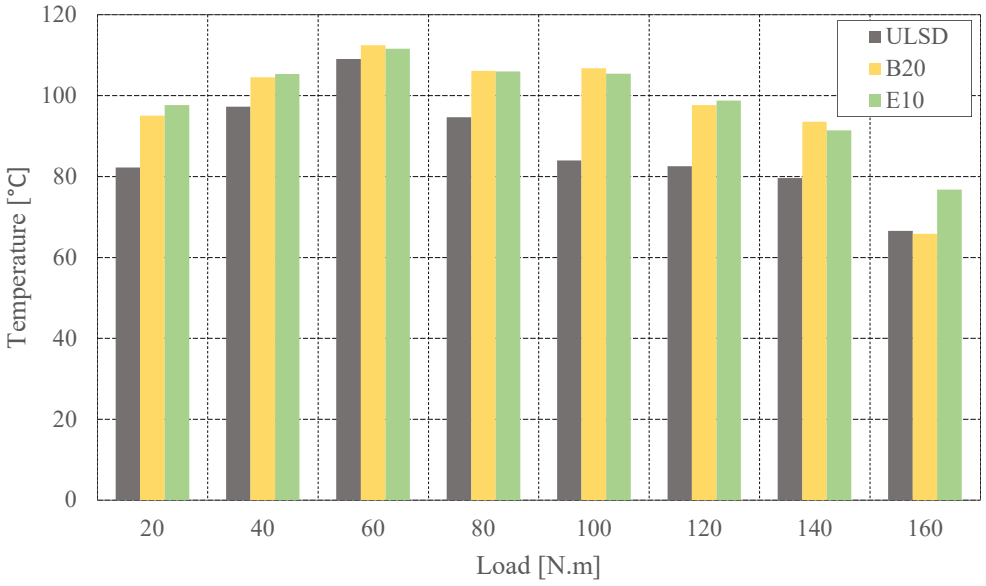

Figure 56: Intake charge temperature at 2400 RPM

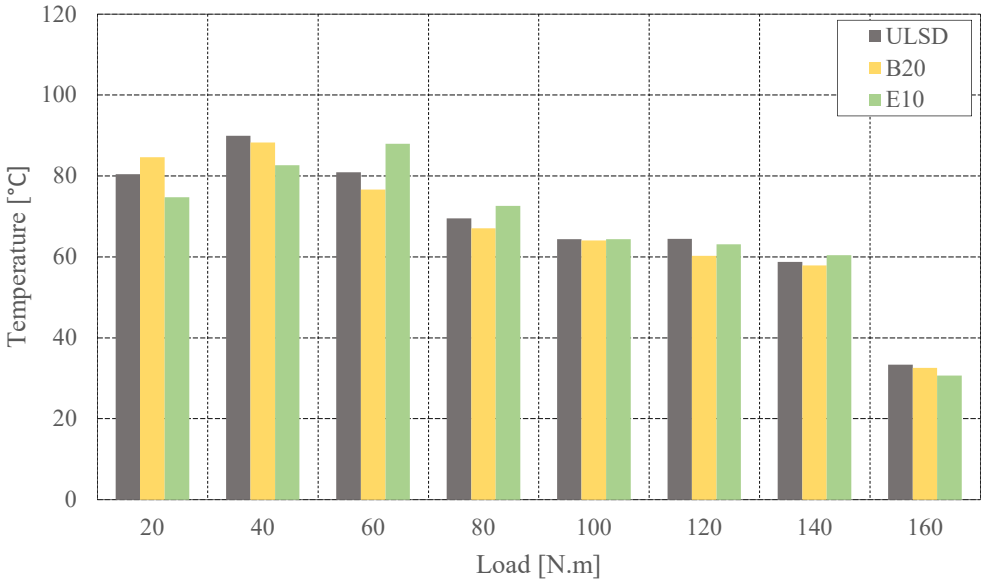

Figure 57: Intake charge temperature at 3000 RPM

The effect the increased exhaust gas recirculation rate has on the intake charge temperature is illustrated when comparing Figure 30 and Figure 56. The B20 and E10 blends show higher intake charge temperatures corresponding with the increased exhaust gas recirculation rate as discussed in section 5.1.

5.5. Compressor performance

The analysis of the compressor performance using the different test fuels did not yield any noticeable deviation when consulting the data. This would suggest that the control strategy employed by the engine control unit with regards to the boost pressure is open loop. The duty cycle for the actuator controlling the variable vanes on the turbine reinforces this conclusion as the movement of the actuator does not vary significantly at any operating point once steady state operation was achieved (Jääskeläinen, 2016). The following curves therefore only illustrate the ULSD for clarity.

Figure 58 shows the total-to-total pressure ratio versus mass air flow of the compressor for the ULSD. It is evident that at engine operating points of 1800 *RPM* between 20 *N.m* and 120 *N.m* there is a greater rate of increase in boost pressure for changes in inlet air mass flow rate, as indicated by the steep gradient shown below suggesting a trend towards greater efficiency.

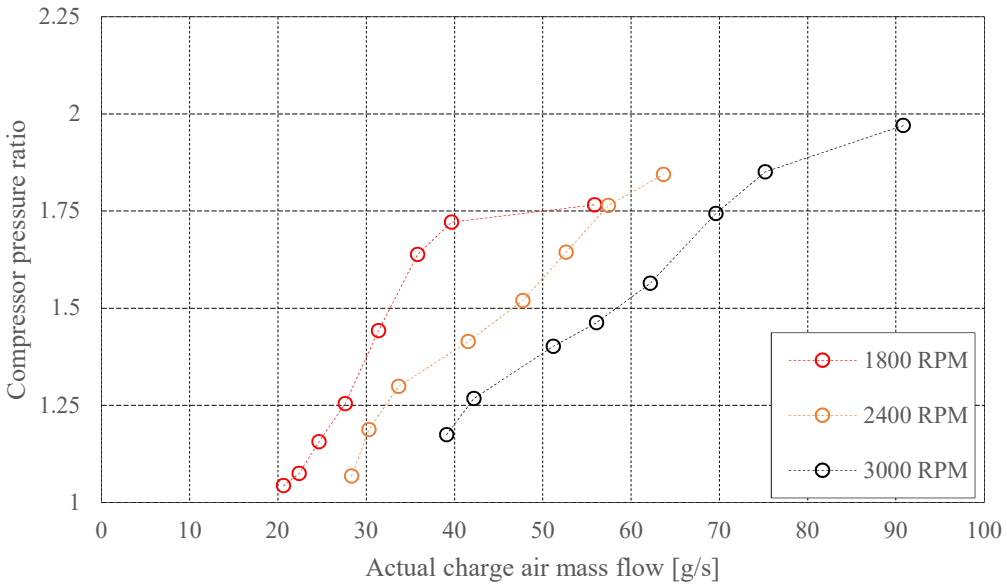

Figure 58: Compressor pressure ratio versus mass flow for ULSD

The compressor efficiency at 1800 *RPM* and 2400 *RPM* at low loads is relatively low but quickly increases as the charge air flow increases for each consecutive load point. The compressor typically operates between 65 to 75 percent efficiency for loads beyond 80 *N.m* for all speed set points tested as seen in Figure 59.

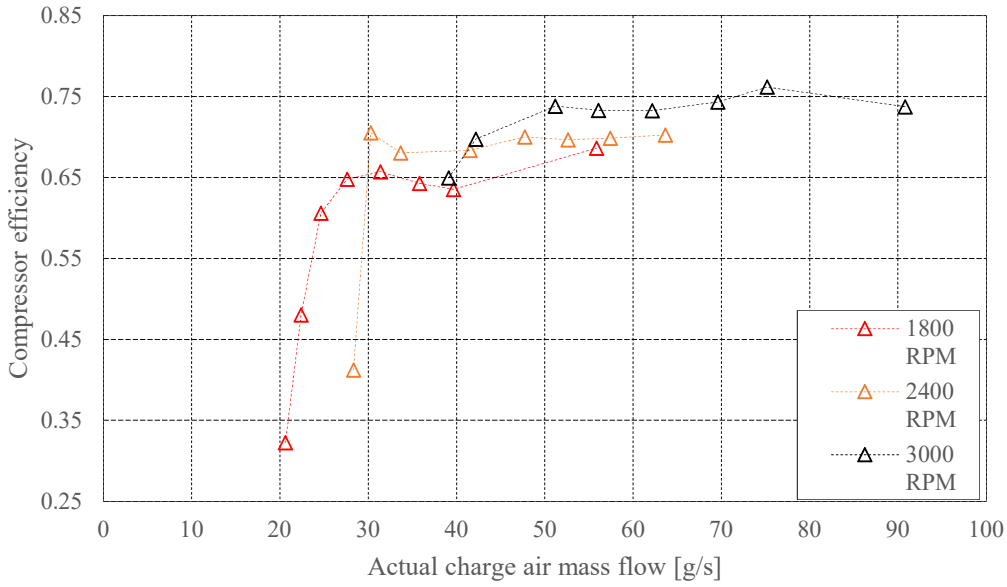

Figure 59: Compressor efficiency versus mass flow for ULSD

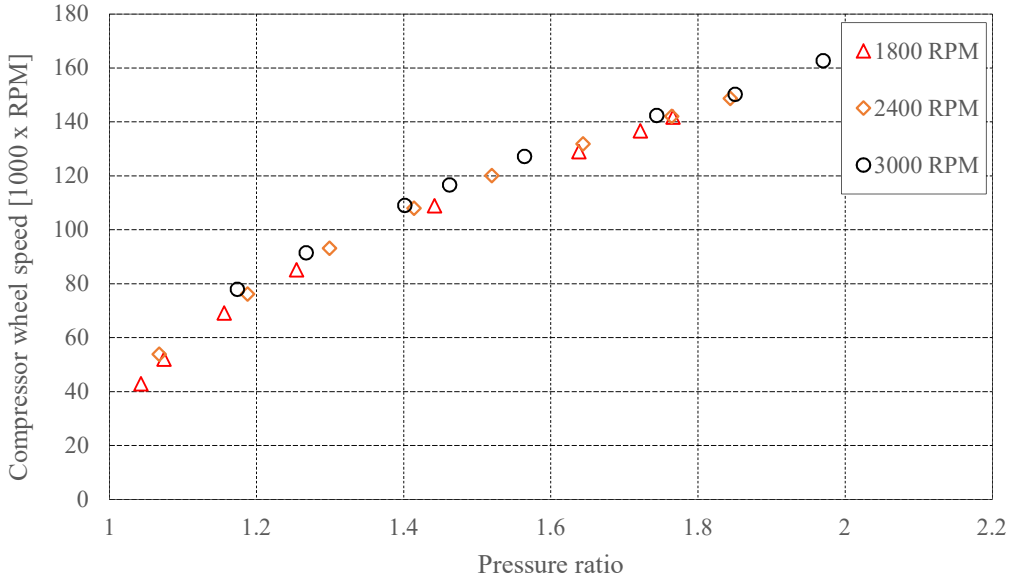

Figure 60: Compressor wheel speed versus pressure ratio for ULSD

Figure 60 shows the characteristic compression trend of the compressor for the points tested. The deviation from the trend shown above between the different fuels tested is negligible. The idling speed of the compressor wheel was observed to be approximately 20 000 *RPM*.

6. CONCLUSIONS AND RECOMMENDATIONS

The measurement capabilities of the turbocharged diesel test bench have been expanded to include measurements of both the turbocharger and exhaust gas recirculation systems.

Upgrades to the measurement of the exhaust gas recirculation system include a venturi tube for the measurement of the recirculated exhaust flow to the intake manifold as well as temperature and pressure of the flow. The compressor side of the turbocharger has been thoroughly instrumented. Pressure and temperature measurements can be taken from both the inlet and outlet of the compressor. A compressor wheel speed sensor has also been installed. Further measurements of interest to the setup include exhaust back pressure measurement as well as intercooler charge temperature and intake manifold temperature.

The high-speed multifunction National Instruments USB-6351 data acquisition device used by Blom (2015) has been fully utilised to include the abovementioned instruments. An addition of a dedicated high precision temperature data acquisition instrument was needed to capture the additional temperature measurements as the high-speed data acquisition device does not include cold junction compensation.

The software program to read the expanded measurements setup was developed. The current hardware restriction at present however prevents the integration of the in-cylinder pressure acquisition program developed by Blom (2015) with the newly developed program used to acquire the exhaust gas recirculation and turbocharger data.

The venturi tube performs as expected at high exhaust gas recirculation rates, producing a steady measurement of the exhaust gas flow. Similar exhaust gas recirculation rates have been reported in literature (Stone, 1992) (Jääskeläinen & Khair, 2014).

Testing of the B20 blend was successful. The E10 blend presented difficulties in measuring fuel consumption due to the formation of vapour bubbles in the fuel lines.

Recommendations for further investigations include:

- An investigation into replacing the ETA control software with a more modern programming interface, such as LabVIEW.
- An investigation into gaining direct access to the engine's control functions.
- A study on the effects different additives have on the engine performance characteristics as well as the emissions profile of the exhaust gas.
- Improving the exhaust gas recirculation system by including cooling, an upgraded valve and a lambda sensor could alleviate the difficulties with measuring hot exhaust flow.

- Expanding the turbine measurements to include inlet and outlet pressure and temperature measurement.
- Improving the fuel conditioning unit to deal with vapour in the fuel line.
- Incorporating all emissions measuring equipment into a portable rack setup capable of interfacing with a PC.

7. REFERENCES

Abd-Alla, G., 2002. Using exhaust gas recirculation in internal combustion engines: a review. *Energy conversion management,* Volume 43, pp. 1027-1042.

Abu-Hamdeh, N. & Alnefaie, K., 2015. A comparitive study of almond biodiesel-diesel blends for diesel engine in terms of performance and emissions. *BioMed research international,* Volume 2015, pp. 1-8.

ACAM, 2015. *Picoturn 1st generation rotational speed measuremnt system for turbochargers.* Stutensee: acam messelectronic GmbH.

Agarwal, D., Singh, S. K. & Agarwal, A. K., 2011. Effect of exhaust gas recirculation (EGR) on performance, emissions, deposists and durability of a constant speed compression ignition engine. *Applied Energy,* Volume 88, pp. 2900-2907.

Agrawal, A., Singh, S., Sinha, S. & Shukla, M., 2004. Effect of EGR on the exhaust gas temperature and exhaust opacity in compression ignition engines. *Sadhana,* 29(3), pp. 275-284.

Alternative Fuels Data Center, 2014. *Alternative fuels data center - Fuel properties comparison.* [Online]
Available at: www.afc.energy.gov/fuels/fuel_comparison_chart.pdf
[Accessed 1 July 2016].

Arnold, S., 2004. *Vane design for use in variable geometry turbocharger.* United Stats of America, Patent No. 6,672,059.

ASTM D6371, 2017. *Standard test method for cold-filter plugging point of diesel and heating fuels.* West Conshohocken, PA: ASTM International.

Audi AG, 2016. *Turbochargers with variable turbine geometry (VTG).* [Online]
Available at: https://www.audi-technology-portal.de/en/drivetrain/tdi-engines/turbochargers-with-variable-turbine-geometry-vtg
[Accessed 20 November 2017].

AVL, 1987. *Operating instruction AVL 730 dynamic fuel consumption measuring equipment.* Graz: AVL GmbH.

AVL, 1998. *Operating manual - AVL 415 variable sampling smoke meter.* s.l.:AVL GmbH.

Baert, R., Beckman, D. & Veen, A., 1999. Efficient EGR technology for future HD diesel engine emission targets. *SAE technical paper.*

Baines, N., 2005. *Fundamentals of turbocharging.* 1st ed. s.l.:Concepts NREC.

Benedict, R., 1984. *Fundamentals of temperature, pressure and flow measruements.* 2nd ed. s.l.:John Wiley & Sons.

Benson, T., 2014. *Stagnation temperature - real gas effects.* [Online]
Available at: https://www.grc.nasa.gov/www/BGH/stagtmp.html
[Accessed 30 September 2017].

Blanchard, B. & Fabrycky, W., 2011. *Systems Engineering and Analysis.* Upper Saddle River, New Jersey: Pearson Education, Inc..

Blom, C., 2015. *Diesel engine performance using oxygenated fuels,* Stellenbosch: Stellenbosch University.

Brian, M., 2000. *How diesel engines work.* [Online]
Available at: auto.howstuffworks.com/diesel1.htm
[Accessed 20 November 2016].

Buenaventura, F., Witrant, E., Talon & V. Dugard, L., 2013. *Simultaneous air fraction and low-pressure EGR mass flow rate estimation for diesel engines.* Grenoble, France, IFAC Joint conference SSSC - 5th symposium on system structure and control.

Byttner, S. & Holmberg, U., 2008. *Closed-loop control of EGR using ion currents.* Innsbruk, ACTA Press.

Can, O. et al., 2016. Combined effects of soybean biodiesel fuel addition and EGR application on the combustion and exhaust emission in a diesel engine. *Applied thermal engineering,* Volume 95, pp. 115-124.

Carter, J., Sharp, N. & Tennant, H., 2010. Turbocharging technologies for heavy-duty diesel engines. In: H. Zhao, ed. *Advanced direct injection combustion engine technologies and development.* Boca Raton: Woodhead Publishing Ltd., pp. 318-357.

Cengel, Y. & Boles, M., 2007. *Thermodynamics - An engineering approach.* 6th ed. New york: McGraw-Hill.

Cengel, Y. & Cimbala, J., 2006. *Fluid mechanics: fundamentals and pplications.* 2nd ed. New York: McGraw-Hill.

Challen, B. & Baranescu, R., 1999. *Diesel engine reference book.* 2nd ed. Woburn: Butterworth-Heinemann.

Chevron, 2007. *Diesel fuels technical review.* San Ramon: Chevron Corporation.

Childs, P., 2001. *Practical temperature measurements.* 1st ed. s.l.:Butterworth-Heinemann.

Cole, R. et al., 2000. *Effect of ethanol fuel additive on diesel emissions,* s.l.: Argonne National Laboratory.

Datta, A. & Mandal, K., 2016. Impact of alcohol addition to diesel on the performance combustion and emissions of a compression ignition engine. *Applied thermal engineering,* Volume 98, pp. 670-682.

Department of mechanical and mechatronic engineering , n.d. *DISA instruction and service manual for type 55D41 anemometer unit.* Stellenbosch: DISA.

DieselNet, 2002. *Fuel properties and emissions.* [Online]
Available at: https://www.dieselnet.com/tech/fuel_emi.php
[Accessed 2 July 2016].

Dräger, 2011. *Instruction manual MSI 150 Euro-4.* Hagen: Dräger MSI GmbH.

Druck Ltd., 1999. *DPI 610 IS portable pressure calibrator/indicator user guide K239.* s.l.:Druck Ltd.

Endress+Hauser, 2016. *Technical information.* s.l.:Endress+Hauser (Pty) Ltd..

Essay UK, 2016. *Dissertation: significance of viscosity in functioning of diesel engine.* [Online]
Available at: http://www.essay.uk.com/essays/engineering/dissertation-significance-of-viscosity-in-functioning-of-diesel-engine/
[Accessed 1 September 2016].

Feneley, A., Pesiridis, A. & Andwari, A., 2017. Variable geometry turbocharger technologies for exhaust energy recovery and boosting - A review. *Renewable and sustainable energy reviews,* Volume 71, pp. 959-975.

Ferguson, C. & Kirkpatrick, A., 2001. *Internal combustion engines applied thermosciences.* 2nd ed. Danvers, MA: John Wiley & Sons, Inc.

Fluke, 2010. *P5514, P5514-V & P5514-EP Hydraulic comparison test pump user manual.* Everett, WA: Fluke Corporation.

Fluke, 2013. *9142, 9143, 9144 Field metrology well user's guide.* Everett, WA: Fluke Corporation.

Fluke, 2014. *9150 Portable furnace user's guide.* Everett, WA: Fluke Corporation.

Ghadikolaei, M., 2016. Effect of alcohol blend and fumigation on regulated and unregulated emissions of IC engines - A review. *Renewable and sustainable energy review,* Volume 57, pp. 1440-1495.

Golloch, R., 2005. *Downsizing bei verrennungsmotoren.* s.l.:Springer.

Hall, N., 2015. *Dynamic Pressure.* [Online]
Available at: https://www.grc.nasa.gov/www/k-12/airplane/dynpress.html
[Accessed 30 September 2017].

Hawley, J. e. a., 1991. *Reduction of steady state NOx levels from an automotive diesel engine using optimized VGT/EGR schedules,* s.l.: SAE International.

Heywood, J., 1988. *Internal combustion engine fundamentals.* International ed. New York: McGraw Hill, Inc.

Hiereth, H. & Prenninger, P., 2007. *Charging the internal combustion engine.* 2nd ed. Wien: Springer Wien New York.

Honeywell, Garrett, 2017. *Turbo tech Expert.* [Online]
Available at: https://www.turbobygarrett.com/turbobygarrett/turbo_tech_expert
[Accessed 4 December 2016].

Huba, 2013. *Relative and absolute pressure transmitter type 691.* Würenlos: Huba Control.

IBSA dialogue forum, 2010. *IBSA dialogue forum: Investigation into harmonization of IBSA biofuels specifications and standards.* Johannesburg, Department of Energy: New and Renewable Energy Directorate of South Africa.

ISO 5167-1, 2003. *Measurement of fluid flow by means of pressure differential devices inserted in circular cross-section conduits running full- Part 1: General principles and requirements.* 2nd ed. Geneva, Switzerland: International Organization for Standardization.

ISO 5167-4, 2003. *Measurement of fluid flow by measn of pressure differential devices inserted in circular cross-section conduits running full - Part 4: Venturi tubes.* 1st ed. Geneva, Switzerland: International Organization for Standardization.

Jääskeläinen, H., 2009. *Biodiesel standards & properties.* [Online]
Available at: https://www.dieselnet.com/tech/fuel_biodiesel_std.php
[Accessed 15 September 2016].

Jääskeläinen, H., 2009. *Low temperature operability of biodiesel.* [Online]
Available at: https://www.dieselnet.com/tech/fuel_biodiesel_lowtemp.php
[Accessed 15 September 2016].

Jääskeläinen, H., 2011. *Diesel exhaust gas.* [Online]
Available at: https://www.dieselnet.com/tech/diesel_exh.php
[Accessed 23 November 2017].

Jääskeläinen, H., 2013. *Variable geometry turbochargers.* [Online]
Available at: https://www.dieselnet.com/tech/air_turbo_vgt.php
[Accessed October 2015].

Jääskeläinen, H., 2016. *EGR control strategy.* [Online]
Available at: https://www.dieselnet.com/tech/engine_egr_control.php
[Accessed 31 October 2016].

Jääskeläinen, H., 2016. *Ethanol-diesel blends.* [Online]
Available at: https://www.dieselnet.com/tech/fuel_ediesel.php
[Accessed 2 February 2016].

Jääskeläinen, H. & Khair, M., 2011. *Intake air management for diesel engines.* [Online]
Available at: https://www.dieselnet.com/tech/diesel_air.php
[Accessed 9 September 2016].

Jääskeläinen, H. & Khair, M., 2012. *EGR systems & components.* [Online]
Available at: https://www.dieselnet.com/tech/engine_egr_sys.php
[Accessed 11 September 2016].

Jääskeläinen, H. & Khair, M., 2014. *Engine fundamentals.* [Online]
Available at: https://www.dieselnet.com/tech/diesel_fundamentals.php
[Accessed 31 October 2016].

Jääskeläinen, H. & Khair, M., 2014. *Exhaust gas recirculation.* [Online]
Available at: https://www.dieselnet.com/tech/engine_egr.php
[Accessed 29 July 2015].

Jääskeläinen, H. & Khair, M., 2016. *Combustion in diesel engines.* [Online]
Available at: https://www.dieselnet.com/tech/diesel_combustion.php
[Accessed 1 August 2015].

Jääskeläinen, H. & Khair, M., 2016. *Turbocharger fundamentals.* [Online]
Available at: https://www.dieselnet.com/tech/air_turbocharger.php
[Accessed 25 August 2016].

Jaquet, 2016. *Speed sensor for turbochargers.* Basel, Switzerland: Jaquet Technology Group AG.

Jothithirumal, J. & Jamesgunasekaran, E., 2012. Combined impact of biodiesel and exhaust gas recirculation on NOx emissions in DI diesel engines. *Procedia Engineering,* Volume 38, pp. 1457-1466.

Karsten, L., 2014. *The design and development of a remote intercooler for a turbocharged diesel engine,* Stellenbosch: Stellenbosch University.

Khair, M. & Jääskeläinen, H., 2015. *Emission formation in diesel engines.* [Online]
Available at: https://www.dieselnet.com/tech/diesel_emiform.php
[Accessed 15 September 2016].

Kivevele, T., Kristóf, L., Bereczky, A. & Mbarawa, M., 2011. Engine performance, exhaust emissions and combustion characteristics of a CI engine fuelled with croton megalocarpus methyl ester with antioxidant. *Fuel,* Volume 90, pp. 2782-2789.

Knothe, G., Von Gerpen, J. & Krahl, J., 2005. *The biodiesel handbook.* 1st ed. Champaign, IL: AOCS Press.

Kotze, J., 2010. *A comparitive study on the performance of biodiesel in a 1.9 litre turbo diesel ngine,* Stellenbosch: Stellenbosch University.

Kröger, D., 1998. *Air-cooled heat exchangers and cooling towers - Thermal flow evaluation and design.* 1st ed. Stellenbosch: Stellenbosch University.

Ladommatos, N., Abdelhalim, S., Zhao, H. & Hu, Z., 1998. The effects of carbon dioxide in exhaust gas recirculation on diesel engine emissions. *Proceedings of the institution of Mechanical Engineers,* 212(Part D), pp. 25-42.

Laurantzon, F., 2010. *Flow Measuring Techniques in Steady and Pulsating Compressible Flows,* Stockholm: Royal Institute of Technology.

Lei, J., Bi, Y. & Shen, L., 2011. Performance and emission characteristics of diesel engine fueled with ethanol-diesel blends in different altitude regions. *Journal of biomedicine and biotechnology,* Volume 2011, pp. 1-10.

Liaquat, A. et al., 2013. Effect of coconut biodiesel fuels on engine performance and emission characteristics. *Procedia Engineering,* Volume 56, pp. 583-590.

Maina, P., 2014. Investigation of fuel properties and engine analysis of Jatropha biodiesel of Kenyan origin. *Journal of energy in Southern Africa,* 25(2), pp. 107-116.

Majewski, W. A. & Jääskeläinen, H., 2013. *What is diesel.* [Online]
Available at: https://www.dieselnet.com/tech/fuel_diesel.php
[Accessed 28 July 2015].

Majewski, W. & Jääskeläinen, H., 2009. *Biodiesel—mono alkyl esters.* [Online]
Available at: https://www.dieselnet.com/tech/fuel_biodiesel.php
[Accessed 15 September 2016].

Martinez, I., 2017. *Fuel properties.* [Online]
Available at:
http://webserver.dmt.upm.es/~isidoro/bk3/c15/Fuel%20properties.pdf
[Accessed 3 July 2016].

Merkisz, J., Kozak, M., Bielaczyc, P. & Szczotka, A., 2002. An investigation of diesel fuel sulphur content on particulates emissions from direct injection common rail diesel vehicle. *Journal of KONES internal combustion engines,* 3(4), pp. 1231-4005.

Mollenhauser, K. & Tschoeke, H., 2010. *Hanbook of diesel engines.* 1st ed. s.l.:Springer.

MoRTH, 2010. *Document on test method testing equipment and related procedures for testing type approval and conformity of production (COP) of vehicles for emission as per CMV rules 115,116 and 126.* Pune, India: The automotive research association of India.

Müller, M., 2010. *General air fuel ration and EGR definitions and their calculation from emissions,* s.l.: SAE International.

NASA, 2010. *Measuring and test equipment specifications, NASA measurement quality assurance handbook - ANNEX 2.* 1st ed. Washington DC: National Aeronatics and Space Administration.

National Instruments, 2005. *DAQ - NI 435x user manual,* Austin, TX: National Instruments.

National Instruments, 2015. *DAQ X Series - X series user manual,* Austin, TX: National Instruments.

Nguyen-Schäfer, H., 2015. *Rotordynamics of automotive turbochargers.* 1st ed. Switzerland: Springer International.

Nice, K., 2000. *HowStuffWorks.com.* [Online]
Available at: http://auto.howstuffworks.com/turbo.htm
[Accessed 12 July 2015].

Olfert, J. & Checkel, M., 2007. An ultrrasonic sound speed sensor for measuring EGR levels. *Proceedings of the Institution of Mechanical Engineers, Part D: Journal of Automobile Engineering,* 221(2), pp. 181-189.

Olin, F., 2007. *Modelling of an EGR system,* Lund: Lund University.

Openshaw, K., 2000. A review of Jatropha curcas: An oil plant of unfulfilled promise. *Biomass and Bioenergy,* Issue 19, pp. 1-15.

Optrand Incorporated, 2012. *AutoPSI pressure sensor operating instructions.* Plymouth, MI: Optrand Incorporated.

Palmer, D., 2008. *The development of a biofuels engine testing facility,* Stellenbosch: Stellenbosch University.

Patane, P., Powar, S. & Deshmukh, S., 2016. A physics based model for estimation of EGR mass flow rate. *International journal of current engineering and technology,* Volume 4, pp. 53-62.

Petroleum.co.uk, 2015. *How hydrocarbons burn.* [Online]
Available at: http://www.petroleum.co.uk/how-hydrocarbons-burn
[Accessed 28 December 2016].

Pfeifer, A. et al., 2002. *A new approach to boost pressure and EGR rate control development for HD truck engines with VGT,* s.l.: SAE International.

Pierburg GmbH, 2013. *Exhaust gas recirculation and control with Pierburg components.* Neuss, Germany: KSPG Automotive.

Rashedul, H. et al., 2014. The effect of additives on properties, performance and emission of biodiesel fuelled compression ignition engine. *Energy conversion management,* Volume 88, pp. 348-364.

Reifarth, S., 2010. *EGR-systems for diesel engines.* Stockholm: Department of Machine Design at Royal Institute of Technology.

Reifarth, S., 2014. *Efficiency and Mixing Analysis of EGR-Systems for Diesel Engines.* Stockholm: Department of Machine Design, Royal Institute of Technology.

Reifarth, S. & Angstrom, H., 2009. *Transient EGR in a long-route and short route EGR-system.* Milwaukee, ASME.

Reif, K., 2014. *Diesel engine management - Systems and components.* 1st ed. Wiesbaden: Springer Vieweg.

Richards, P., 2014. *Automotive fuels reference book.* 3rd ed. Warrendale, PA: SAE International.

Romagnoli, A. & Martinez-Botas, R., 2012. Heat transfer analysis in a turbocharger turbine: An experimental and computational evaluation. *Applied Thermal Engineering,* Volume 38, pp. 58-77.

SAE J1349, 2008. *Engine power test code - Spark ignition and compression ignition - Net power rating.* 2008-03 ed. s.l.:SAE International.

SANS1935, 2011. *Automotive biodiesel - Fatty acid methyl esters (FAME) for diesel engines - Requirements and test methods.* Pretoria: Standards South Africa.

SANS342, 2016. *Automotive diesel fuel.* Pretoria: Standards South Africa.

SAPIA, 2008. *Petrol and diesel in South Africa and the impact on air quality,* s.l.: South African Petroleum Industry Association.

SAPIA, 2017. *Cleaner fuels II.* [Online]
Available at: http://www.sapia.org.za/key-issues/cleaner-fuels-ii
[Accessed 10 November 2017].

Schenck, 1976. *Operating instructions for eddy current dynamometer.* 1st ed. Darmstadt: Schenck GmbH.

SKF, 2016. *Initial grease fill.* [Online]
Available at: http://www.skf.com/africa/en/products/bearings-units-housings/super-precision-bearings/principles/lubrication/grease-lubrication/initial-grease-fill/index.html
[Accessed 25 May 2016].

SKF, 2017. *Designs.* [Online]
Available at: http://www.skf.com/group/products/coupling-systems/sh-bushings/designs/index.html
[Accessed 19 September 2017].

SKF, 2017. *SH bushings.* [Online]
Available at: http://www.skf.com/group/products/coupling-systems/sh-bushings/index.html
[Accessed January 2017].

Stone, R., 1992. *Introduction to internal combustion engines.* 2nd ed. London: The MacMillan press Ltd..

Ultra tune, 2010. *Ultra tune gas analyser manual.* Benmore: ULTRA TUNE (Pty) Ltd..

VAG, 2003. *1.9-Liter TDI engine with pump injection (pumpe düse) design and function.* 1st ed. Auburn Hills, Michigan: Volkswagen of America,Inc..

van Basshuysen, R. & Schäfer, F., 2004. *Internal combustion engine handbook - Basics, components, systems and perpectives.* 1st ed. Warrendale, PA: SAE International.

Wahlström, J. & Eriksson, L., 2011. Modelling diesel engines with variable geometry turbocharger and exhuast gas recirculation parameters for capturing non-linear system dynamics. *Proceedings of the institution of mechanical engineers - Part D: journal of automobile engineers,* 225(7), pp. 960-986.

Waterland, L., Venkatesh, S. & Unnasch, S., 2003. *Safety and performance assessment of ethanol/diesel blends (E-Diesel),* Cupertino: National Renewable Energy Laboratory.

WIKA, 2016. *Pressure transmitter for general industrial applications model A-10.* Lawrenceville: WIKA Instruments.

Wu, Y., Huang, R., Lee, C. & Huang, C., 2012. Effects of the exhaust gas recirculation rate and ambient hgas temperature on spray and combsution characteristics of soybean biodiesel and diesel. *Proceedings of the institution of mechanical engineers, Part D: Journal of automobile engineering,* 226(3), pp. 1-13.

Zeldovich, Y., Frank-Kamenetskii, D. & Sadonikiv, P., 1947. *Oxidation of nitrogen in combustion,* Moscow-Leningrad: Institute of Chemical Physics.

Zhang, Z. & Balasubramanian, R., 2016. Investigation of particulate emission characteristiccs of a diesel engine fueled with higher alcohols/biodiesel blends. *Applied energy,* Volume 163, pp. 71-80.

Zhao, H., 2010. *Advanced direct injection combustion engine technologies and development - Volume 2: Diesel engines.* 1st ed. Boca Raton, FL: Woodhead Publishing Ltd..

Zheng, M., Reader, G. & Hawley, J., 2004. Diesel engine exhaust recirculation - a review on advanced and novel concepts. *Energy conversion and management,* Volume 45, pp. 883-900.

Zvizdić, D., 2014. *Fundamentals of measurement of temperature in Air.* [Online] Available at: http://www.npl.co.uk/upload/pdf/20141209-npl-ukas-zvizdic.pdf [Accessed 30 September 2017].

APPENDIX A ENGINE TEST BENCH UPGRADE

Various upgrades to the existing test bench as of 2014 was undertaken to improve upon key areas identified by previous users. Improved control of engine operating parameters such as load, speed, inlet charge temperature and fuel temperature were identified as areas earmarked for upgrade on the test bench. Any data obtained from the improved engine test bench will therefore be more reliable. The repeatability of the experiments will also be improved as the control of inlet parameters such as fuel and charge air temperature will allow any experiment to be replicated regardless of the ambient conditions in the test cell.

A.1. Dynamometer

The primary upgrade to the TDI test bench is improved torque and speed set point control via the dynamometer and dynamometer control unit. The Schenck D360 hydraulic dynamometer, is replaced by a Schenck W130 eddy current dynamometer, Figure 61. The flow of water to the test cells is variable throughout the day. As the hydraulic dynamometer's control stability is highly dependent upon a stable water flow rate, the previous configuration did not suffice. The decision was made to switch to an electricity-based load control. Eddy current dynamometers have improved steady state control versus hydraulic dynamometers.

Figure 61: Schenck W130 eddy current dynamometer

Before any work could be undertaken, a proper plan had to be implemented. The functional analysis from Blanchard & Fabrycky (2011) for systems engineering and analysis was adapted to suit the current application. This plan consisted of three main phases namely disassembly, repair and reassembly.

Disassembly

Upon selection of a suitable dynamometer, the Department's workshop disassembled the dynamometer. The reason for disassembly was to verify whether the dynamometer was still in operating condition.

The dynamometer was disassembled into its constituent components and organized by loose bearing side (LBS) and fixed bearing side (FBS). This approach simplifies the process of inventorying and inspecting all the components. Both the cooling chamber plates were warped. Blocked water channels on the cooling chamber plates were identified as the cause.

During the normal lifecycle of the dynamometer, the water channels between the fins, need to be cleaned and descaled periodically to avoid fouling of the water channels. The fouling observed could be due to the cleaning not being performed regularly enough or the quality/cleanliness of the water running through the dynamometer being poor.

The accumulation of foreign matter inside the water channels of the dynamometer, lead to corrosion of the fins and blocking of the channels. Subsequently the designed heat transfer capacity of each cooling chamber plate was reduced, and the operation of the dynamometer was compromised.

Figure 62, on the left, shows the discolouration of the steel on the LBS cooling chamber plate on the rotor side of the plate. It was surmised that the warping of this plate was mainly due to the heat accumulation in the plate exceeding the design parameters. A concave deflection of up to 2 *mm* was observed on the LBS cooling chamber plate.

Figure 62: Rotor side cooling chamber plates condition post disassembly

Figure 63: Corrosion on cooling chamber plate and support

Figure 62, on the right, shows abrasion on the rotor side of the FBS cooling chamber plate. It was speculated that during operation, the rotor rubbed against the FBS cooling chamber plate. This could be due to incorrect positioning of the rotor between the cooling chamber plates. The heat produced from the friction between the rotor and surface of the FBS cooling chamber plate explains the lesser degree of warping on this plate. The level of fouling in the water channels was also less severe than the LBS cooling chamber plate.

Further components requiring attention included the cooling chamber supports, shown in Figure 63, on the right, the rotor, the two deep groove ball bearings and a cylindrical roller bearing.

Figure 63, on the left, shows the surface that covers the cooling chamber plate to create a watertight seal on the inside and outside of the perimeter. These seals had been compromised by the excess rust on the surface which prevented the cooling chamber from sealing tightly onto the cooling chamber support.

As previously identified, the rotor had an unknown rotational balance. This was due to the rotor blades contacting the rotor side of the FBS cooling chamber plate, as previously mentioned. The rotor was checked for rotational stability and balanced.

Common practice dictates that whenever any bearing is removed from a device such as a dynamometer, it be replaced by a new one regardless of the number of hours the previous bearing has already spent in its lifecycle. The old bearings were all manufactured by FAG but is was opted to replace them with SKF bearings.

A CAD model of all the major operating components of the dynamometer was constructed to aid with identifying tolerance issues and to inventory the parts of the dynamometer. The problems identified during disassembly are listed in Table 10.

Table 10: List of identified problems with the W130

Item/Part	Problem(s)	Solution
LBS cooling chamber plate	Corroded surfaces	Sandblast surface
FBS cooling chamber plate	Warped plate corroded surfaces	Manufacture new plate
FBS and LBS cooling chamber supports	Corroded surfaces	Sand down surface to remove excess rust
Deep groove ball bearings	Unknown lifecycle	Replace with new bearing
Cylindrical roller bearing	Unknown lifecycle	Replace with new bearing
Trunnion bearings	Dirty grease	Clean and re-grease
Rotor	Unknown balance	Rotational balance checked and adjusted
Gasket seals/rings	Worn/Damaged	Replace

Repairing and manufacturing of parts

To assure the correct operation of the dynamometer all the above problems listed in Table 10 were addressed. The following section details the process followed to ensure a fully functional dynamometer was obtained at the end of the refurbishing process.

Initially the cooling chamber plates were both sent for sandblasting, to get rid of all the excess corrosion on the surface and in between the 6 mm fins of the plates to avoid having to manufacture new cooling chamber plates to save time and money.

For the FBS cooling chamber plate this was not an option, as the severity of the warping necessitated that a new plate be manufactured. The plate was measured with a digital Vernier calliper and drafted in Autodesk Inventor 2016. Raw material was obtained, and the drawing submitted to the Department's workshop for manufacture.

The challenge of manufacturing the component was addressed by using a combination of precision turning on the lathe to get rid of the bulk of the raw material and to utilise CNC to machine the water channels of the cooling chamber plate.

Some challenges with this operation was the CNC machine itself. The manufacturing of the water channels called for high speed removal of minimal material, to reduce the amount of stress on the end mill cutter. This was not possible as the CNC machine has a maximum spindle speed of 6000 *RPM*, which was inadequate for the type of cutter used. To ensure the cutter did not break during

operation the maximum spindle speed was used along with a very low feed rate with a moderate plunge depth, as indicated by Table 11.

Table 11: CNC settings for both operations

Roughing operation		**Profiling operation**	
Spindle speed	6000 rpm	Spindle speed	6000 rpm
Feed rate	550 mm/min	Feed rate	1200 mm/min
Plunge depth	0.5 mm	Plunge depth	0.25 mm

Initially the specified settings as per Table 11 was used. A 5 *mm* end mill cutter was used for the roughing operation. The settings specified by the supplier was inadequate for the application as the cutter broke after 4 mm of plunge depth, as seen in Figure 64, on the right.

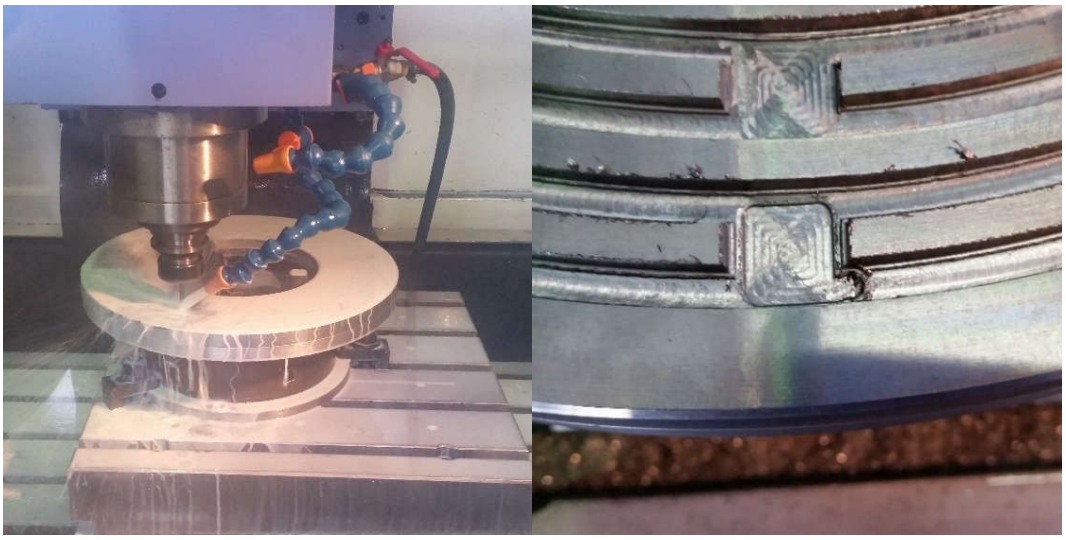

Figure 64: CNC milling operation

The Stellenbosch Technology Centre was consulted on an alternative set of settings for the roughing operation. The feed rate was increased to 1800 mm/min and the plunge depth decreased to 0.15 mm.

After the roughing operation of the cooling chamber plate was completed, the component was sent for heat treatment to stress relieve the plate negating any accumulated local stresses in the plate due to the machining during the roughing operation. The cooling chamber plate was returned to the CNC machine to complete the profiling operation which was accomplished using a 6 *mm* slot drill.

Figure 65, on the left, shows the cooling chamber plate post heat treatment. Figure 65, on the right, shows the finished component after the profiling had been done.

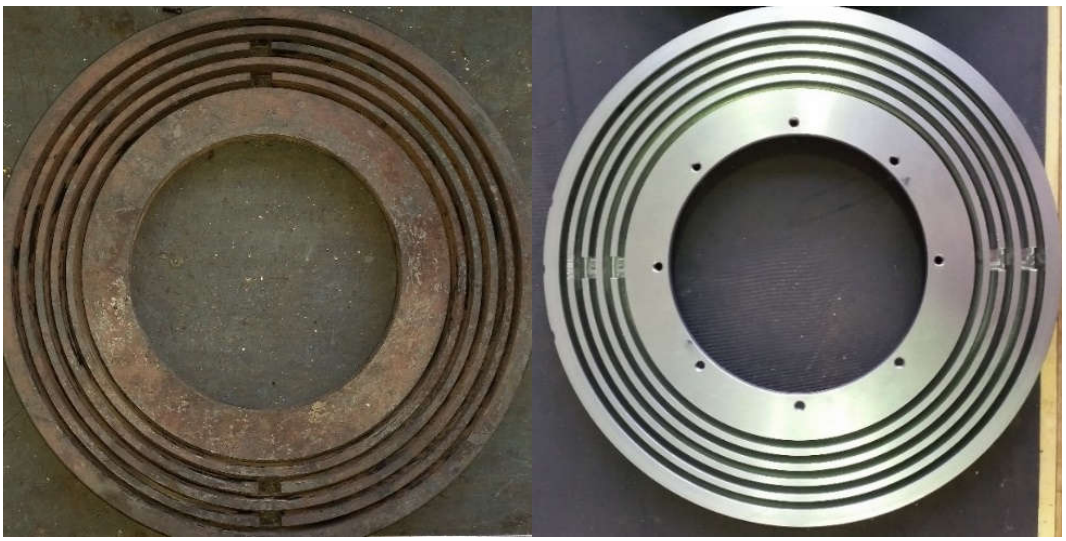

Figure 65: Cooling chamber plate during different stages of manufacturing

The rotor was checked for balance and the cooling chamber supports were sanded down to get rid of most of the excess rust. The trunnion bearings, and all fasteners were cleaned using paraffin. All bearings that needed greasing was greased using SKF LGLT 2/1 low temperature bearing grease, with the quantity of grease per bearing being determined by the equations provided by (SKF, 2016).

Reassembly and fine-tuning tolerances

For the final stage of the refurbishing process, the components were all gathered and cleaned of grime. The components were organized by LBS and FBS, and all components and fasteners were checked against the inventory list made earlier during the first stage of the refurbishment process.

The dynamometer was assembled, and tolerances were adjusted as required by the manufacturer instructions (Schenck, 1976). Table 12 summarises the adjusted tolerances.

Table 12: Tolerance adjustments made to various components

Component	Total Adjustment[mm]
FBS Cooling Chamber Plate (Thickness)	-0,61
LBS Cooling Chamber Plate (Thickness)	-0,49
FBS Cooling Chamber Support (Surface Height)	-0,60
LBS Cooling Chamber Support (Surface Height)	-0,60

Upon successful assembly, with all stated tolerances and alignments of (Schenck, 1976) to within acceptable limits, the dynamometer was sent for painting and

mounted onto the test bench. Final adjustment of the bearing clearance and verification of the allowable runout on the shaft flange was performed on the test bench as per the manufacturer's procedure (Schenck, 1976)

A.2. Fuel conditioning unit

The work done by Blom (2015) on the improvement of the fuel conditioning unit was further refined as part of the test bench refurbishment. A compact frame was constructed to securely contain the OEM diesel filter, aftermarket filter, two plate heat exchangers and the three-way mixing valve and actuator, as seen in Figure 67.

During his tests Blom (2015) reported that the fuel supply temperature never exceeded 1 °C of the fuel set point which was set to 30 °C. For the current project, the fuel set point was adjusted to 22 °C, close to ambient conditions. Fuel temperature control is confirmed to still fall within the specifications established by Blom (2015). Figure 66 shows the typical operating point stability of the fuel supply temperature control. Figure 68 shows the fuel conditioning circuit as developed by Blom (2015). The fuel conditioning unit is supplied with water from the chilled water circuit, described in section A.6.

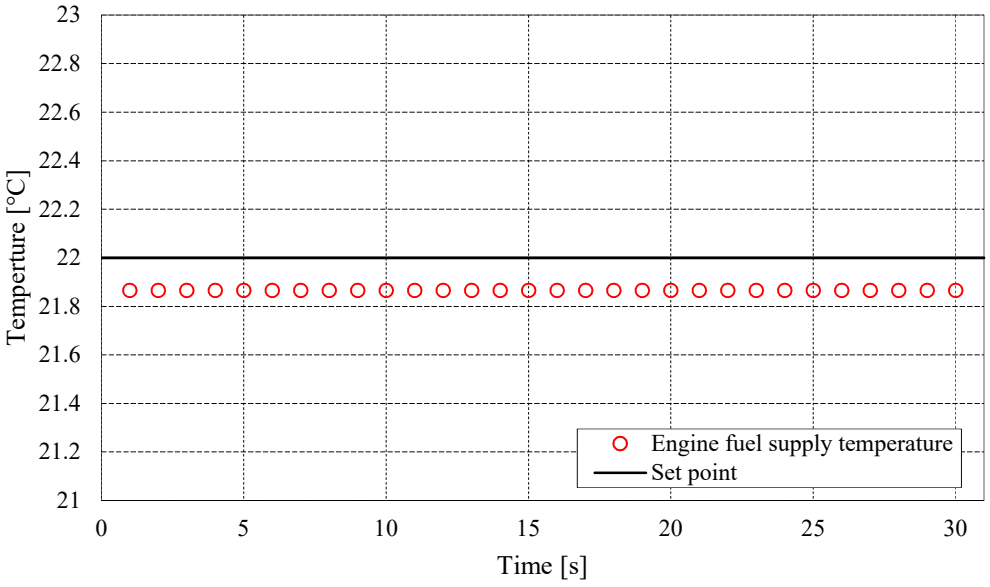

Figure 66: Fuel supply temperature control

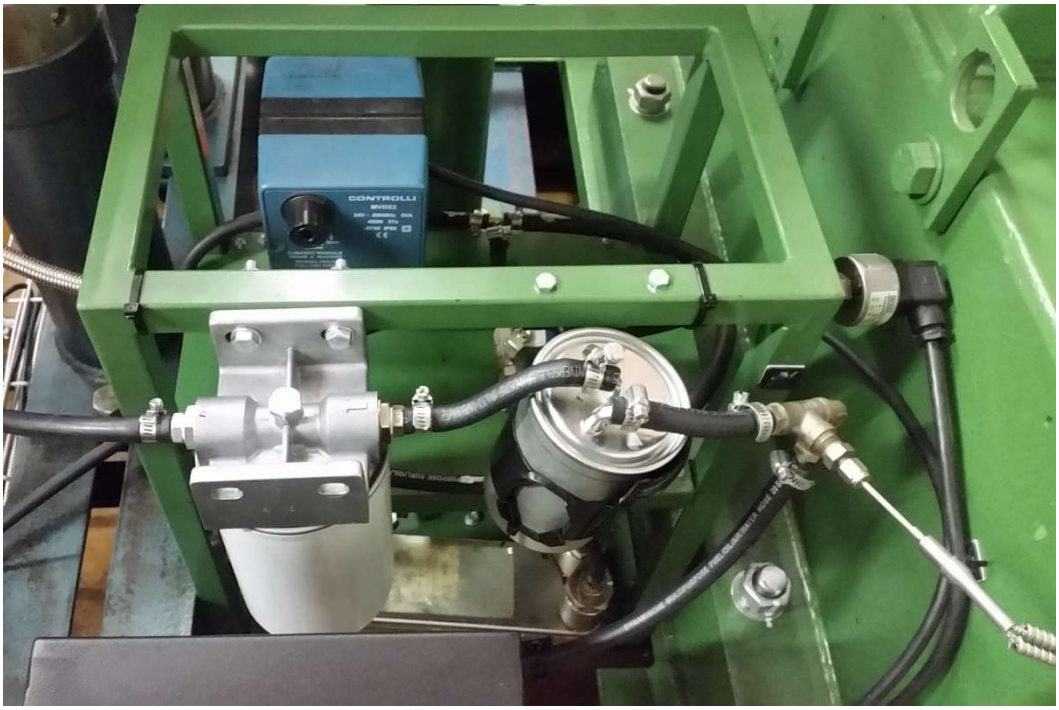

Figure 67: Compact fuel conditioning unit installed on test bench

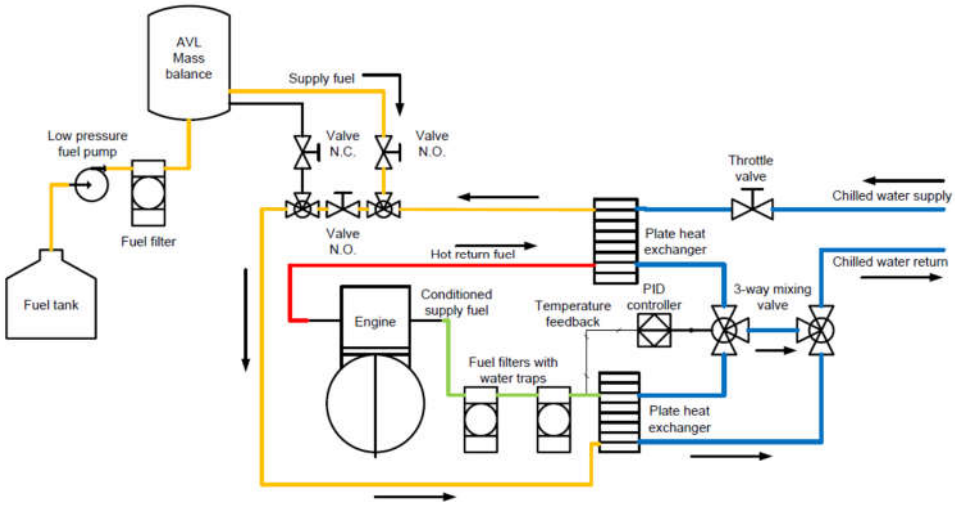

Figure 68: Fuel conditioning unit heat transfer circuit (Blom, 2015)

A.3. Intercooler

A previous shortcoming of the engine test bench was the lack of adequate charge air control. A project by Karsten (2014) served to address this shortcoming. The standard air-to-air intercooler could not reliably control the charge air temperature at load conditions exceeding 100 N.m. The intercooler was designed with a charge air temperature set point that may not exceed 30 °C whilst testing. The intercooler is supplied with chilled water at approximately 9 °C, and forms part of the chilled water supply circuit.

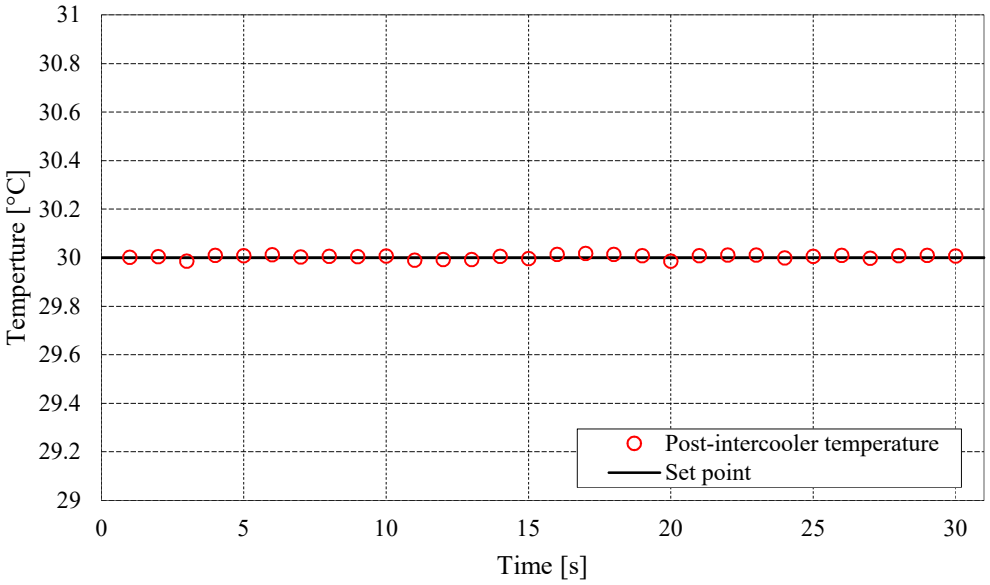

Figure 69: Charge air temperature control

The charge air temperature control of the air-to-water intercooler shows a marked increase in performance over the stock air-to-air intercooler used previously, as seen in Figure 69. The ability of the intercooler to maintain a stable operating temperature of 30 *°C* for 3000 *RPM* at 160 *N.m* is shown.

A.4. Throttle input

One of the areas identified by Blom (2015) was the improvement of the throttle input, since at the time the throttle input to the engine control unit was accomplished by mechanically actuating the pedal module of the TDI with a servo motor via a voltage signal from the Allen Bradley MicroLogix 1200 PLC, as seen in Figure 70.

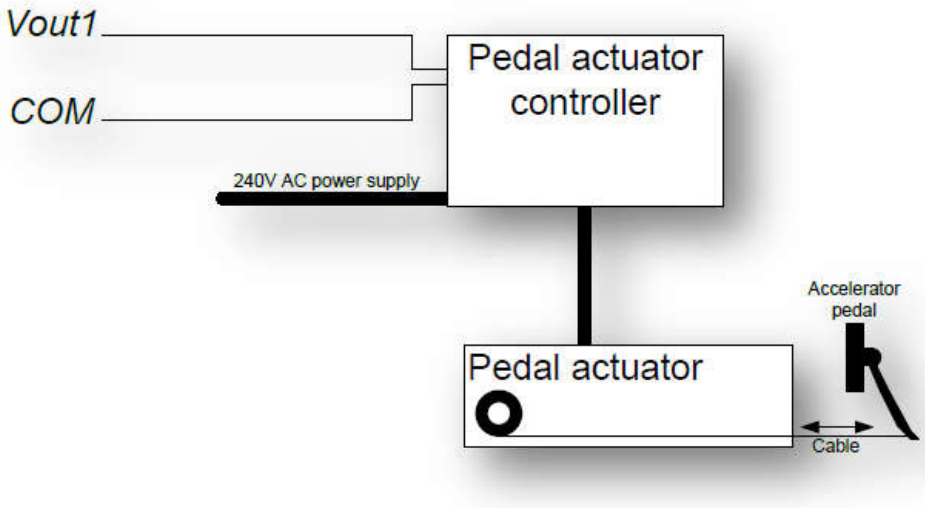

Figure 70: Previous throttle input configuration (Kotze, 2010)

Whilst this proved an adequate solution to implementing throttle control, it proved problematic as the actuation circuitry had to be calibrated often during testing to ensure that the throttle percentage specified by ETA, corresponds to that seen by the engine control unit and VCDS.

The motivation for changing the throttle input to an electronic circuit that simulates the operation of the pedal module, came when the old pedal control circuitry that controlled the servo motor started failing due to damaged wiring and blown capacitors, which could also explain the drifting calibration.

The operation of the pedal input to the engine control unit was investigated. It was discovered that the throttle control is accomplished by three signals. The pedal actuation module incorporates three components which generate these signals, namely the accelerator position sender, kick-down switch and the idling switch. The accelerator position sender acts by sending a voltage signal to the engine control unit, indicating the pedal position i.e. the throttle percentage.

A malfunction of this module will cause the engine to only run at a higher idling speed (VAG, 2003). In addition to this the kick-down switch activates when the driver wants to accelerate by activating when the pedal hits full throttle. The idling speed switch is engaged when the pedal position is at rest.

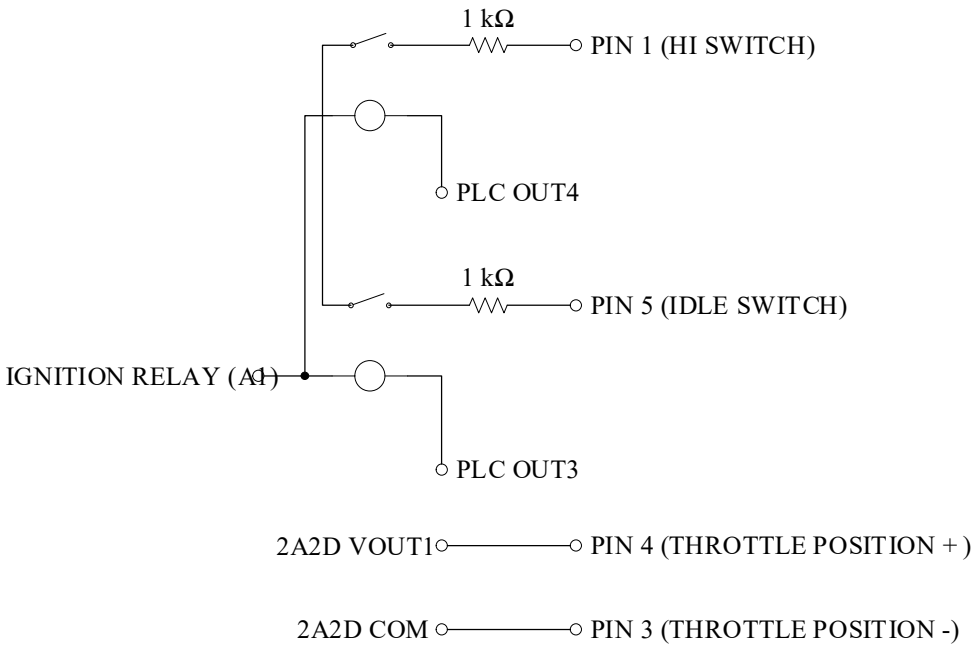

Figure 71: Pedal module simulating circuit

The electronic circuit, seen in Figure 71, simulates the operation of the pedal module comprises of two relay switches and a 12-bit analogue voltage output from the PLC. The idling switch is simulated by the normally closed relay switch. The kick-down switch is simulated by the normally open switch. The relays are actuated via output from the PLC to mimic their respective operation as described above. The accelerator position sender is simulated by supplying the engine control unit with a 0.338 V to 4.286 V indicating idle and full throttle respectively.

A.5. Driveshaft coupling modification

An improvement to the driveshaft-to-engine coupling junction was earmarked as an aspect to improve upon by the project supervisor. The concern was that the spline on the shaft interfacing with the clutch plate would fatigue prematurely by having it transfer all the engine power through to the dynamometer. The driveshaft modification proposed, consists of a SH bushing which is a mechanical friction joint, as seen in Figure 72 (SKF, 2017).

This design dispenses with the spline, opting instead to use two tapered sleeves, an inner and an outer, with the outer sleeve tightening the inner sleeve onto the shaft, connected to the engine, as the outer sleeve is wedged into position on the outside hub, connected to the driveshaft. This coupling is accomplished by pressure and friction, thereby negating the need for a spline or a key and keyway. The hub connecting to the clutch plate assembly is lubricated using Castrol automatic transmission fluid.

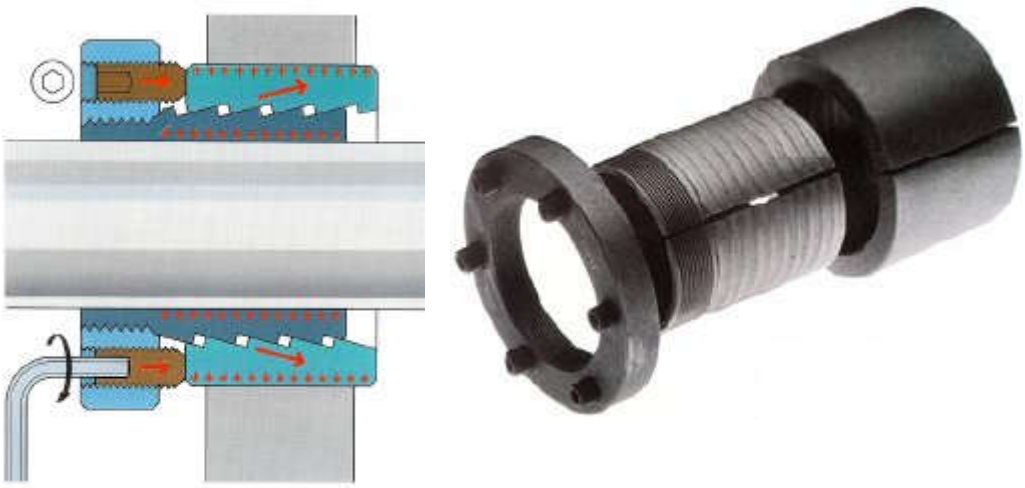

Figure 72: Core component of the driveshaft coupling modification (SKF, 2017)

To accommodate the new driveshaft modification and coupling the driveshaft to the W130, two intermediate couplings had to be designed and manufactured. Both featured, precision machined spigots to align the axis of rotation of the engine, driveshaft and dynamometer concentrically.

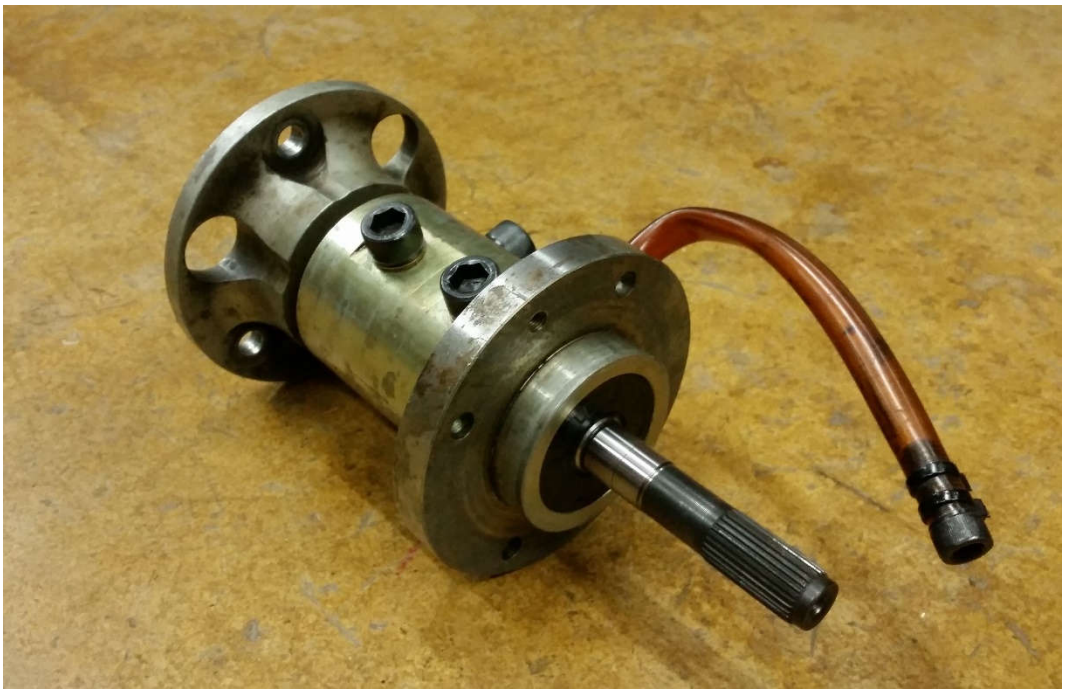

Figure 73: Driveshaft coupling modification design

The CV joint was disassembled and cleaned to get rid of any fouling of the lubricating grease. The CV joint was then reassembled and lubricated using molybdenum disulphide grease.

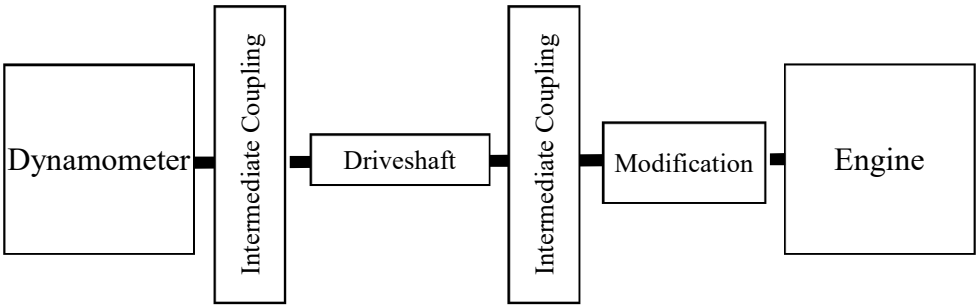

Figure 74: Drive-line schematic of test bench

A.6. Water supply circuits

To ensure optimal temperature control of the test bench's individual components, water cooling is employed throughout. These components include the dynamometer, intercooler, fuel conditioning unit and the heat exchanger which acts as the engine's radiator. The test cell facilities allow the use of two separate water sources namely the chilled water and cooling tower water.

The chilled water circuit supplies water from a system comprising a circulation pump and a chiller which keeps the water supply at approximately 9 °C. It was decided that the intercooler and fuel condition unit be placed in parallel on the chilled water circuit as these components require a stable supply temperature to function optimally.

The cooling tower water is pumped from a large reservoir beneath ground level to a tank on top of the building. This water does not pass through a heat exchanger but relies on the reservoir temperature to regulate the water temperature. The dynamometer and heat exchanger are placed in parallel on the cooling tower circuit.

The dynamometer and the heat exchanger are placed on the cooling tower circuit as the cooling of dynamometer requires only flowing water at ambient temperatures to function optimally. The heat exchanger was originally the only component placed on the cooling tower circuit.

Magnetic filters are installed on both water circuits, as the water from both sources are unclean. Without the filters, significant build up in the circuits may lead to a reduced cooling capacity, which in turn will affect the temperature control capabilities of the individual components. The filters also trap larger particulates which may cause damage to the pipes and block the components' heat exchanging elements. All piping consisted of multipurpose fibre reinforced rubber piping able to withstand pressure of up to 10 *bar*.

Figure 75: Magnetic filters

APPENDIX B ENGINE TESTBENCH RECOMMISSIONING

The upgrades done on the TDI test bench, necessitated the replication of results to prove repeatability of the results obtained during the experiments to an acceptable degree of accuracy. During the recommissioning of the test bench troubleshooting on various components had to be performed to attain the desired repeatability of results.

B.1. Repeatability tests

All repeatability tests are performed using the synthetic 50 *ppm* ULSD. Exhaust gas temperatures at different operating points are compared to verify consistent results for the same fuel source. Figure 76 shows the repeatability of the exhaust gas temperatures within 15 °C. The results obtained from comparing the repeatability tests are consistent with that obtained by Blom (2015) bearing in mind that due to a lower intercooler charge air temperature the exhaust gas temperature is lower by approximately 50 *°C*.

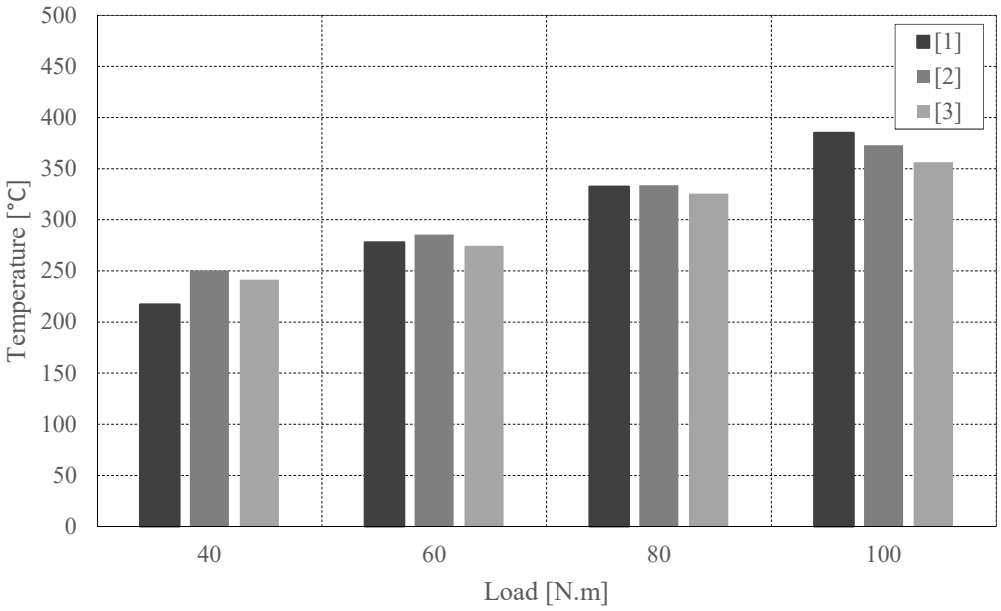

Figure 76: Exhaust gas temperature repeatability at 1800 RPM

The in-cylinder pressure traces are primarily used in this project to establish repeatability of results. A hot motored curve was obtained at 1800 *RPM* to determine the phasing of the shaft encoder. The signals are filtered using a zero phase second order low-pass Butterworth filter. Figure 77 shows good repeatability when using the synthetic bracket fuels. The phasing is shown to be consistent as are the peak pressures.

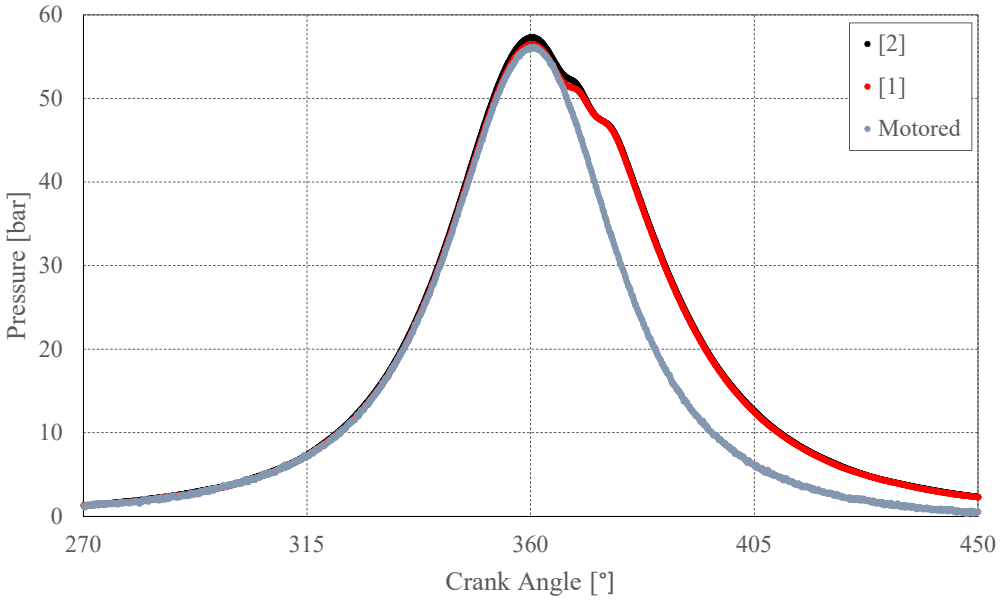

Figure 77: In-cylinder pressure trace repeatability for 1800 RPM at 20 N.m

Figure 78 establishes repeatability for the brake specific fuel consumption of the engine at the indicated operating points. It should be noted that the brake specific fuel consumption is improved due to the addition of a suitable charge air cooler and eddy current dynamometer with average standard deviation values of 4 *g/kW.h*.

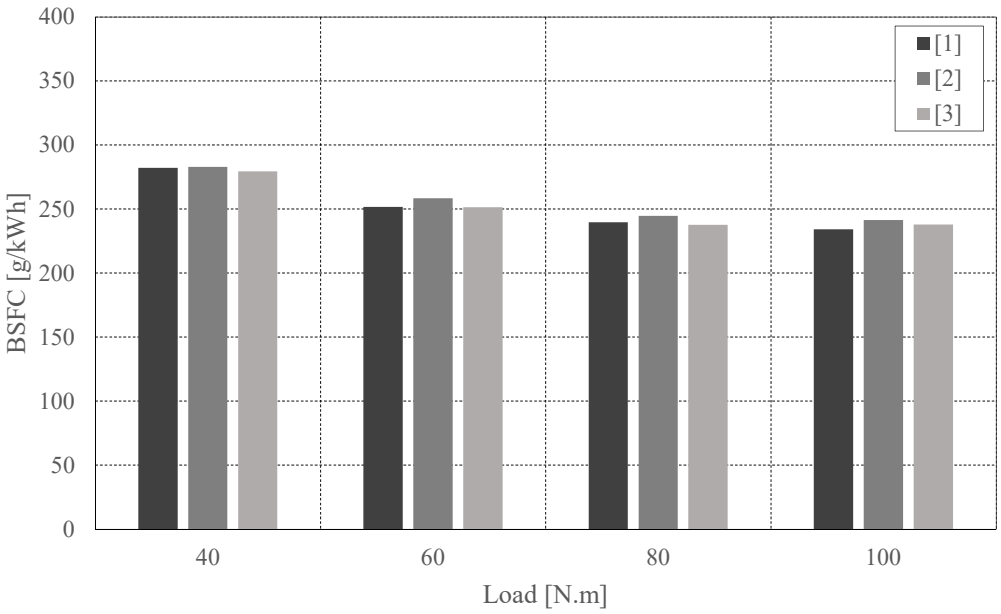

Figure 78: BSFC repeatability at 1800 RPM

APPENDIX C CALIBRATION OF MEASUREMENT EQUIPMENT

Calibration of the test bench instrumentation is done to ensure the accuracy, repeatability and thereby reliability of all measurements taken. All calibration was performed by the data acquisition devices used during testing to ensure any discrepancies between data acquisition devices are negated.

C.1. Thermocouples

Thermocouple calibration was performed in two temperature ranges i.e. low temperature and high temperature. A total of twenty thermocouples were calibrated, seventeen of which are low temperature thermocouples and three are high temperature thermocouples. The low temperature calibration procedure ranges between *0* °C to *140* °C in increments of *20* °C. The high temperature thermocouple calibration procedure ranges between *200* °C to *800* °C in *100* °C increments.

Figure 79 shows the results for the low temperature calibration. Figure 80 shows the results for the high temperature calibration. It should be noted that the signal conversion from voltage to temperature is handled by both ETA and LabVIEW internally. The temperature correction equations for the low temperature thermocouples are summarised in Table 13. The temperature correction equations for the high temperature thermocouples are summarised in Table 15.

Table 13: Low temperature correction equations

Description	R^2	Equation
Atmospheric	0.999	y = 0.9637 + 1.5727
Intercooler charge	0.999	y = 0.96x + 1.635
Compressor inlet	0.999	y = 0.9529x + 1.779
Compressor outlet	0.999	y = 0.9588x + 1.7035
Inlet manifold	0.999	y = 0.9548x +1.9278
Oil	0.999	y = 0.9725x -0.0302
Fuel supply	0.999	y = 0.9624x + 0.2577
Fuel return	0.999	y = 0.9429x + 1.635
Inlet air	0.999	y = 0.9428x + 1.073
Intercooler charge	0.999	y = 0.9708 + 1.7728
Dynamometer FBS	0.999	y = 0.9724x + 0.7563
Dynamometer LBS	0.999	y = 0.9731x + 0.9066
Coolant supply	0.999	y = 0.9719x +0.1612
Coolant return	0.999	y = 0.9698x +0.7335
Intercooler charge air control	0.999	y = 0.9664 + 1.1135
Fuel supply control	0.999	y = 0.9629x +1.002
Coolant supply control	0.999	y = 0.9708 + 2.1314

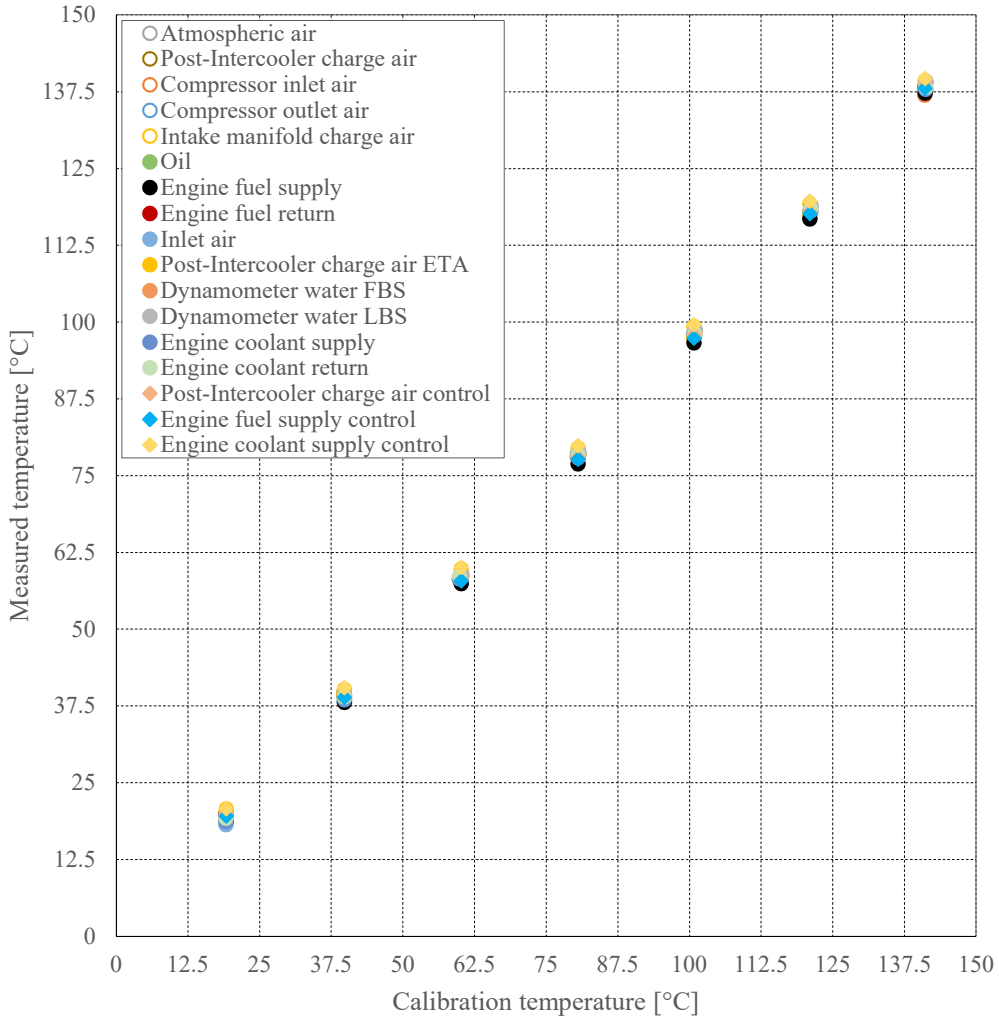

Figure 79: Low temperature thermocouple calibration

The thermowells used to perform the calibration of the thermocouples are the Fluke 9143, for low temperature calibration and Fluke 9150, for high temperature calibration. Table 14 shows the specifications of the thermowells (Fluke, 2013), (Fluke, 2014).

Table 14: Temperature calibrator specifications (Fluke, 2013) (Fluke, 2014)

Fluke 9143	**Specification**	**Fluke 9150**
-25 °C to 150 °C	Range	150 °C to 1200 °C
	Last calibration date	16 November 2016
± 0.2 °C	Accuracy	± 5.0 °C
± 0.02 °C	Stability	± 0.5 °C

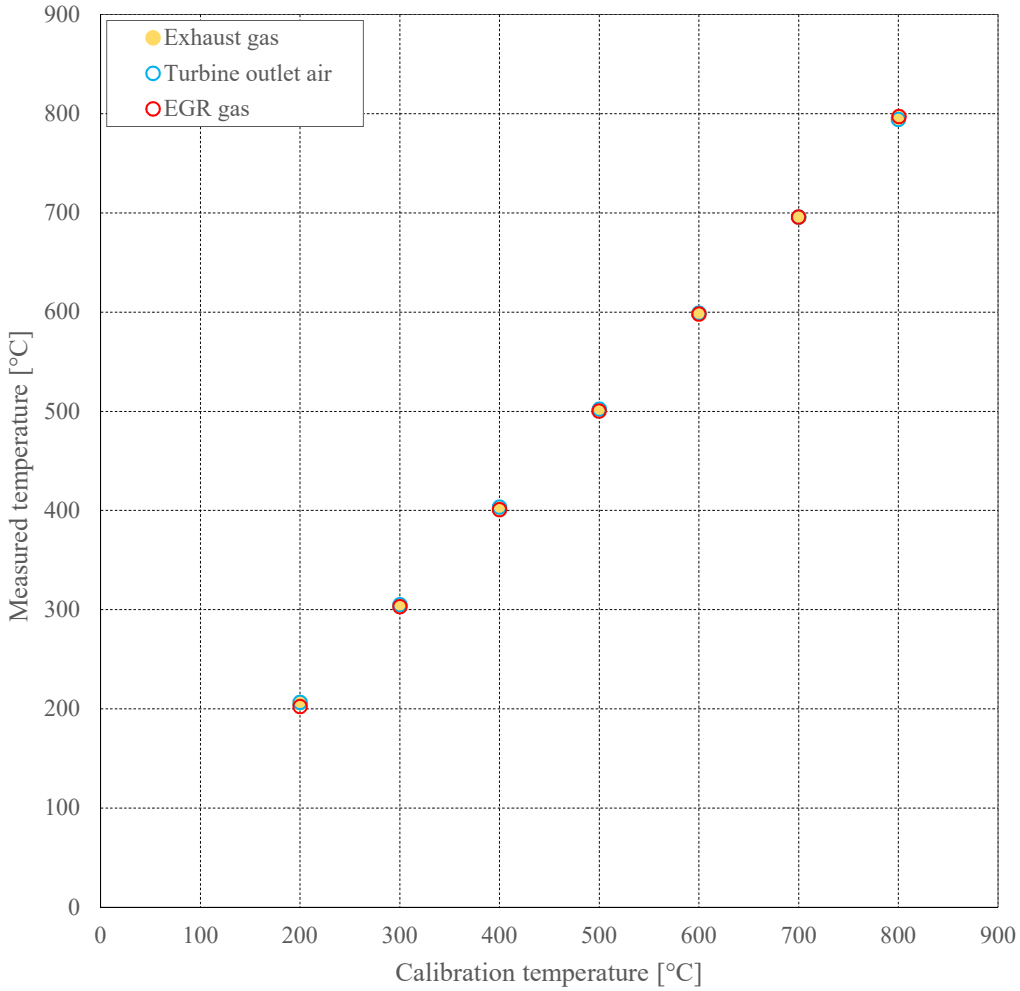

Figure 80: High temperature thermocouple calibration

Table 15: High temperature correction equations

Description	R^2	Equation
Exhaust gas	0.999	y = 0.9837x + 8.6017
Turbine outlet	0.999	y = 0.9819x + 9.5929
EGR gas	0.999	y = 0.9902x + 4.2507

C.2. Pressure transmitter and in-cylinder pressure transducer

The pressure calibration was done using two different calibrators. For the in-cylinder pressure transducer, the Fluke P5514-2700G was used. The rest of the pressure sensors were calibrated using the Druck DPI 610. Table 16 shows the specifications of the pressure calibration devices (Fluke, 2010), (Druck Ltd., 1999). The Druck DPI 610, was used to routinely establish good compliance with the initial calibration.

Table 16: Pressure calibrator specifications

Fluke P5514-2700G	Specifications	Druck DPI 610
70 Bar (Gauge)	Range	20 Bar (Gauge)
0.02% Full Scale	Accuracy	0.025% Full Scale
± 14 mbar	Stability	-

The Optrand PSIglow-A pressure transducer used to measure in-cylinder pressure, was calibrated to validate the sensitivity of the transducer as indicated by Optrand Incorporated. The calibration ranges from 0 to 200 *bar* in 200 *psi* increments. The calibration procedure was performed as indicated by (Optrand Incorporated, 2012). Figure 81 shows the calibration points obtained from calibration.

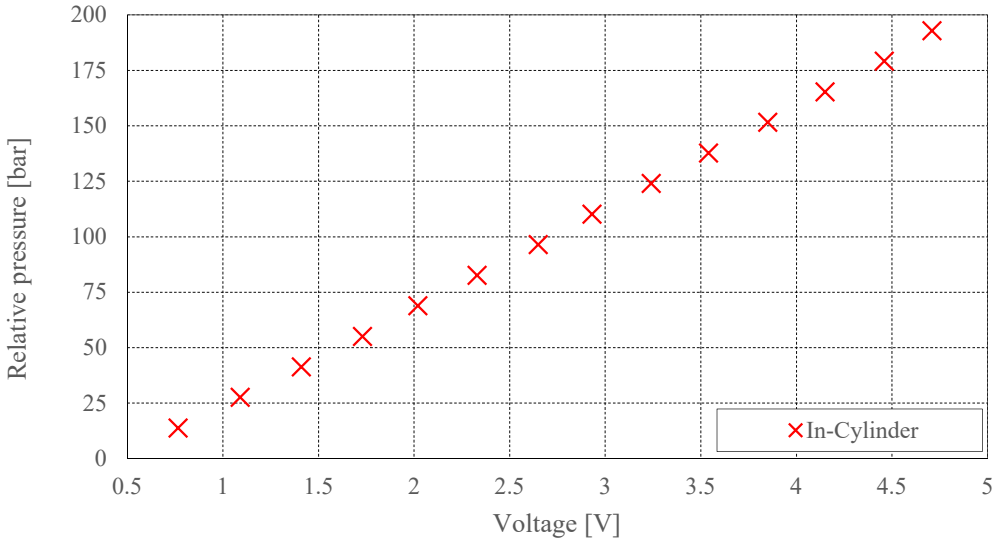

Figure 81: Optrand pressure transducer calibration 0 to 200 bar

Likewise, the Huba and WIKA pressure transmitters were calibrated. These pressure sensors are calibrated in *Pa* and thereafter converted to *mbar*. This is done

especially for the differential pressure sensors as their pressure variations are of the order in *Pa*. Figure 82 to Figure 86 shows the calibration points for the transmitters.

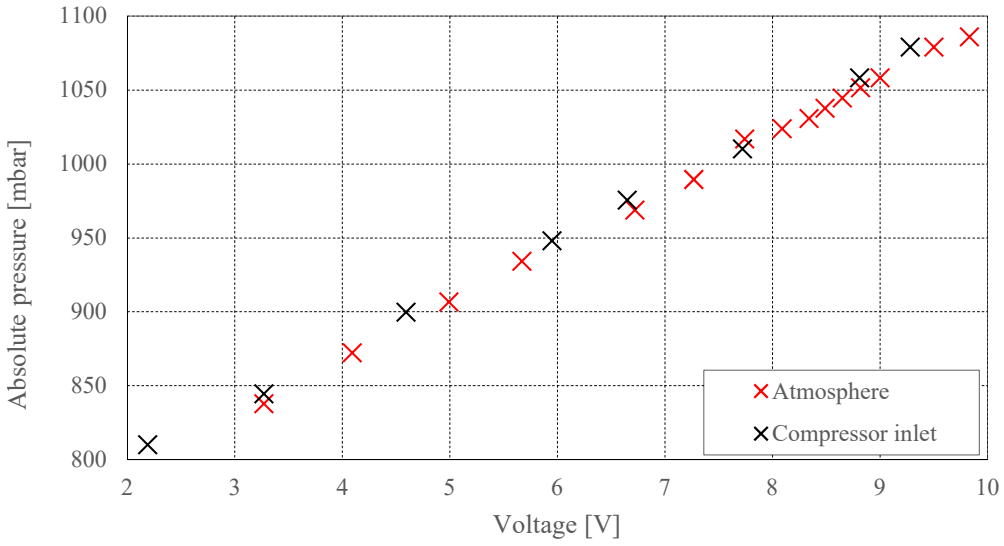

Figure 82: Huba pressure transmitter calibration 0.8 to 1.1 bar

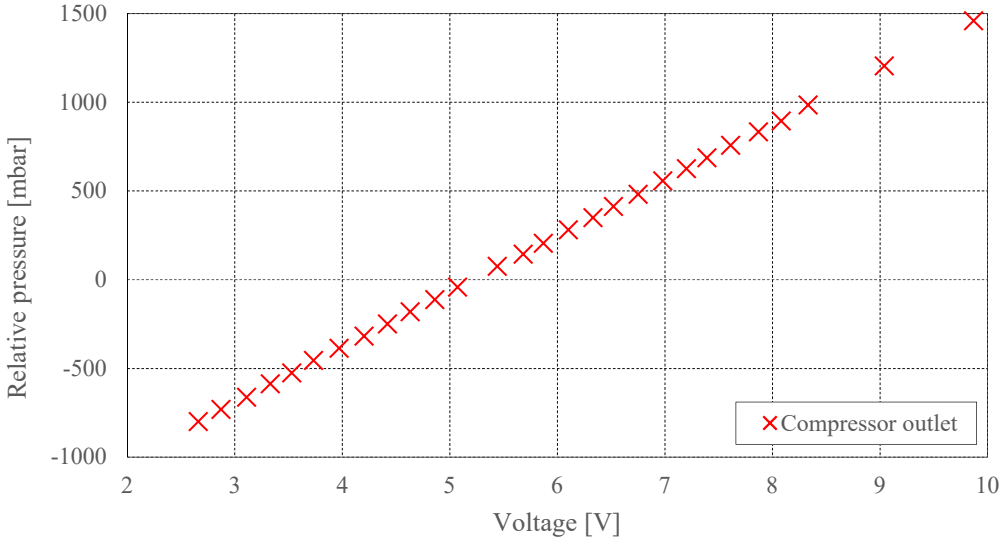

Figure 83: Huba pressure transmitter calibration -1 to 1.5 bar

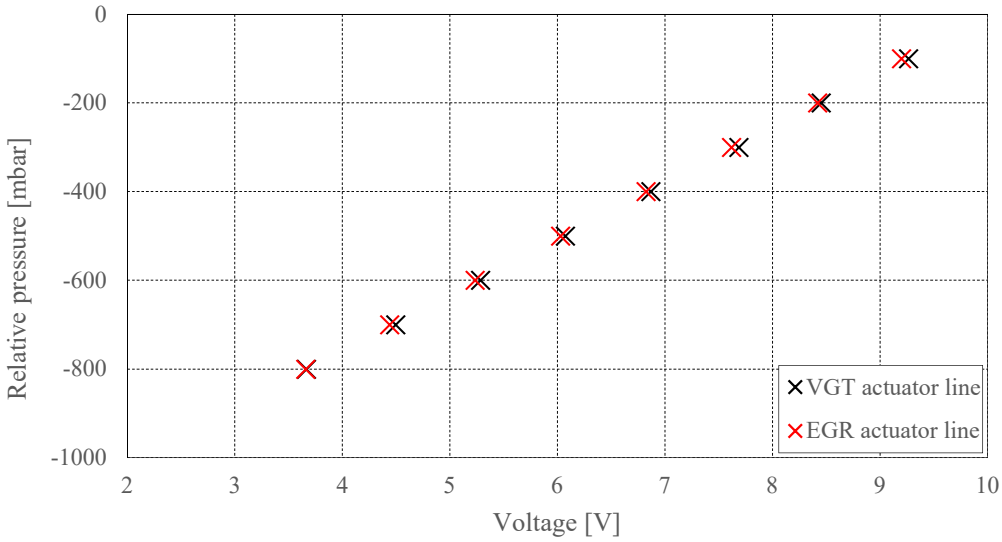

Figure 84: Huba pressure transmitter calibration -1 to 0 bar

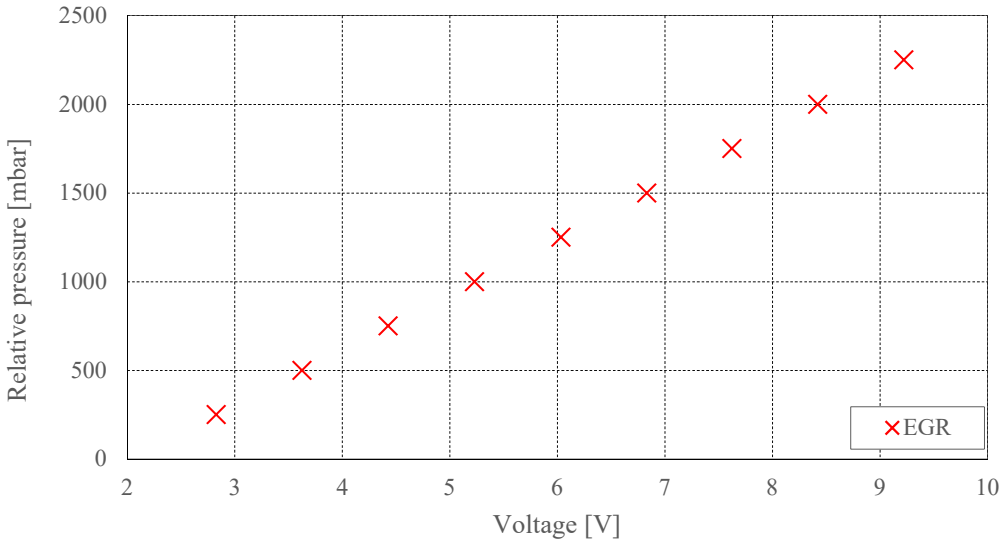

Figure 85: WIKA pressure transmitter calibration 0 to 2.5 bar

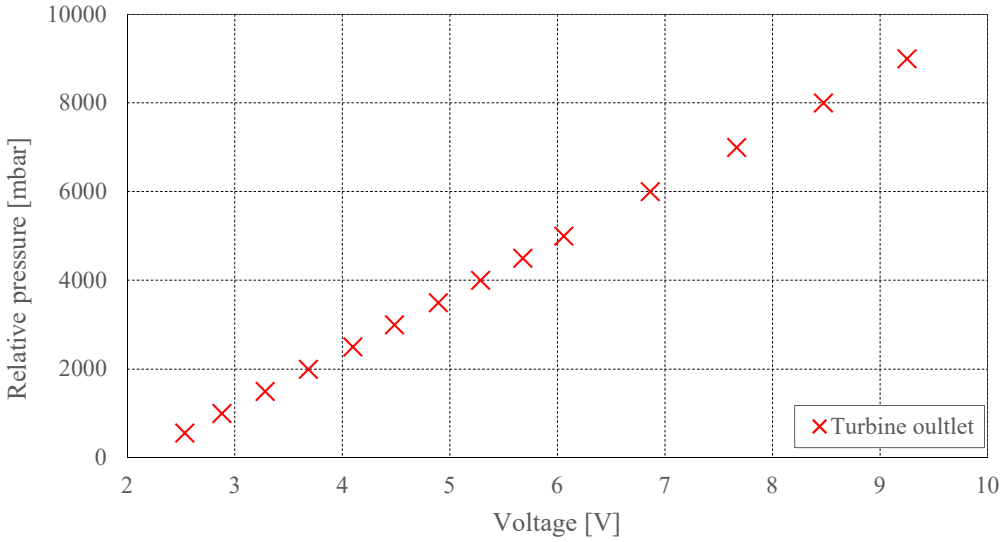

Figure 86: WIKA pressure transmitter calibration 0 to 10 bar

The pressure correction equations obtained from the calibration, is summarised in Table 17.

Table 17: Pressure correction equations

Description	R^2	Equation
In-cylinder pressure	0.999	y = 45.5562x – 23.061
Atmosphere	0.999	y = 38.152x+714.61
Compressor inlet	0.999	y = 37.982x + 722.36
Compressor outlet	0.999	y = 313.58x - 1631.8
VGT actuator line	0.999	y = 125.24x -1261
EGR valve line	0.999	y = 125.45x - 1257
EGR	0.999	y = 312.9x -634.83
Turbine outlet	0.999	y = 1255.7x -2627

C.3. Dynamometer load cell

The calibration of the load cell is performed pre-and post-testing, to validate the measurements from the load cell. The importance of the accuracy and repeatability necessitates the checking of hysteresis of the load cell for this calibration.

Calibration is performed by first ensuring a zero offset before fixing the calibration arms to the dynamometer. The load cell reading is then zero offset again to prepare

for the loading of the weights on the weight tray suspended from the calibration arm one metre away from the centre of rotation of the dynamometer. Calibrated one-kilogram weights are then lowered onto the tray to simulate approximately 10 *N.m* load increase each time. The maximum load for the dynamometer, 400 *N.m* is checked, and the weights are systematically removed to check for hysteresis. Figure 87 shows the calibration points for the load cell calibration.

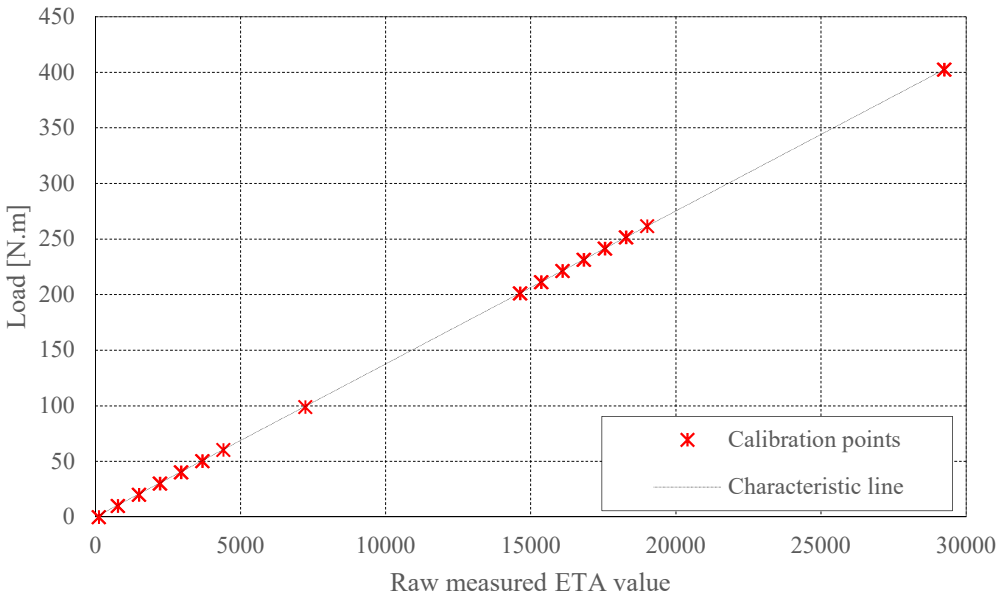

Figure 87: Load cell calibration

The stability of each reading was assessed by noting the fluctuations of the raw measured value obtained in ETA. The stability was found to be satisfactory. Before each test was run the calibration of the dynamometer was compared to the above. Each calibration was confirmed to be accurate and comparable the original calibration. The load cell and amplification therefore have good long-term stability.

Table 18: Load cell correction equation

Description	R^2	Equation
Load	0.999	y = 0.0138x

C.4. Venturi tube

The venturi tube is calibrated using the DISA Type 55D41 calibration unit. The venturi tube is fixed in series with the calibration unit at the unit's nozzle inlet as seen in Figure 88. Two differential pressure transducers are used to take measurements at each of the pressure stations. To verify the differential readings

obtained at each of the stations, the differential pressure transducers are also used to measure each individual pressure tapping relative to atmospheric pressure.

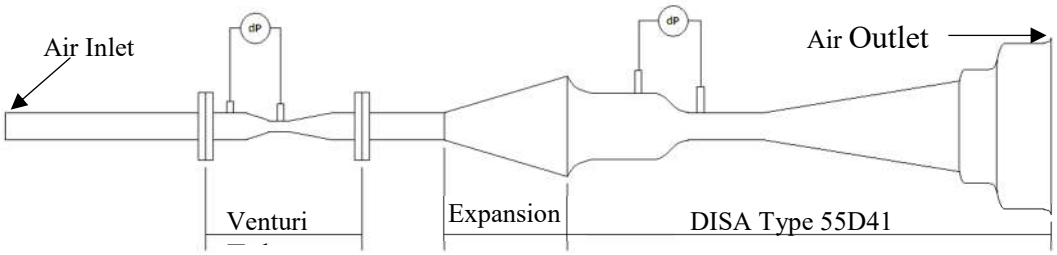

Figure 88: Venturi tube calibration configuration

All measured pressure readings are first corrected according to the operating manual for the DISA (Department of mechanical and mechatronic engineering , n.d.).

$$\Delta p' = \Delta p \frac{101325}{p_o} \tag{21}$$

Equation (22) is then used to determine the velocity of the flow at the nozzle measuring section of the calibration unit. The gas constant, R, and isentropic exponent, κ, for air is 287.1 *J/kg.K,* and 1.4 respectively.

$$c^2 = \frac{2\kappa}{\kappa - 1} RT_o \left[1 - \left(1 - \frac{\Delta p'}{p_o} \right)^{\frac{\kappa - 1}{\kappa}} \right] \tag{22}$$

Once the velocity has been obtained it is also corrected for variation in reservoir temperature.

$$c' = c \sqrt{\frac{T_o}{293}} \tag{23}$$

The volumetric flow rate can then be determined for each of the measured differential pressure points. The diameter at the nozzle measuring section is 14 *mm*.

$$q_v = c'A \tag{24}$$

Plotting the various measured data points against the calculated volumetric flow rate, enables the determination of the characteristic volumetric flowrate curve.

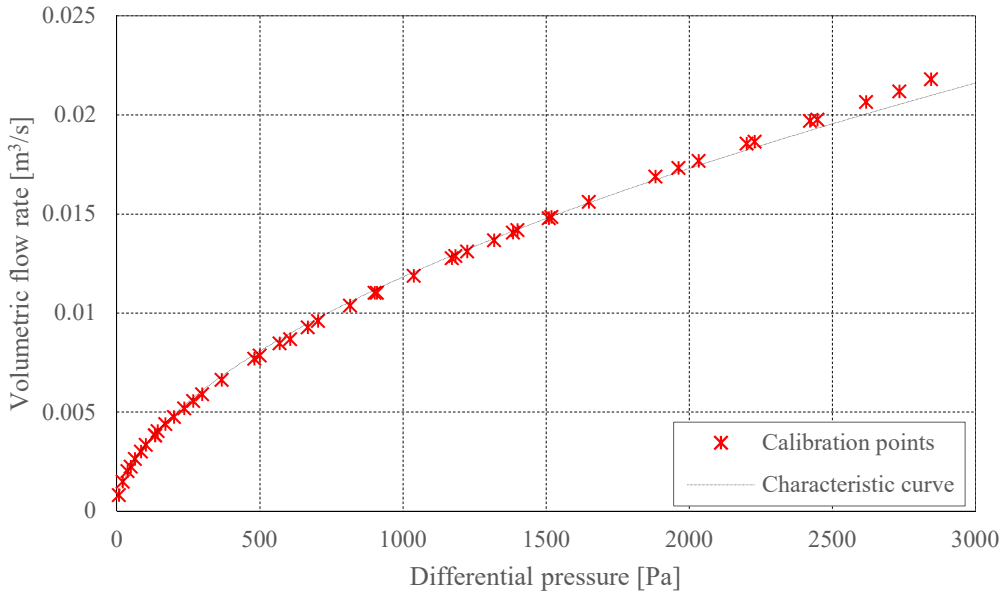

Figure 89: Venturi tube calibration

Table 19 shows the characteristic curve obtained for the volumetric flow rate. The coefficient of determination shows good agreement of the trendline to the data points. Equation (25) is obtained from the regression analysis in Figure 89.

Table 19: Volumetric flow rate equation for venturi tube

Description	R^2	Equation
Volumetric flow curve	0.999	$y = 2.666e^{-4}x^{0.549}$

$$q_v = 2.666e^{-4}\Delta p_{measured}^{\ 0.549} \tag{25}$$

The final equation is then obtained by correcting the equation in Table 19, to standard conditions and accounting for the change in Reynolds number of the exhaust flow with a discharge coefficient. Equation (26) shows the formula used to obtain the mass flow rate of the recirculated exhaust gas. The density of exhaust gas is determined by using the ideal gas law with the specific gas constant for diesel exhaust being 286.89 *J/kg.K* (MoRTH, 2010). Analysis shows the Reynold number does not change significantly, therefore a constant discharge coefficient of 0.985 is used.

$$q_m = \rho_{exhaust} C_d \left(\frac{T_{cal}}{T_{EGR}}\right)\left(\frac{p_{EGR}}{p_{cal}}\right) q_v \tag{26}$$

C.5. Meriam laminar flow element Model 50MC2

The Meriam laminar flow meter was calibrated by installing it in series with the calibration air flow wind tunnel in the flow laboratory. Calibration was performed by Mr Andre Brink, a MEng (Mechanical) student from the department. The procedure involved determining the air mass flow rate through the laminar flow meter and converting it to volumetric flowrate using the procedure described in Kröger (1998). The calibration points include compensation for any leaks that occurred due to the connection of the laminar flow meter to the calibration tunnel.

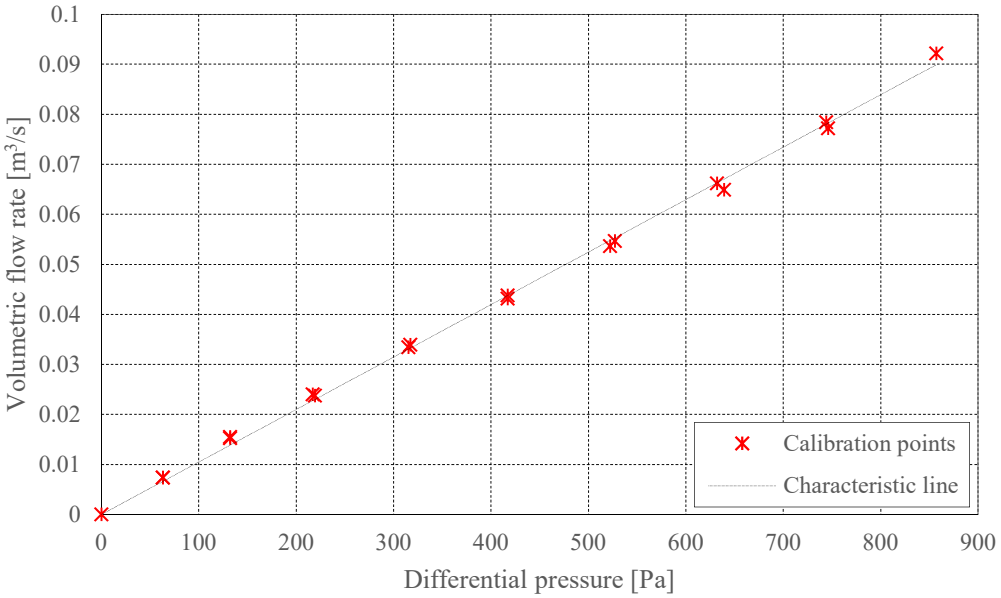

Figure 90: Laminar flow meter calibration

A linear regression line was then fitted to obtain the equation for the volumetric flowrate through the laminar flow meter as seen in Figure 90.

Table 20: Volumetric flow rate equation for laminar flow meter

Description	R^2	Equation
Volumetric flow line	0.998	$y = 1.049e^{-4}x$

The final equation, Equation (27) used to calculate the mass air flow, is shown below.

$$q_m = \rho_{air} 1.049e^{-4} \Delta p_{measured} \quad (27)$$

C.6. AVL 730 dynamic fuel consumption meter

The fuel consumption of the 1.9L TDI is measured using the AVL 730 measuring equipment series. The equipment comprises of the following:

- Dynamic Fuel Balance 7130-09 Cabinet Unit
- Evaluation Fuel Calculator 7030-A01 Module
- Analogue-to-Digital Converter (ADC) 7030-A03 Module
- Balance Control 7030-A04 Module

To ensure accurate brake specific fuel consumption measurement, the unit must be calibrated annually. For this project the linearity and gain are checked and adjusted, according to the manufacturer recommendations (AVL, 1987).

Calibration is done at three fuel levels, as seen in Table 21. To check linearity, a calibrated weight is lowered onto the fuel vessel and lifted in the "empty" and "full" states. If the measured weight of the calibration weight is the same in each state, only the gain must be adjusted. If not, the procedure outlined in the operating manual must be followed to adjust the linearity. To check the gain, the calibration weight is again lowered and lifted from position, however this time from the "half" state. The measured weight must be within the tolerance shown below. If not, the procedure for adjusting the gain in the operating manual must be followed.

Table 21: AVL 730 tolerances

Calibration Weight	**Tolerance**	**Fuel level**		
		Empty	Half	Full
100 g	±0.1 g	50 g to 80 g	380 g to 410 g	820 g to 850 g

Once the linearity and gain has been properly calibrated the unit must at any fuel level conform to the tolerances stated in Table 21 when checking the calibration in calibration mode.

APPENDIX D HARDWARE AND SOFTWARE SPECIFICATIONS

The various hardware specifications for the new sensors added to the test bench is shown below in Table 22 and Table 24. The specifications for the emission sampling instrumentation is given in Table 23. Relevant information on the fuel consumption meter is also given in Table 25.

Table 22: Pressure sensor specifications

Huba type 691 pressure transmitters	
Response time	< 5 ms
Tolerance	±0.3 % FS
Non-linearity, hysteresis and repeatability	±0.3 % FS
Stability	±0.5 % FS
Resolution	±0.1 % FS
Operating temperature	-15 to 80 °C
Overpressure limit	2 x FS
WIKA A-10 pressure transmitters	
Response time	< 4 ms
Non-linearity	0.5 % FS
Repeatability	0.1 % span
Operating temperature	0 to 80 °C
Overpressure limit	2 x FS
Endress+Hauser Deltabar PMD55 differential pressure transmitter	
Resolution	1 µA
Reference accuracy	±0.2 % FS
Stability	±0.25 % FS
Total Error	±0.95 %
Operating temperature	-40 to 85 °C

Table 23: Emissions analysis instrumentation specifications

Dräger MSI 150 Euro-E diesel exhaust gas analyser		
Gas	**Accuracy**	**Range**
Carbon Monoxide	±20 ppm	0 to 4000 ppm
Nitrogen oxide	±10 ppm	0 to 2000 ppm
Nitrogen dioxide	±5 ppm	0 to 200 ppm
AVL 415 Smoke meter		
Particulates	**Accuracy**	**Range**
Soot density	± 0.05 FSN	0 to 9.99 FSN
ULTRA TUNE exhaust gas analyser		
Gas	**Accuracy**	**Range**
Carbon dioxide	±3.0 % FS	0 to 20 % vol
Oxygen	±0.1 % vol	0 to 25% vol

Table 24: Speed sensor specification

PICOTURN© PT1G Series Sensor	
Operating Temperature	-40 to 230 °C
PICOTURN© BMV6.2 signal conditioning unit	
Operating Temperature	-40 to 85 °C
Output tolerance	0.5 % FS

Table 25: AVL 730 fuel consumption meter specifications

Dynamic fuel balance 7130-09	
Measuring accuracy	± 0.15% of consumed mass
	± 0.005 % of vessel mass
Temperature sensitivity	± 0.01 % per °C
Fuel calculator 7030-A01	
Resolution	0.01 kg/h for fuel mass < 100 g
	0.1 kg/h for fuel mass > 100 g
Analog-to-digital converter ADC 7030-A03	
Filter	1 Hz / 16 dB / Oct.
ADC conversion	100 ms

Figure 91 shows the instrumentation layout of the test bench setup. PC1 interfaces with the programmable logic controller (PLC) mentioned in section 4.2.

PC2 uses LabVIEW to communicate with both the NI USB-6351 and the NI USB-4350. The block diagram, shown in Figure 92, illustrates the programmatic flow of the LabVIEW program developed for data acquisition of the exhaust gas recirculation and variable geometry systems. The other LabVIEW program, used to sample the in-cylinder pressure traces, was adapted from Blom (2015), and is not shown here.

PC3 communicates with VCDS via a OBD-II (onboard diagnostics) connector. This connector is necessary to scan the data received from the engine control unit and to relay it to the PC via a USB connection. In this way the engine control unit can be interrogated whilst operational, to report real-time data to the user.

PC4 communicates with the Ultra tune gas analyser via a serial connection. Software accompanying the instrument allows the user to control the sampling time and when to trigger the instrument to log the relevant emissions data. The logged data is saved to a text file.

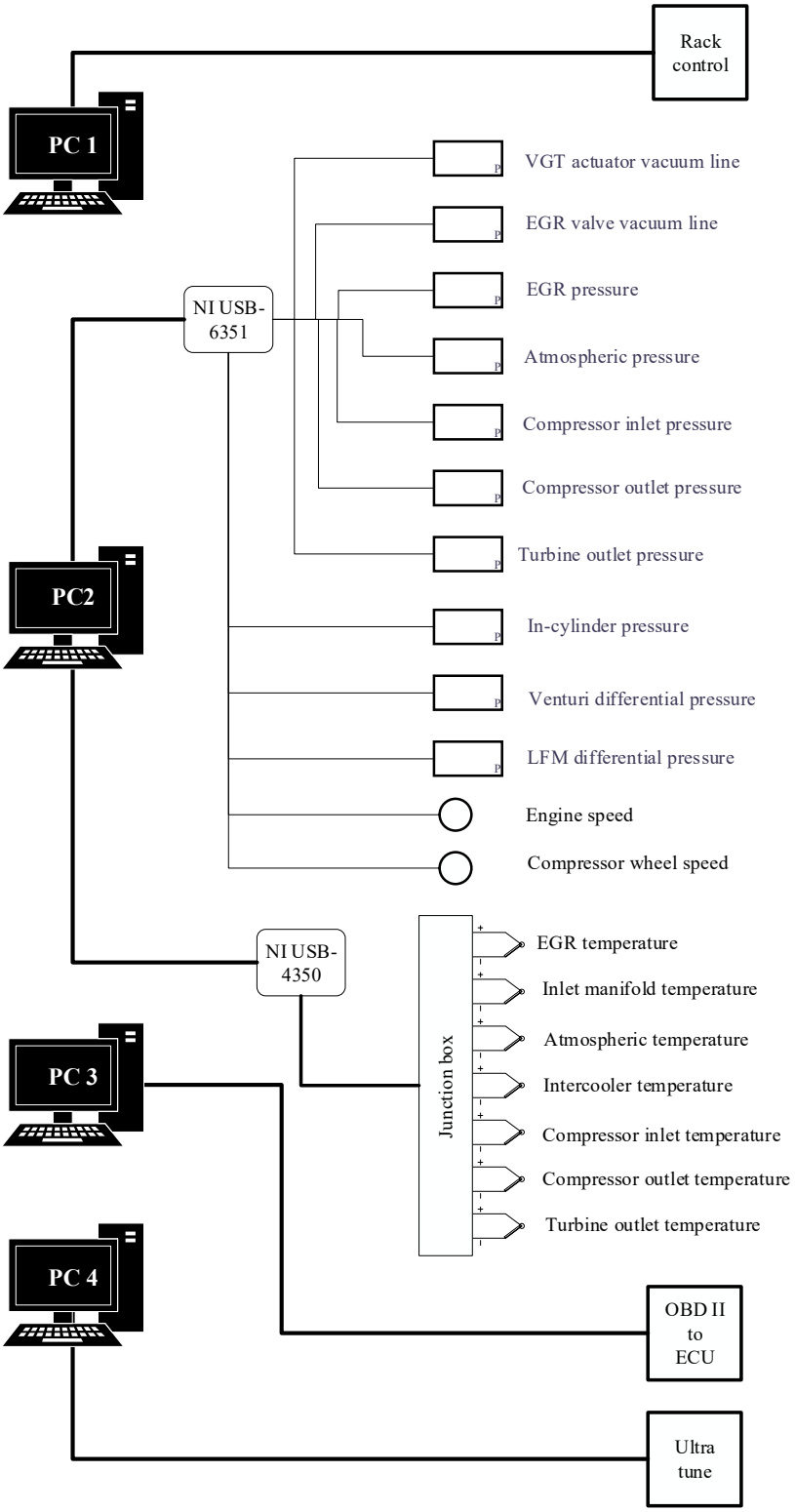

Figure 91: Instrumentation wiring layout

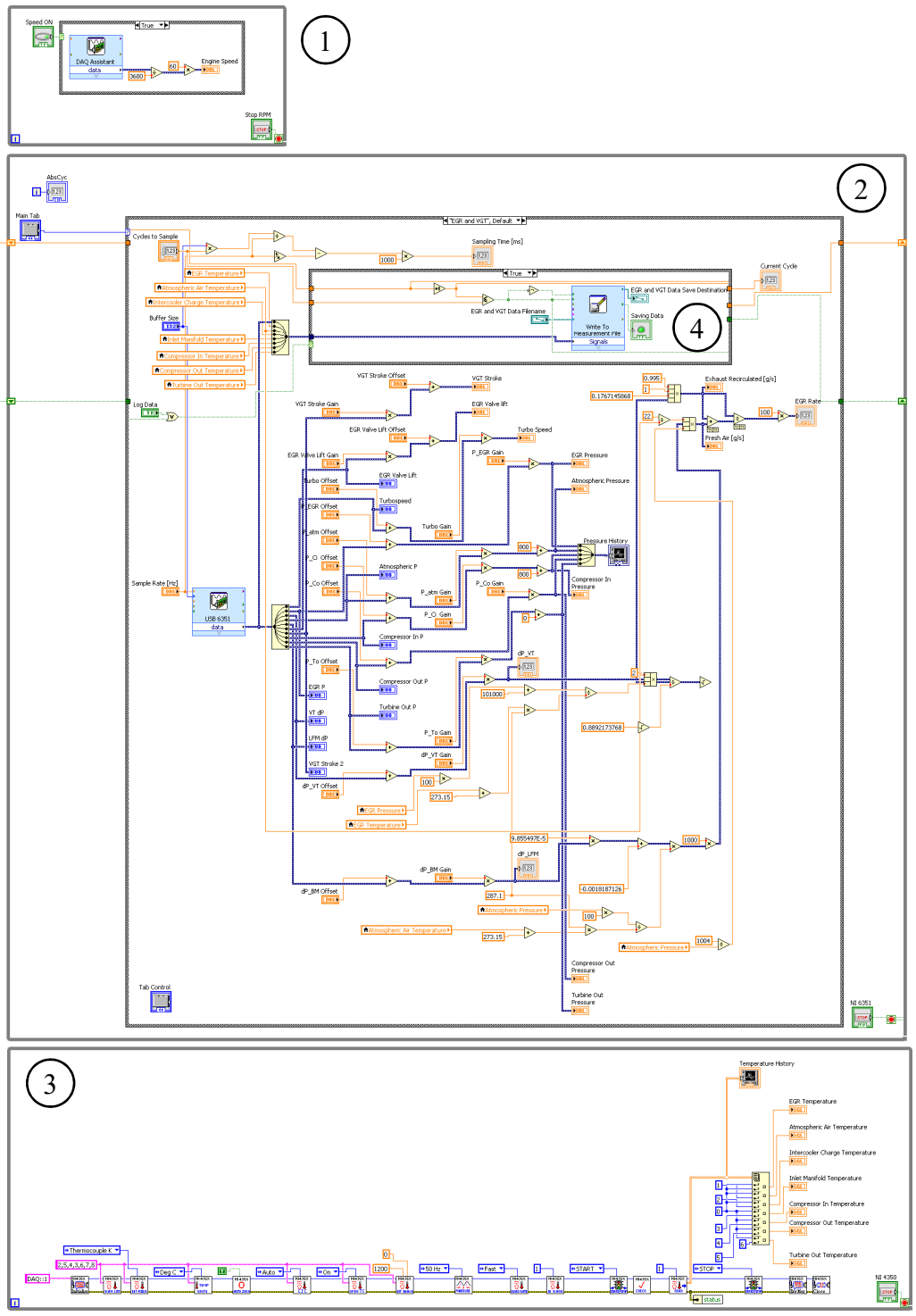

Figure 92: LabVIEW program block diagram

The LabVIEW program, shown in Figure 92, comprises of three main loops. These loops execute continuously until the program is stopped. Information is passed between the loops by using local variables. This ensures that one loop does not have to wait for the other to finish executing before it can start.

The first loop consists of a counter that converts the pulses obtained from the shaft encoder, attached to the crankshaft of the engine, to a frequency. This frequency is then used to calculate the speed of the engine.

The second loop handles all the analogue input channels connected to the NI USB-6351. A total of fifteen analogue input terminals are used, with seven channels being referenced single ended analogue inputs and the remaining four channels configured as differential inputs (using eight terminals). One of the differential inputs is reserved for the in-cylinder pressure sensor which interfaces with a separate program adapted from the program Blom (2015) developed.

The ten channels, used for this program, are sampled at 60 Hz. The built-in DAQ-Mx utility of LabVIEW is used to configure each channel accordingly and to acquire the data from the NI USB-6351. Once the data stream, containing the raw information from each sampled channel, flows from the DAQ-Mx utility, it is split into individual channel data streams. These streams are then converted by the calibration values input on the front panel, discussed in section 3.4. Once the conversions have been done the data is displayed on the front panel of the program.

The third loop handles the temperature acquisition from the NI USB-4350. It is configured for type-K thermocouples, with cold-junction compensation enabled. The built-in 50 Hz noise filter of the NI USB-4350 is also enabled. This loop logs each thermocouple value once before it exports the values to an array, which sorts the values into their appropriate local variables. A total of 7 channels are read during each iteration of the loop which updates every 1.1 seconds on the front panel of the graphical user interface.

For data logging, the raw data is saved to LabVIEW's proprietary TDMS file format. This file format compresses the data that is logged to save hard drive space. This data can be converted to an excel spreadsheet via the excel TDMS plugin. The data logging is accomplished by using the LabVIEW: "Write to measurement file" function. All data logging is accomplished in the fourth loop.